ORNL/TM-9831

ornl

OAK RIDGE NATIONAL LABORATORY

MARTIN MARIETTA

The Advanced Toroidal Facility

J. F. Lyon
B. A. Carreras
K. K. Chipley
M. J. Cole
J. H. Harris
T. C. Jernigan
R. L. Johnson
V. E. Lynch
B. E. Nelson
J. A. Rome
J. Sheffield
P. B. Thompson

OPERATED BY
MARTIN MARIETTA ENERGY SYSTEMS, INC.
FOR THE UNITED STATES
DEPARTMENT OF ENERGY

Printed in the United States of [illegible]
National Technical Information [illegible]
U.S. Department of Commerce
5285 Port Royal Road, Springfield, [illegible]
NTIS price codes: Printed Copy [illegible]

ORNL/TM-9831
Dist. Category UC-20

Fusion Energy Division

THE ADVANCED TOROIDAL FACILITY

J. F. Lyon

B. A. Carreras
K. K. Chipley*
M. J. Cole*
J. H. Harris
T. C. Jernigan
R. L. Johnson*
V. E. Lynch+
B. E. Nelson*
J. A. Rome
J. Sheffield
P. B. Thompson*

*Engineering Division, Martin Marietta Energy Systems, Inc.
+Computing and Telecommunications Division, Martin Marietta Energy Systems, Inc.

Date Published - September 1986

Prepared by the
OAK RIDGE NATIONAL LABORATORY
Oak Ridge, Tennessee 37831
operated by
MARTIN MARIETTA ENERGY SYSTEMS, INC.
for the
U.S. DEPARTMENT OF ENERGY
under Contract No. DE-AC05-84OR214(

CONTENTS

TABLES

FIGURES

ABSTRACT

The Advanced Toroidal Facility (ATF), now under construction at Oak Ridge National Laboratory, will be the world's largest stellarator experiment when it begins operation in early 1987. It will have a 2.1-m major radius and a 0.3-m average plasma radius, a magnetic field of up to 2 T for a 5-s pulse and up to 1 T steady state, and up to 5 MW of plasma heating. The ATF is designed to study a wide range of toroidal confinement issues, including confinement and stability of high-beta plasmas, low-collisionality transport, impurity behavior, magnetic configuration optimization, and steady-state operation.

The ATF is the result of a study of a large number of possible coil configurations. It is an $\ell = 2$, 12-field-period torsatron with rotational transform between 0.3 and 1 and with plasma aspect ratio $R/\bar{a} = 7$. This optimized helical field coil configuration permits direct access to a high-beta, second stability region in a flux-conserving manner, and volume-average beta values above 8% may be achieved. The poloidal coil system allows study of a large variety of stellarator configurations, including those with a helical magnetic axis, and external control of the fundamental magnetic configuration parameters, including rotational transform, shear, magnetic well, and plasma shape.

The ATF consists of two segmented, jointed helical field coils; three sets of poloidal field coils; a thin, helically contoured vacuum vessel; and a thick, segmented, toroidal shell support structure. Its important design features include extensive access for plasma heating and diagnostics, a high degree of construction accuracy, and parallel construction techniques.

This paper describes the ATF torsatron, the physics and engineering reasons for the different design choices, and the expected capabilities of the device.

I. INTRODUCTION

The Advanced Toroidal Facility (ATF) now under construction at Oak Ridge National Laboratory (ORNL) will be the world's largest and most versatile stellarator facility when it begins operation in early 1987 [1]. It has been designed to study a wide range of stellarator magnetic configurations, including those with a helical magnetic axis, and to combine good confinement properties with the potential for high-beta operation (volume-average beta $\langle\beta\rangle \gtrsim 8\%$). The ATF is expected to study a number of general toroidal confinement issues, including confinement and stability of high-beta plasmas, low-collisionality transport, impurity behavior, magnetic configuration optimization, and steady-state plasma operation.

A sketch of the ATF is shown in Fig. 1. The main components are two segmented, jointed helical field (HF) coils; three pairs of poloidal field (PF) coils, labeled inner, outer, and mid-vertical field (VF) coils; an exterior shell structure to support the magnetic and thermal loads from the coils; and a thin, helically contoured vacuum vessel closely conforming to the HF coils. The distance between the bottom of the lower mid-VF coil and the top of the upper mid-VF coil is 1.9 m, and the outer diameter of the outer VF coils is 6 m. The 12 large outer ports (0.9 by 0.6 m), 12 inner ports (0.2 m in diameter), and 24 upper and lower ports (0.35 by 0.35 m) provide extensive access for diagnostics, tangential neutral beams, ion cyclotron heating (ICH) antennas, pump limiters, and maintenance.

The relationship of the major ATF components is shown in more detail in Figs. 2 and 3. The centers of the top and bottom ports lie in the $\phi = 0^{\circ}$ plane, and the centers of the inside and outside ports occur in the $\phi = 15^{\circ}$ plane.

The main ATF device parameters are given in Table I. The ATF is an $\ell = 2$, 12-field-period torsatron [2] with moderate rotational transform ($\iota = 1/q = 0.3$-1), shear [$(\iota(a)/\iota(0) \sim 3)$], and plasma aspect ratio ($A = R/\bar{a} = 7$). Although this aspect ratio is smaller than that of most stellarators ($A = 10$-20), it is larger than that of most tokamaks. This configuration was chosen after study of a large number

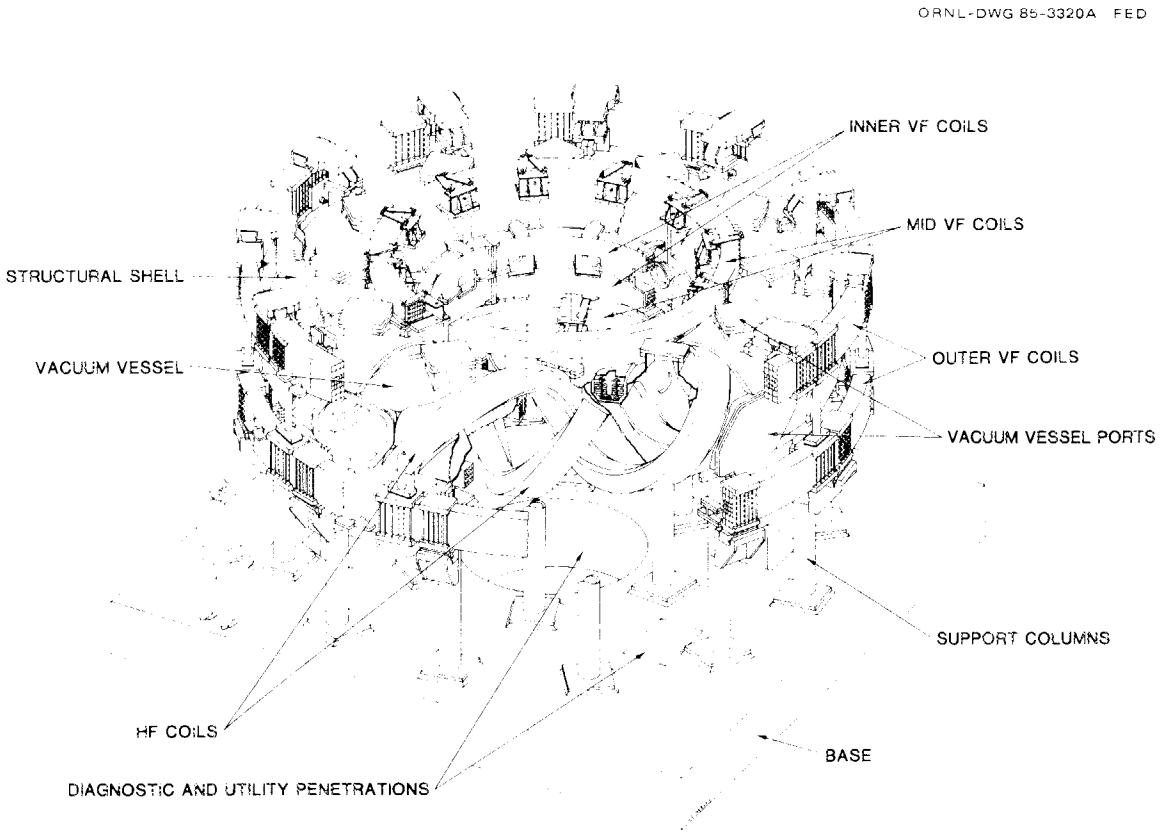

Fig. 1. Artist's sketch of the ATF.

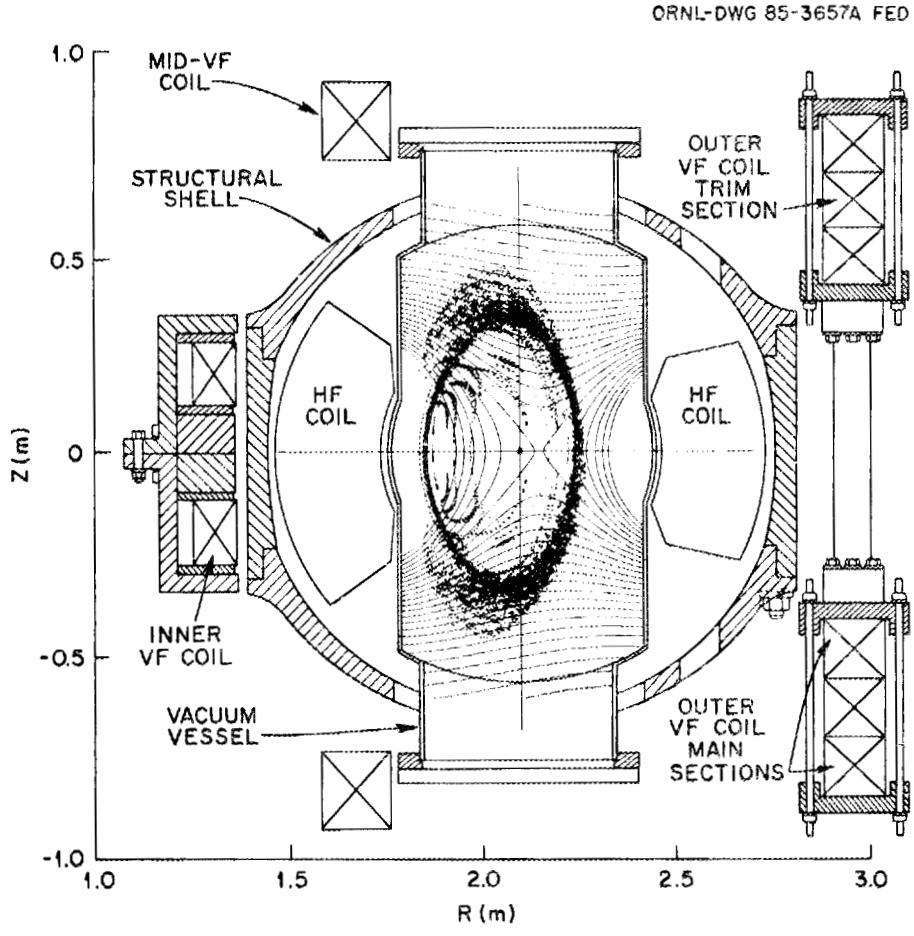

Fig. 2. Cross section of the ATF at the $\phi = 0^{o}$ location. The apparent unequal cross section of the helical coils is due to the different angles at which these coils cut the $\phi = 0^{o}$ plane at small and large R. Also shown are |B| contours and intersections with the $\phi = 0^{o}$ plane of 1-keV H^{+} orbits launched at $r/\bar{a} = 0.95$.

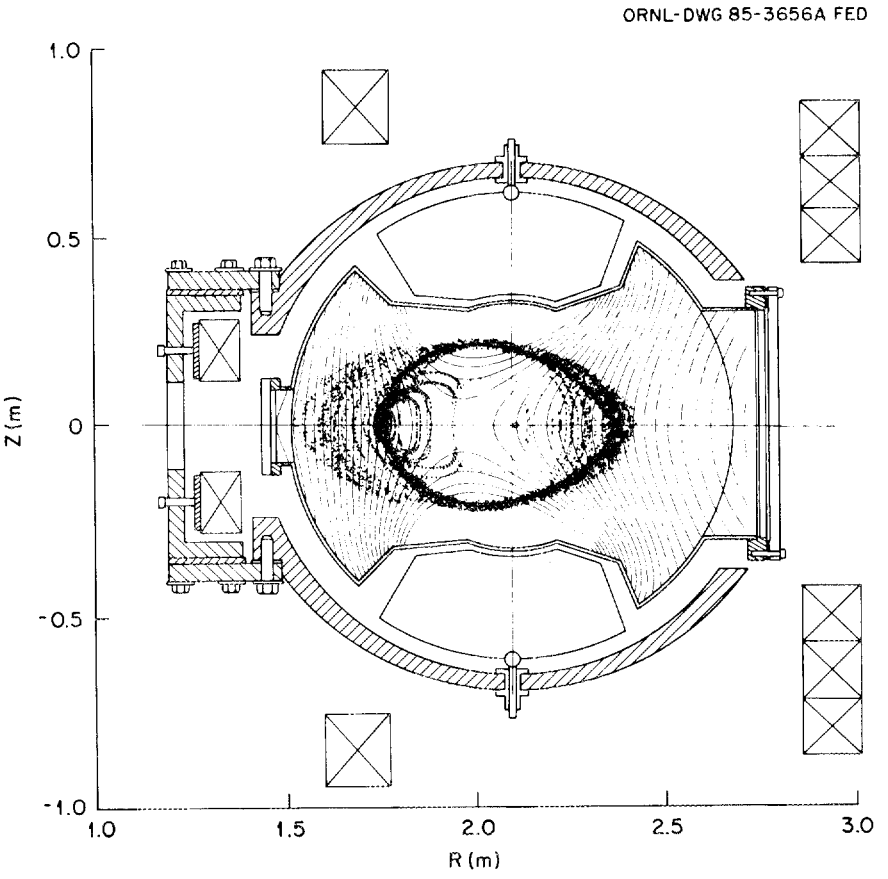

Fig. 3. Cross section of the ATF at the $\phi = 15^{o}$ location. The |B| contours and the orbit punctures are the same as in Fig. 2.

TABLE I

ATF Device Parameters

Size	
Major radius R	2.1 m
Average plasma radius $\bar{a}$	0.3 m
Average HF coil radius a_c	0.46 m
Vacuum vessel radius (inside)	0.58 m
Structural shell radius (inside)	0.66 m
Plasma volume	3.7 m^3
Vacuum vessel volume	10.5 m^3
Vacuum vessel interior	≈1.16 by 0.65 m
Plasma-wall separation	0.05-0.2 m
Field	
Magnetic field on axis B_0	2 T, 5-s pulse
	1 T, continuous
Plasma Heating	
40- to 50-kV H^0 NBI	3 x 1.5 MW, 0.3 s
53.2-GHz ECH	2 x 0.2 MW, cw
5- to 30-MHz ICH	0.4 MW, cw
40- to 80-MHz ICH	1.5 MW, <30 s

of stellarator configurations and was specifically optimized for high-beta operation in the second stability region and for configuration flexibility. This optimization led to the selection of the magnetic configuration parameters ℓ, M, R/a_c, $R/\bar{a}$, $\iota(\bar{a})$, $\iota(0)$, and $\Delta V'$ defined in Table II.

The novel stellarator parameters are the small plasma aspect ratio, the large plasma volume (3.7 m^3 vs 1.6-1.7 m^3 in Wendelstein VII-AS [3,4] and Heliotron-E [5]), and the steady-state field capability at B = 1 T. The main parameters of the largest world stellarator experiments [4-9] are listed in Table III. A shearless configuration with low transform and a magnetic well is being studied in Wendelstein VII-A [7] and will be studied in modular form in Wendelstein VII-AS. The other extreme, a high-shear, high-transform configuration with a vacuum magnetic hill, is being studied in Heliotron-E. The ATF occupies an intermediate position.

The high-beta capability is the result of a configuration optimization process. The resulting rotational transform profile places surfaces with low-order rational rotational transform (field line resonances) inside a magnetic well or in high-shear regions. The magnetic well deepens with beta such that the plasma does not become unstable. This beta-self-stabilizing effect is referred to as stable access to the second stability region. The inherent flexibility of the coil sets allows external control of the rotational transform profile so that it can be kept close to the (optimal) vacuum profile as beta increases.

The good confinement properties predicted for ATF arise from a combination of physics and design factors. The self-consistent radial electric field required for ambipolarity produces a poloidal $\vec{E} \times \vec{B}$ orbit rotation and consequently a large reduction in both direct orbit losses [10] and diffusive losses [10-12]. The vacuum vessel and HF coils are designed so that almost all collisionless orbits that cross the plasma boundary (the $\iota = 1$ surface), the usual loss region, reenter the plasma before hitting the vacuum wall. Additionally, the tangential neutral beam injection (NBI) path is such that $|v_{\parallel}/v| \gtrsim 0.9$, so that fast ions are deposited far from the potential loss region at

TABLE II

ATF Magnetic Configuration Parameters

Helical field coil winding law	$\phi = \ell\theta/M$
Multipole order ℓ	2
Number of toroidal periods M	12
HF coil aspect ratio R/a_c	4.6
Plasma aspect ratio $R/\bar{a}$	7
Edge rotational transform $\iota(\bar{a})$	0.95
Central rotational transform $\iota(0)$	0.35
Vacuum magnetic well depth $\Delta V'$	0.7%

TABLE III
Principal Large World Stellarator Facilities

Device	Location	Start Date	R (m)	a (m)	B (T)	Pulse Length (s)	ℓ	$\iota(0)$	$\iota(a)$	Main Feature
L-2	U.S.S.R.	1976	1	0.11	2	0.03	2	0.2	1.0	Stellarator
W VII-A	F.R.G.	1976	2	0.1	3.5	0.5	2	0.2 -0.6	0.2 -0.6	Shearless
Heliotron-E	Japan	1981	2.2	0.2	2	0.5	2	0.6	2.5	High ι, shear
URAGAN-3	U.S.S.R.	1982	1	0.13	2.5	0.5	3	0	0.6	Divertor
W VII-AS	F.R.G.	1986	2	0.2	3	10	2	0.38	0.38	Modular coils
ATF	U.S.A.	1986	2.1	0.3	2	30,000	2	0.35	0.9	Flexibility
TJ-II	Spain	1989	1.5	0.25	1	0.5	-	1-3	1-3	Helical axis

small $v_{\parallel}/v$. Transport code calculations incorporating a self-consistent radial electric field indicate that $\langle\beta\rangle \gtrsim 5\%$ and $T_i(0) \gtrsim$ 4 keV are attainable with 4 MW of NBI power at B = 1 T.

The engineering design of the ATF [13-16] permits operation for up to 5 s at full field (2 T) and steady-state operation at half-field, provides large access ports for heating and diagnostics, and allows parallel fabrication of the major components to shorten the construction time. Although parallel fabrication allows a one-piece vacuum vessel, it also requires segmented HF coils with mechanical joints. Innovative techniques were developed to construct the HF coils and vacuum vessel and to ensure the high degree of accuracy (typically 1 part in 10^3) needed in fabrication and assembly. The principal features of the ATF are listed in Table IV and discussed throughout the paper.

The support systems are another important consideration in the ATF design. The initial power supplies and planned upgrades are consistent with the demands of 5-s pulsed operation at 2 T and steady-state operation at 1 T, and they provide the control and flexibility required for the magnetic configuration studies. Currentless plasma startup will be provided by fundamental and second harmonic electron cyclotron heating (ECH) with 0.4 MW of 53.2-GHz cw ECH power. The primary plasma heating will be provided by 4.5 MW of pulsed (0.3-s) tangential 40-kV H^0 beams and supplementary cw ICH (0.4 MW at 5-30 MHz and 1.5 MW at 40-80 MHz).

This paper describes the ATF torsatron, the physics and engineering reasons for the different design choices, and the expected capabilities of the device. Section II discusses the reasons for choosing a stellarator configuration for the ATF, the optimization of the magnetic configuration, and the selection of the ATF parameters. Section III discusses the specific properties of the optimized torsatron configuration, high-beta and confinement issues, the projected performance, relevant plasma heating physics, and issues related to power and particle removal. Section IV describes general design considerations, the HF coil system, the poloidal coil systems, the vacuum vessel, the machine support structure, and the accuracy

TABLE IV

Main ATF Characteristics and Reasons for Their Selection

Characteristic	Reason
Low $R/\bar{a}$	Second stability region, larger $\bar{a}$
No OH transformer, no TF coils	Currentless plasma operation
Three PF (VF) coil sets	Wide range of magnetic configurations
Two independent HF coils	Helical-axis capability
Segmented HF coils with joints	Parallel construction of HF coils and vacuum vessel
Contoured vacuum vessel	Maximum distance from plasma, HF coil assembly needs
Thin vacuum vessel	All magnetic loads on coils and thick shell, fast penetration of poloidal fields
Large access ports	Tangential NBI; access for ICH, diagnostics
High precision in construction and assembly	Minimize magnetic field perturbations and impact on flux surfaces

required in construction and assembly. Section V describes the support systems (power supplies and plasma heating). Section VI gives a brief summary and indicates future directions for the ATF program. The appendix discusses the optimization methodology and the results that led to selection of the torsatron configuration.

II. ATF PHYSICS DESIGN ISSUES

The goal of the ATF design program was to define a facility that can demonstrate the principles of high-beta, steady-state operation and advance the understanding of toroidal confinement. Toroidal confinement devices are characterized by helical (toroidal plus poloidal) magnetic fields that form toroidally nested, closed magnetic surfaces. Their confining magnetic fields can be generated by internal plasma currents, as in a tokamak, or by currents in external windings, as in a stellarator. These devices obtain the highest plasma parameters of any confinement configuration.

II.A. Selection of the Stellarator Concept for the ATF

The stellarator was selected to carry out the ATF mission because of some important inherent advantages, the level of tools available for theoretical optimization, and the high level of plasma performance attained in stellarators in recent years.

Toroidal confinement systems with external windings have the advantages of inherent steady-state operation and external control of the magnetic configuration parameters. Other advantages are no need to drive a net plasma current, startup on closed magnetic surfaces, and elimination of disruptions and other current-driven phenomena. External control of the magnetic confinement geometry and the variety of possible configurations allow experimental optimization of performance (second stability region for high beta, plasma shaping to control rotational transform, etc.) and flexibility to study the basic "building blocks" of toroidal confinement (rotational transform, shear, magnetic well, magnetic axis topology, electric field, etc.).

The level of stellarator theory has advanced in recent years [17-21], and computational tools are now available for theoretical optimization of stellarator configurations and maximization of flexibility in the magnetic configuration. The theoretical optimization of the configuration is carried out to obtain maximum beta capability. The maximization of flexibility provides for experimental optimization and for study of the widest possible range of stellarator configurations.

Significant experimental advances in the stellarator field in recent years [1,19,20] have also made this concept more attractive for fusion-relevant studies. Plasma performance in Heliotron-E [22-26] and in Wendelstein VII-A [7,27,28] is comparable to that obtained in tokamaks of larger size, magnetic field strength, and auxiliary heating power. Some recent experimental results are given in Table V.

II.B. Selection of the ATF Magnetic Configuration

Selection of a specific magnetic configuration for the ATF [29] involved examining a large number of stellarator geometries using an extensive set of physics design tools: three-dimensional (3-D) magnetic field calculations, 2-D and 3-D MHD equilibrium and stability codes, and 3-D guiding center particle orbit codes. The evaluation procedure is described in the appendix. All magnetic fields used in these calculations were derived from realistic coil models, rather than from approximate analytic field representations, to ensure an accurate engineering realization of the configurations studied.

The MHD studies were the most sensitive to variations in the vacuum field structure and played a dominant role in finding an optimum configuration for a particular stellarator geometry. The orbit studies and engineering studies established limits on configurations by indicating when configuration changes became extreme enough to be unacceptable — for example, by producing large particle losses or requiring very tight coil bend radii.

The aim of the evaluation studies was to identify the type of stellarator configuration best suited for the ATF mission and to restrict its parameter range for the optimization studies. The primary criteria were maximum beta capability, good confinement

TABLE V

Current-Free Stellarator Parameters

Experiment	$\bar{n}$ (10^{13} cm^{-3})	T_i (keV)	T_e (keV)	$\langle\beta\rangle$ (%)	$\bar{n}\tau_E$ (10^{12} cm^{-3}-s)	P_{abs} (MW)
Heliotron-E	1.0	0.33	1.1	0.08	0.24	0.2
B = 1.9 T	1.9	1.04	0.8	0.2	0.6	0.66
	7.2	0.6	0.6	0.6	2.4	1.2
	0.9	0.18	1.0	0.25	0.16	0.15
B = 0.94 T	7.8	0.35	0.35	2.0	1.6	0.7
Wendelstein VII-A						
B = 3 T	10	1.0	0.8	0.3	---	0.4
B = 1.25 T	0.8	---	2.3	---	0.03	0.18

characteristics (assuming reasonable electric fields), a large plasma radius, and the flexibility to allow changes in the magnetic configuration characteristics over a reasonable range. Additional considerations were relative cost, engineering difficulty, construction time, and similarity to existing experiments.

The configurations considered were limited to the modest coil aspect ratios ($R/a_c \approx 3$–5) and configuration parameters appropriate to a near-term physics experiment. The vacuum field configurations were required to have magnetic surfaces with moderate plasma aspect ratio ($R/\bar{a} \approx 6$–12), average radius $\bar{a} \approx 20$–30 cm, substantial transform ($\iota_{max} > 0.5$), and a magnetic well and/or shear. Configurations with parameters outside these limits were also studied in order to determine trends. The range of stellarator configurations examined is illustrated in the appendix by Fig. A.4 and Table A.III.

The main criterion used in optimizing the stellarator configuration for the ATF was high beta capability. Figure 4 illustrates how two factors, equilibrium limitations and MHD instability thresholds, determine the achievable beta. The equilibrium beta limit, which increases with the plasma aspect ratio ($A \approx R/\bar{a}$), arises from an outward (Shafranov) shift of the magnetic axis, $\delta/\bar{a} \approx \beta/(\iota^2 A)$, induced by the generation of parallel (Pfirsch-Schlüter) currents as the plasma pressure increases. This phenomenon is basically the same as in tokamaks. Large toroidal shifts can cause a topology change by bringing a separatrix into the plasma, thus destroying the equilibrium. In the stellarator, the toroidal shift also induces symmetry-breaking components that can destroy magnetic surfaces and thus limit the achievable beta. This is particularly important for low-shear systems because the size of magnetic islands depends inversely on the square root of the local magnetic shear. The moderate-shear ATF relies on varying the poloidal field shape as beta increases to conserve flux and thus avoid the change of topology induced by the toroidal shift.

The MHD stability is determined by the pressure gradient, which is the main source of free energy in a stellarator, and the magnetic field line curvature (shear, magnetic well/hill), which is mostly

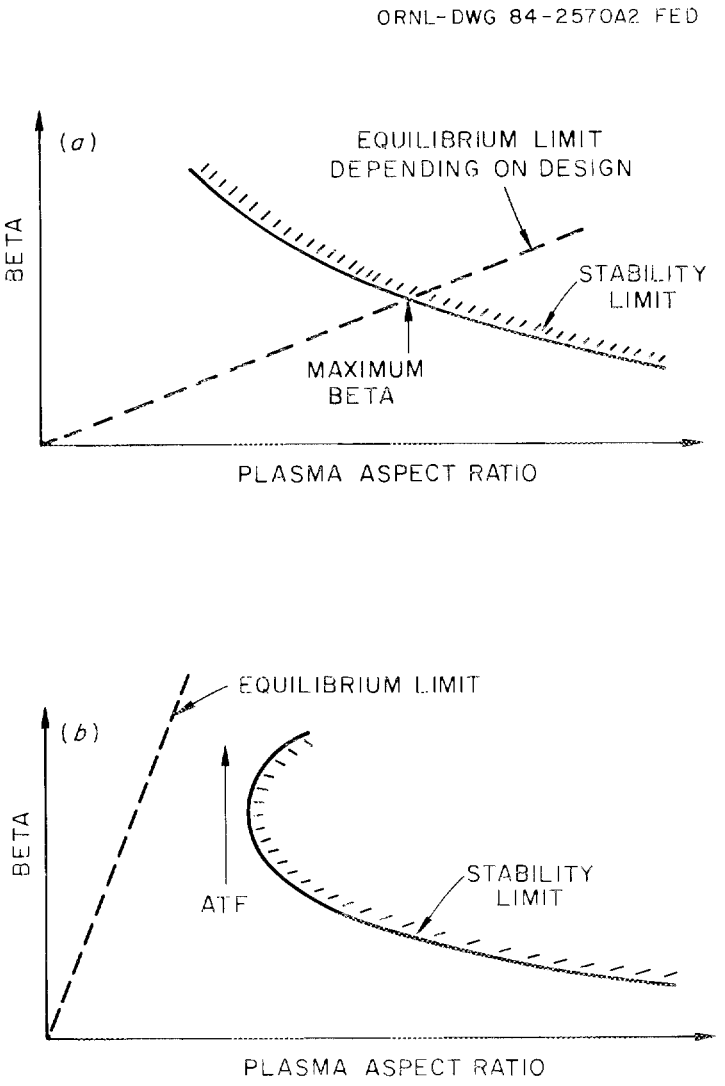

Fig. 4. Equilibrium and stability limits on maximum beta achievable in stellarators. (a) In a conventional design, maximum beta occurs at $R/\bar{a}$ = 10-20. (b) The ATF design uses the second stability region (indicated by the arrow) and profile control to give higher beta (limited by equilibrium) at lower $R/\bar{a}$ (~7).

determined by currents in external coils. The stability limit decreases as the aspect ratio increases and the toroidal curvature decreases. The free energy available to drive the instability increases as beta increases, but the accompanying outward magnetic axis shift increases the magnetic well depth and changes the magnetic field line curvature. If the well depth increases fast enough with beta, there is a beta-self-stabilization effect [30], and the MHD stability improves with beta [Fig. 4(b)]. This results in stable access to the so-called second stability regime for the pressure-driven modes. At high beta the induced Pfirsch-Schlüter currents can be large enough to destabilize kink modes. However, these modes have a weaker growth rate than in tokamaks, and the combined effect of coupling to stable interchange modes and wall stabilization is effective for the stabilization of these modes [31].

From the evaluation described in the appendix, the $\ell = 2$ torsatron emerged as the most promising configuration on which to base the ATF design. The cost and engineering constraints had basically determined the size and field for the device. Therefore, the aspect ratio A and the number of field periods M were the only free parameters remaining to fix the design of the helical coils. In this situation, it was possible to determine these parameters through an optimization study, which was done in two steps. First, the optimal pitch parameter, $p = M/\ell A_c$, of the helical coil was found. Once the pitch was fixed, a relation between the aspect ratio and the number of field periods was established, and the optimization was reduced to a single parameter search. Then, the second step was carried out by looking for the configuration with optimal MHD properties; that is, the highest equilibrium and stability critical beta β_c.

To find the optimal pitch parameter, the vacuum field properties of many (~100) configurations were studied [29,32]. These properties are very sensitive to the pitch of the helical coils, as illustrated in Fig. 5, which shows three configurations with the same coil aspect ratio but with different pitch p ($\propto$ M). The lowest-pitch case, $p = 1.14$, has a small radius for the outermost flux surface and practically no shear. The highest-pitch case, $p = 1.71$, has large volume utilization

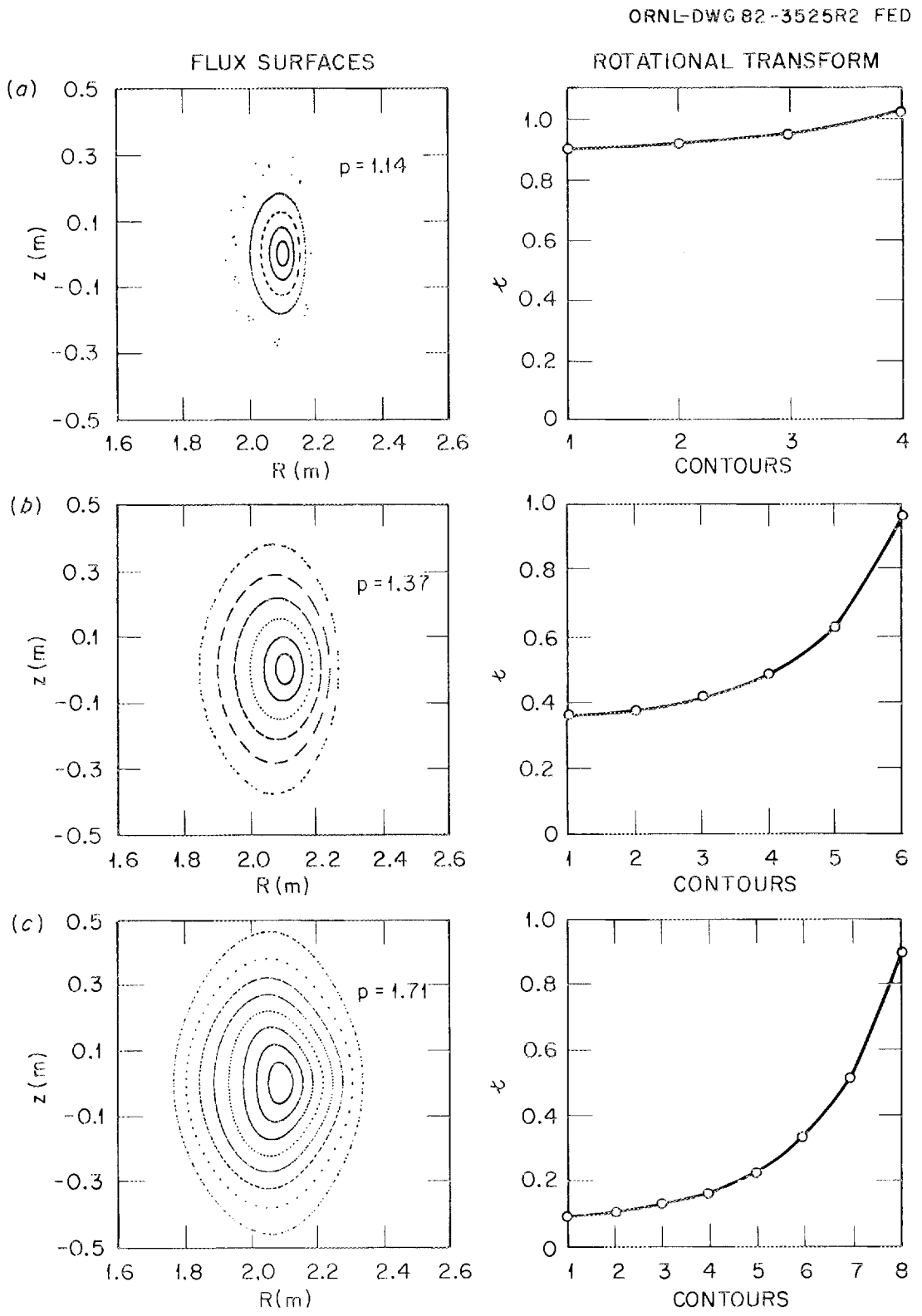

Fig. 5. Magnetic surfaces and rotational transform profiles for $\ell = 2$ torsatrons with the aspect ratio $R/a_c \approx 4.4$ and (a) winding pitch $p = 1.14$, (b) $p = 1.37$ (ATF), and (c) $p = 1.71$.

but high transform and shear only on the outer surfaces, which are lost when finite-size coils are used and allowance is made for plasma-wall spacing. The case with $p = 1.37$ is a good compromise between plasma size, shear, and transform. Therefore, a pitch parameter close to 1.4 is optimal for an $\ell = 2$ torsatron. A similar result ($p = 1.31$) has been found in Heliotron studies.

In the second step of the optimization process, a constant-pitch ($p = 1.37$) scan was used to investigate the equilibrium and stability properties of torsatrons as a function of aspect ratio. Figure 6 shows the configurations studied in the constant-pitch scan. Configurations with $M < 7$ were eliminated because at these M values the magnetic axis of the vacuum configuration bifurcates. Figure 7 shows the radial variation of ι and $[V' - V'(0)]/V'(0)$ for these configurations, where $V' = \int d\ell/B$ for these configurations. The plasma aspect ratio increases with M in the same proportion as the coil aspect ratio, $R/\bar{a} \simeq 0.62M \simeq 0.58R/a_c$. Both the central and edge rotational transforms increase with M, but the global shear is approximately constant, $[\iota(\bar{a}) - \iota(0)]/\iota(0) \simeq 2$, for $M \geq 12$. These approximately constant ratios are a consequence of the constant pitch of these configurations. The vacuum magnetic well decreases in depth with increasing M and vanishes for the $M = 24$ case in Fig. 7(b).

To compare the equilibrium properties of different configurations it is useful to evaluate an equilibrium critical beta. A true definition of equilibrium critical beta for a 3-D configuration is not easy to give. However, a practical way to make the comparison is to define the equilibrium critical beta as the value of beta at which the magnetic axis shift attains a value of one-half the minor radius. Figure 8 shows the variation of the magnetic axis shift with central beta for the $M = 12$ configuration. The value of critical beta increases with aspect ratio along the constant-pitch sequence. However, the improvement is not a strong function of aspect ratio. It is clearly not as strong as suggested by the often-used expression $\beta_c = \iota(\bar{a})^2/A \propto M$, which is based on a low-beta estimate of the magnetic axis shift [33].

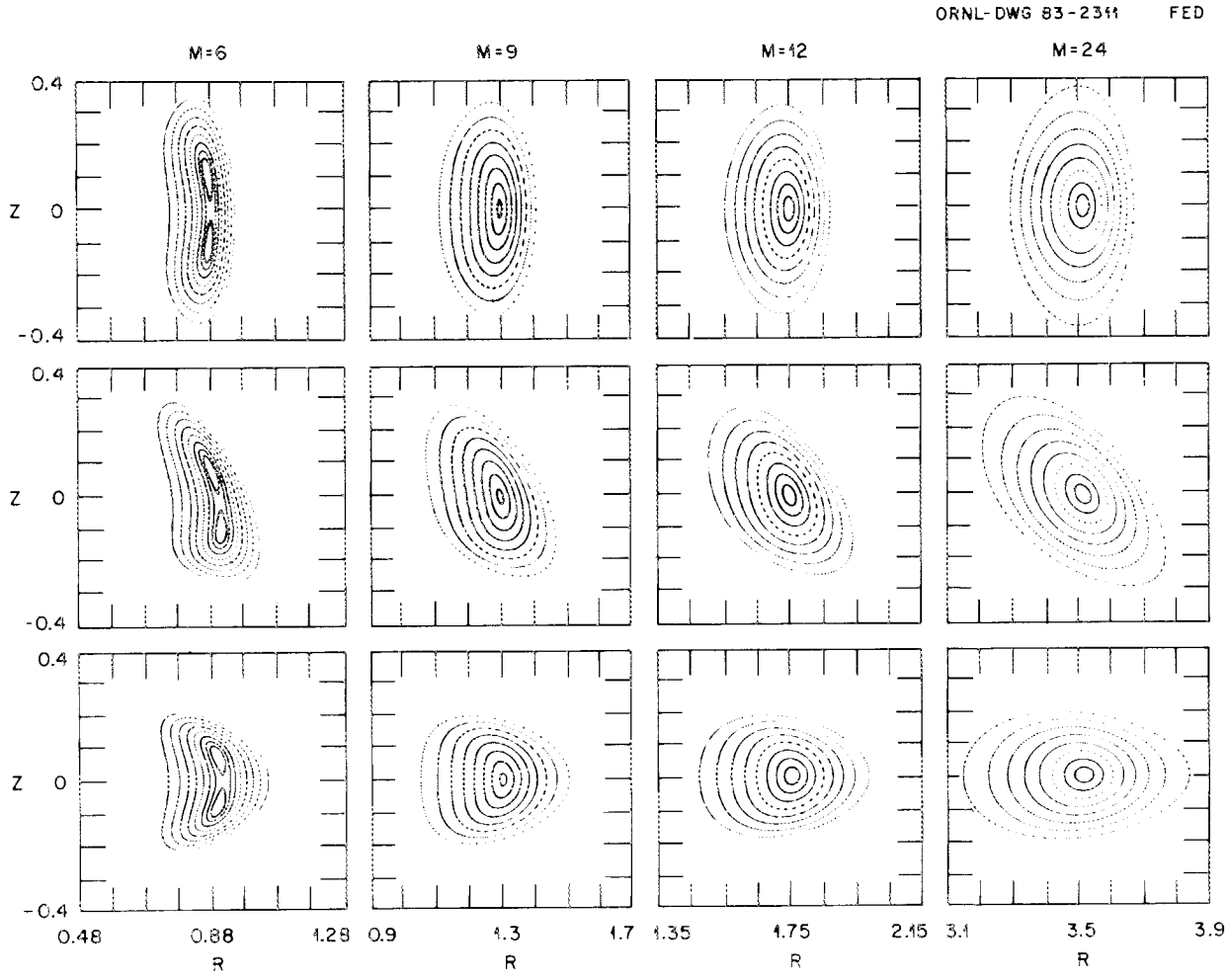

Fig. 6. Vacuum magnetic surfaces at the beginning (top), one-quarter (middle), and one-half (bottom) of a toroidal field period for M = 6, 9, 12, and 24 in the constant-pitch configuration scan.

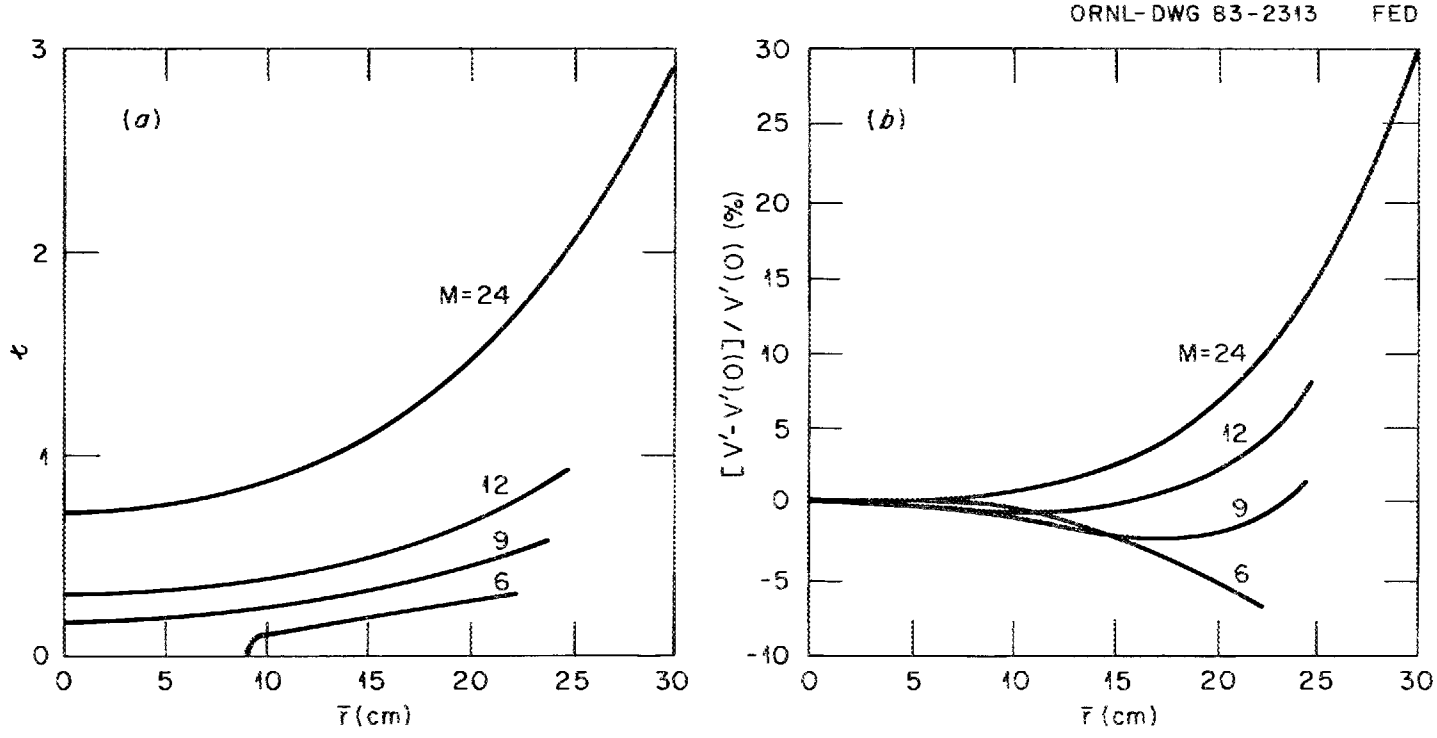

Fig. 7. Vacuum field properties for the constant-pitch configuration scan. (a) ι vs $\bar{r}$. (b) $[V' - V'(0)]/V'(0)$ vs $\bar{r}$.

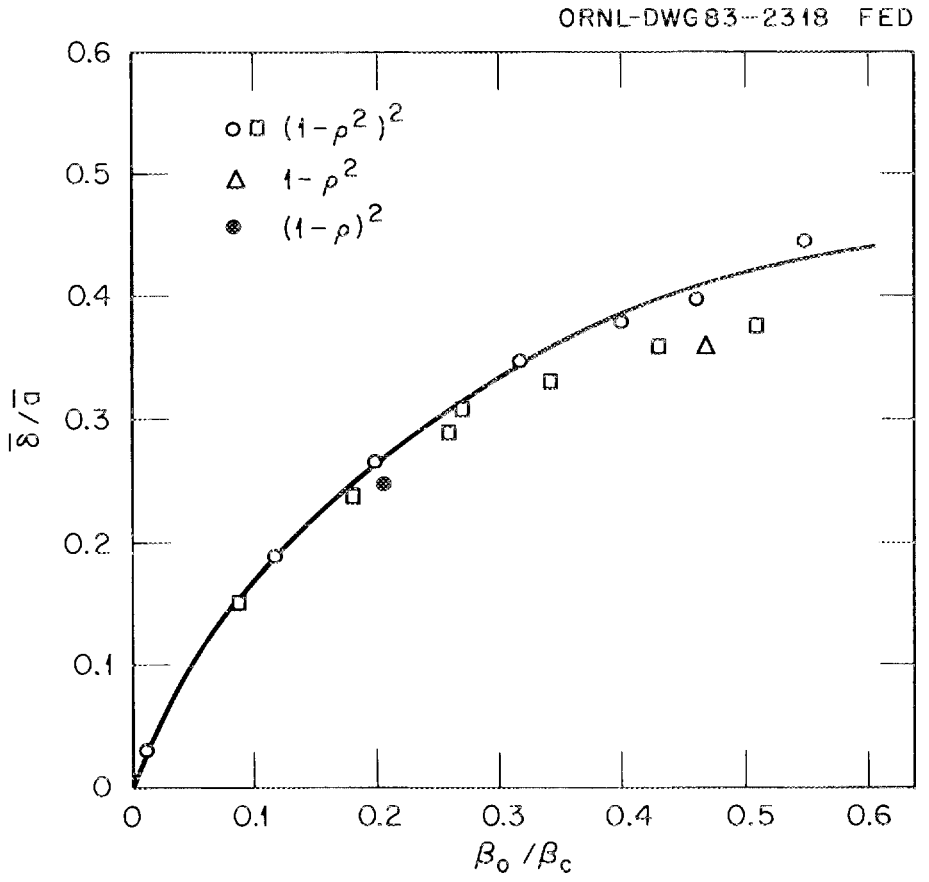

Fig. 8. Normalized magnetic axis shift for the M = 12 configuration for different radial profiles of the plasma pressure, where $\rho = r/\bar{a}$.

The stability properties are rather more sensitive to the aspect ratio. For fixed beta, the linear growth rate of the low-n modes decreases strongly with aspect ratio, and the plasma becomes stable for $M < 13$ (Fig. 9) [33]. This stabilizing effect has been correlated with the absence of low-order rational surfaces in the magnetic hill region ($V'' > 0$). Figure 10 shows the relationship of the low-order rational surfaces to ι_c, the transform at the critical surface where $V'' = 0$, for the vacuum field of the configurations in the constant-pitch scan. The shaded regions show the sections of configuration space where low-order rational surfaces lie inside the plasma but outside the critical surface (where V" changes from stabilizing to destabilizing). In this stability window, the beta-self-stabilization effect dominates, and the plasma can have direct access to the second stability regime.

The equilibrium and stability results for the constant-pitch scan are combined in Fig. 11. Computational difficulties due to either numerical problems of grid resolution in the high-pressure-gradient regions or actual breakup of magnetic surfaces prevent calculation of higher-beta equilibria than those indicated. From these studies [33,34] we concluded that the optimal value of M is the highest one in the stability window. This led to selection of the $M = 12$ case as the optimal torsatron configuration.

While the HF coil geometry was designed to produce the optimum equilibrium and MHD stability properties for the standard ATF configuration, the PF coil systems were designed for maximum flexibility to provide access to a wide range of magnetic configurations, as discussed in Sec. III.A. A minimum of three sets of coils was required to independently control the rotational transform and the magnetic well without generating a net plasma current [35].

II.C. Selection of the ATF Device Parameters

The optimization process discussed in Sec. II.B led to the specification of the HF and VF coil sets shown in Fig. 12 and of the normalized coil currents and sizes given in Table VI. The heights of the

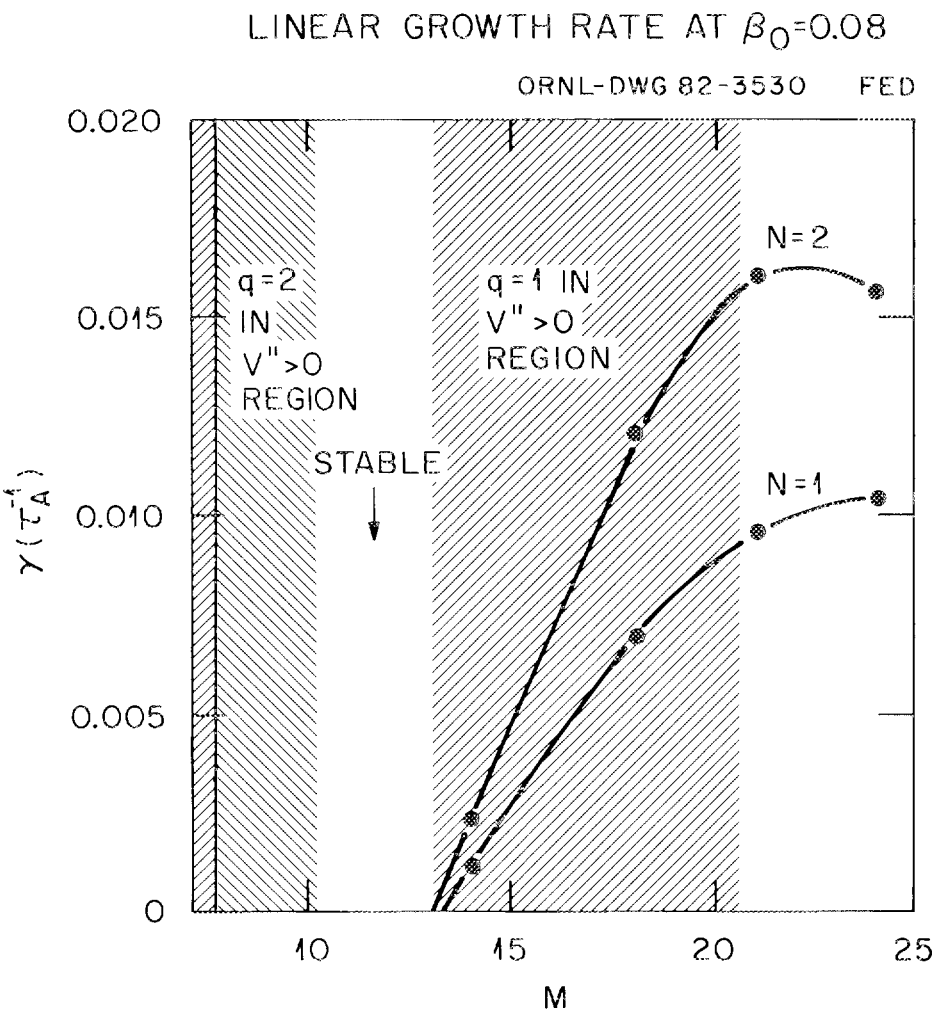

Fig. 9. Linear growth rates (in units of the inverse of the Alfvén time) for n = 1 and n = 2 modes for the constant-pitch configuration scan. The stable window between M = 10 and M = 13 has no principal resonance outside the magnetic well.

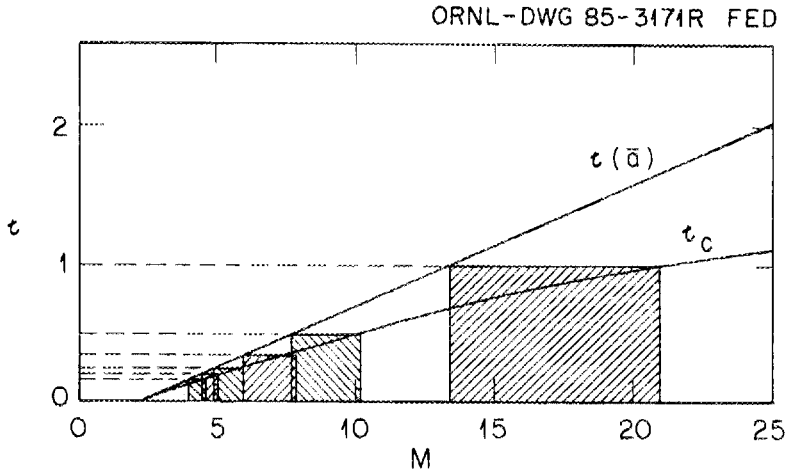

Fig. 10. Location of the principal low-order rational resonances ($\iota = 1, 1/2, 1/3, 1/4, 1/5$, etc.) relative to critical ι values for configurations in the constant-pitch scan. Configurations in the window (nonshaded area) between $M = 10$ and $M = 13$ have no principal resonances between the high-beta boundary of the stabilizing magnetic well and the plasma edge.

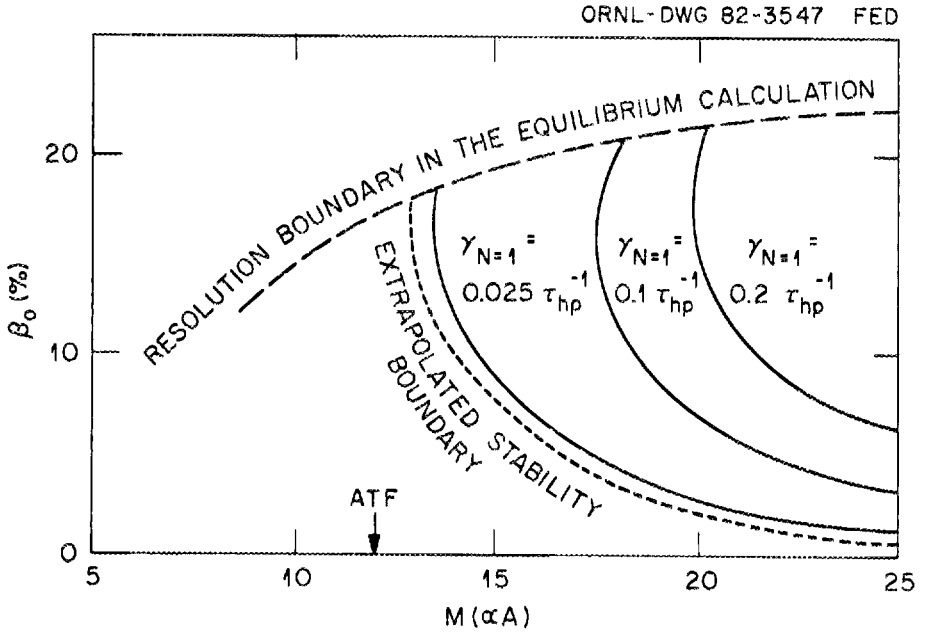

Fig. 11. Combined equilibrium and stability constraints for the constant-pitch configuration scan. The $n = 1$ instability growth rates are in units of the inverse of the poloidal Alfvén time.

ORNL-DWG 85-3124 FED

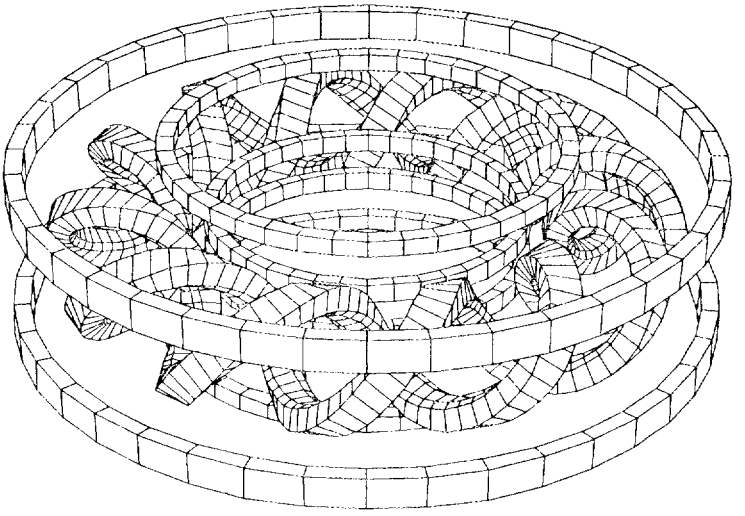

Fig. 12. The ATF coil sets.

TABLE VI

ATF Coil Specifications

Parameter	HF	Inner VF	Mid-VF	Outer VF
R/R_0	1	0.633	0.805	1.40
a_c/R_0	0.218	----	----	----
Z/R_0	----	$\pm$0.095	$\pm$0.405	$\pm$0.305
I/I_h	1	0.15	0	-0.47

inner, outer, and mid-VF coils were chosen to allow adequate space for the diagnostic ports. The device parameters (given in Table I) were determined by the following considerations.

The machine size ($R = 2.1$ m, and hence $a_c = 0.46$ m and $\bar{a} = 0.3$ m) was determined mainly by constraints on the device cost, which scales approximately as the total mass and hence roughly as R^3B^2 for constant material stress levels. Other important constraints were a plasma large enough not to be dominated by edge effects and adequate separation of the plasma edge and the vacuum wall. The plasma edge region (typically 5-10 cm) is characterized by atomic processes (charge exchange, ionization, impurity radiation) and by the edge magnetic geometry (magnetic islands or broken flux surfaces near $\iota = 1$ and the divertor-like scrapeoff layer associated with the separatrix outside the $\iota = 1$ surface). The plasma-wall separation in ATF varies from 5-10 cm under the helical coils to 20 cm at the outside (large R).

The magnetic field strength ($B = 1$ T for steady state and 2 T for 5-s pulses) is determined by a combination of physics (availability of ECH for currentless operation), engineering (coil heating, power supplies, forces, structure), and cost considerations. The desire to shorten construction time led to the choice of jointed HF coils. These joints restrict steady-state operation to 1 T, due to the difficulty of cooling the joint region, and pulsed (5-s) operation to 2 T, due to stresses in the joints. The maximum current density is 3 kA/cm^2 at 2 T. The steady-state HF power requirement at 1 T is 22.5 MW, a level compatible with upgraded power supplies and cooling towers at ORNL. The forces at 2 T (maximum 2 MN/m radial and 1 MN/m axial) are consistent with a toroidal shell support structure that allows large outside diagnostic ports (0.6 by 0.9 m) and with a large number (10^4) of full-field pulses.

The ATF has no toroidal field (TF) coils because they would limit access to the plasma and increase the magnetic loads on the device, thus restricting the allowable currents in the other (HF and VF) coils. However, the ATF has been designed to accept 0.5-T TF coils (and the resulting forces) to allow the possibility of a future upgrade for stellarator-tokamak hybrid operation. Such an upgrade would

also require addition of high-power lower hybrid current drive or a large ohmic heating (OH) transformer to sustain the plasma current.

III. ATF PHYSICS CAPABILITIES

The capabilities of the optimized ATF torsatron are determined by its vacuum magnetic configuration characteristics, its high-beta and transport properties, and its auxiliary systems (plasma heating, energy and particle removal, etc.).

III.A. Properties of the ATF Vacuum Magnetic Configuration

The standard ATF vacuum magnetic configuration, defined by the relative coil parameters in Table VI, is illustrated in Fig. 13. The effect of finite toroidicity is apparent. The corresponding $\ell = 2$ system in the straight (infinite-aspect-ratio) limit has magnetic surfaces with elliptical cross sections that rotate poloidally by an angle $\theta = 6\phi$ as the toroidal angle ϕ increases. The finite-aspect-ratio effects produce a deviation from the pure elliptical shape. As can be seen in Fig. 13, the elongation of the magnetic surfaces varies from 1.96 at $\phi = 0^{\circ}$ to 1.55 at $\phi = 15^{\circ}$, and the surfaces near $\phi = 15^{\circ}$ have pronounced triangularity.

The plasma size is characterized by the average radius $\bar{a}$ of the "last" closed flux surface, beyond which the magnetic field is ergodic (a magnetic limiter) or displays a separatrix (a magnetic divertor). For the ATF case, we assume that the plasma edge is given in practice by the $\iota = 1$ surface as a result of the sensitivity of this resonance surface to magnetic island formation. However, flux surfaces exist at larger radius, as shown by the vacuum field calculations.

The rotational transform profile for the standard ATF configuration, shown in Fig. 14(a), is the result of the MHD optimization studies described in the appendix. The $q = 1$ and $q = 3$ surfaces are excluded from the plasma since $\iota(r)$ varies from 0.35 at the center to 0.95 at the edge. The $\iota = 0.5$ surface falls within a magnetic well, and the low-order resonances for $0.5 < \iota < 1$ fall in a region of higher shear.

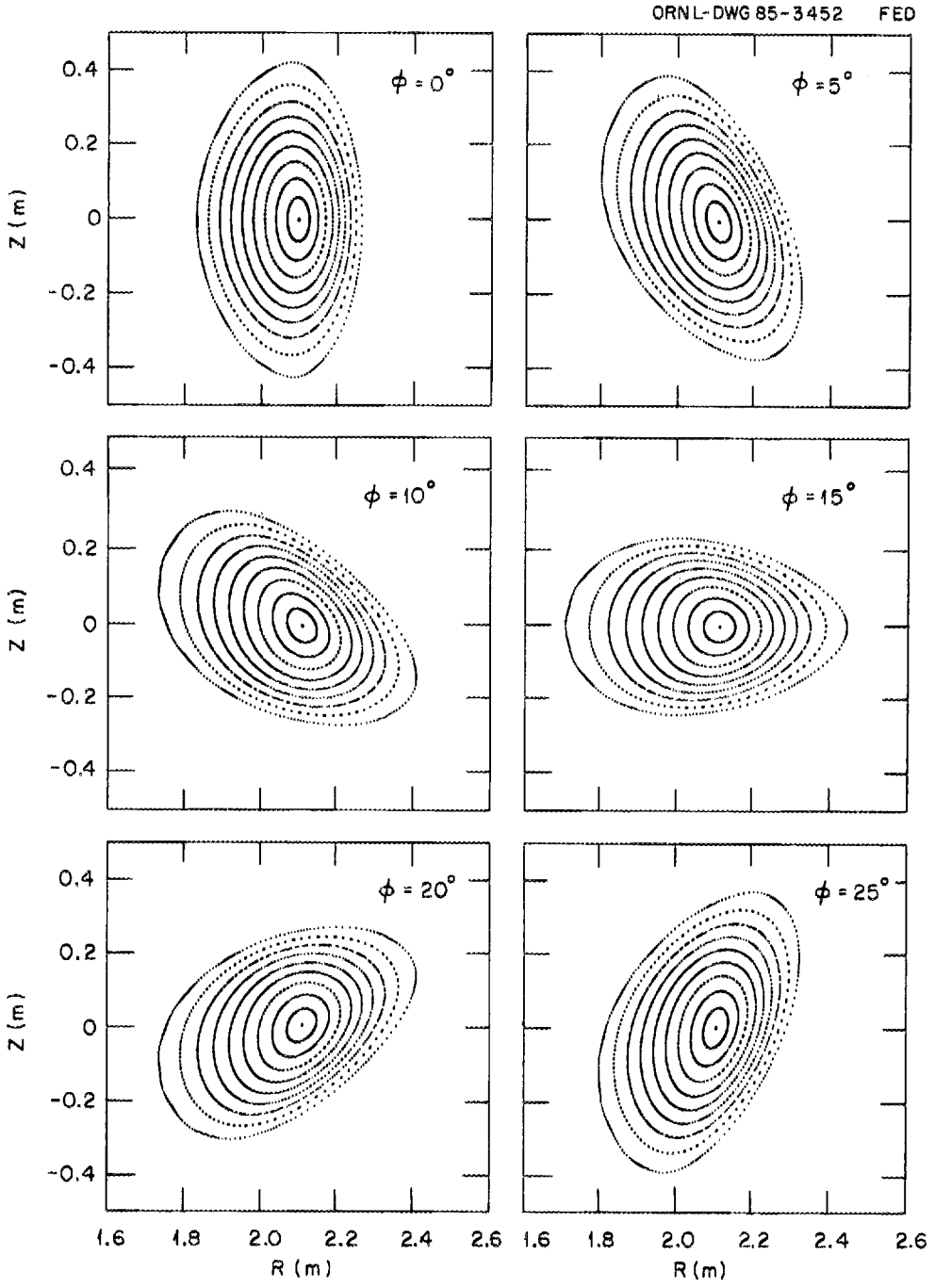

Fig. 13. Cross sections of magnetic flux surfaces for the standard ATF configuration every 5° toroidally in a 30° (M = 12) field period.

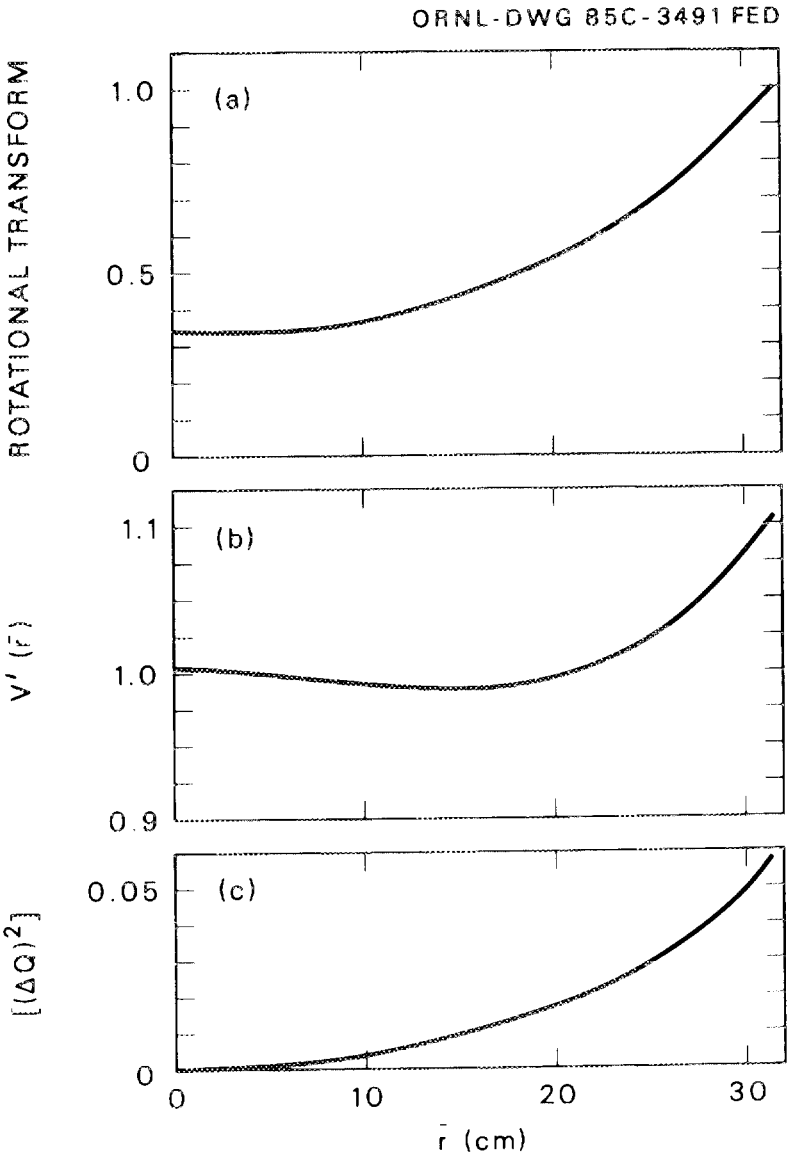

Fig. 14. Radial variation of (a) rotational transform ι, (b) $V' = \int d\ell/B$, and (c) $(\Delta Q)^2$ for the standard ATF configuration.

The outward displacement of the magnetic axis relative to the center of the last closed flux surface in Fig. 13 indicates the existence of a vacuum magnetic well. This is seen more clearly in Fig. 14(b), which shows V' as a function of the average radius $\bar{r}$. Here $V' = \oint d\ell/B$ is the derivative with respect to the toroidal flux $\Phi = \int dV\, \vec{B}\cdot\nabla\phi/2\pi$ of the volume V enclosed in a flux surface. If $V'(\bar{r})$ has a minimum V'_{min} at $\bar{r}_{min}$, the configuration has a magnetic well. The region of the magnetic well corresponds to $V'' < 0$, and that of the magnetic hill to $V'' > 0$. A quantitative measure of the magnetic well depth is given by $\Delta V' = [V'(0) - V'_{min}]/V'(0)$. For the standard ATF vacuum configuration, $\Delta V'$ is 0.7%. The magnetic well has a stabilizing effect on interchange modes. In ATF the combination of magnetic well for $\bar{r} < \bar{r}_{min}$ and shear for $\bar{r} > \bar{r}_{min}$ stabilizes the dominant resonant modes.

In addition to transform, shear, and well depth, another parameter that characterizes a magnetic configuration is the poloidal variation on a flux surface of $Q = \int_{FP} d\ell/B$, integrated along a field line over one field period. The average value of Q on a flux surface is V'. The poloidal variation ΔQ about the average value V' is directly related to the Pfirsch-Schlüter current, since $j_{\parallel}/j_{\perp} \propto \Delta Q/V'$, and therefore to the shift of the magnetic axis. The normalized mean square value of ΔQ increases with the average radius, as shown in Fig. 14(c).

The |B| contours are basically quadrupolar ($\ell = 2$) and rotate with the twist of the helical coils, as shown in Fig. 15, and the saddle point in the |B| contours shifts with respect to the magnetic axis of the flux surfaces. The magnetic field variation along a field line [helical field ripple $\Delta = (B_{max} - B_{min})/(B_{max} + B_{min})$ is relatively small ($\Delta = 0.004$) on the magnetic axis but rises to a large value ($\Delta = 0.345$) at the plasma edge ($\iota = 1$). Modeling each HF coil with a single filament and with six filaments gives essentially the same |B| contours and flux surfaces inside the last closed flux surface. Differences are important only near the HF coils, and then six (or more) filaments are used to obtain a better field representation.

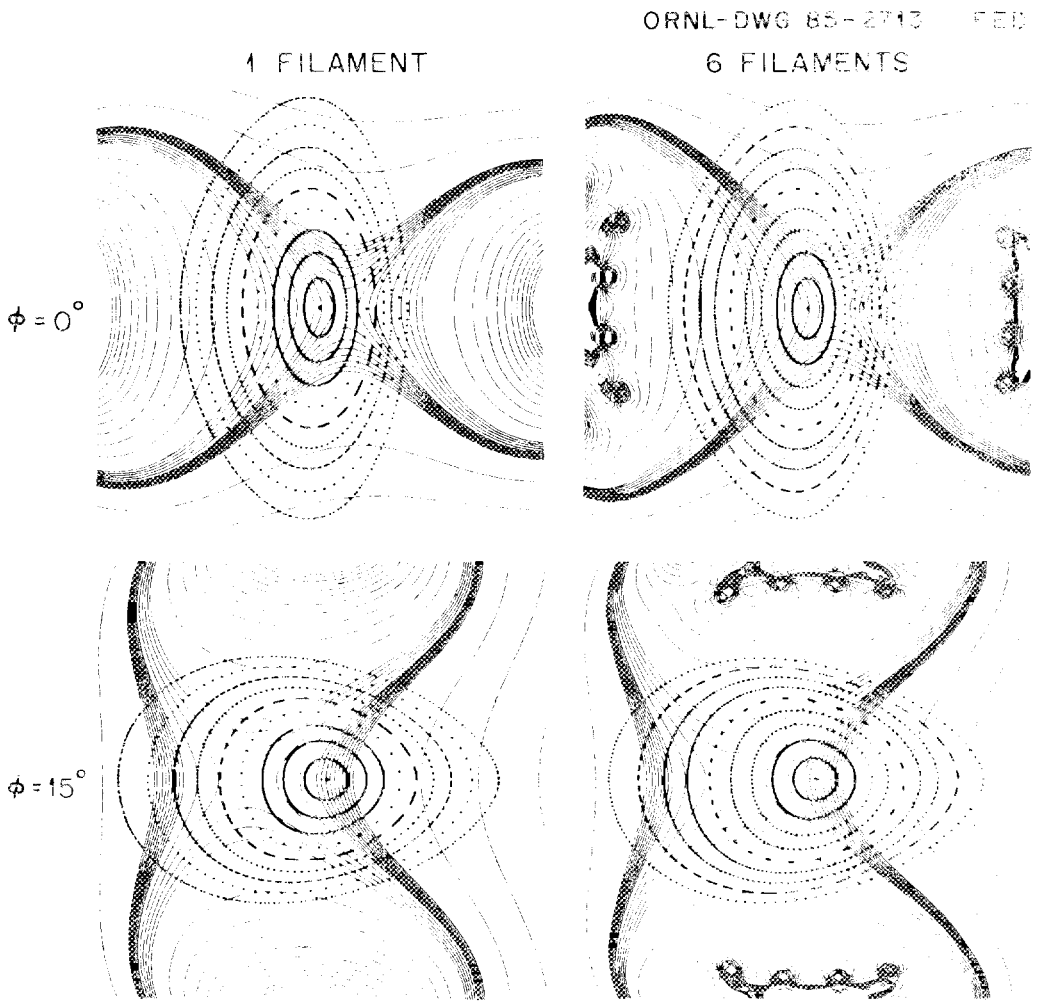

Fig. 15. Flux surfaces and |B| contours for the standard ATF configuration, modeled with one and six filaments. The |B| contours are separated by 0.05 T and range from 1 T between the coils to 2.8 T under the coils. The central (saddle-point) |B| = 2.0 T.

The PF coil system shown in Fig. 12 permits wide variations from the parameters of the standard configuration just described. The flexibility to modify and control the magnetic configuration parameters derives from the three degrees of freedom inherent in the PF coil system: (1) the poloidal flux, which controls the net plasma current (normally zero); (2) the dipole moment, which permits shifting the magnetic axis inward or outward and varying the vacuum magnetic well depth; and (3) the quadrupole moment, which permits poloidal shaping of the magnetic surfaces and changing the central rotational transform. Changes in these quantities can be expressed [35] as linear combinations of the inner, outer, and mid-VF coil currents, so the three VF coil sets allow independent control of these quantities.

Figure 16 shows the $\phi = 0^{\circ}$ magnetic flux surfaces for a range of plasma shifts and plasma shaping. Table VII gives the corresponding values of the VF coil currents. The central case in the figure is the standard ATF configuration (nominal current settings). A wide range of plasma shapes is possible, from basically triangular to elliptical to configurations with a bifurcated magnetic axis [$\iota(0) = 0$]. Shifting the axis inward in major radius ($\Delta_v < 0$) produces a destabilizing magnetic hill; the nominal axis position ($R = 2.1$ m) or shifting the axis outward ($\Delta_v > 0$) produces a stabilizing magnetic well.

Some possible variations in the magnetic configuration parameters obtained by changing the mid-VF coil current are shown in Fig. 17(a) for the unshifted ($R_0 = 2.1$ m) configurations in the central column of Fig. 16. Figure 17(b) shows the changes in these parameters obtained by shifting the magnetic axis for the unshaped ($I_{MID} = 0$) configurations in the central row of Fig. 16. Fairly large variations are possible in central transform (from 0 to 0.5), edge transform (from 0.8 to 1.24), and magnetic well/hill (from 5.2% well to ~20% hill), but the average plasma radius is approximately constant (28.5 cm to 34.7 cm) during these parameter variations. Figure 18 shows the radial profiles of ι and $V'(\bar{r})/V'(0)$ for the extremes of the I_{MID}/I_h and Δ_v ranges in Fig. 17.

These magnetic configurations have essentially a circular magnetic axis. An important variant of the stellarator configuration, one with

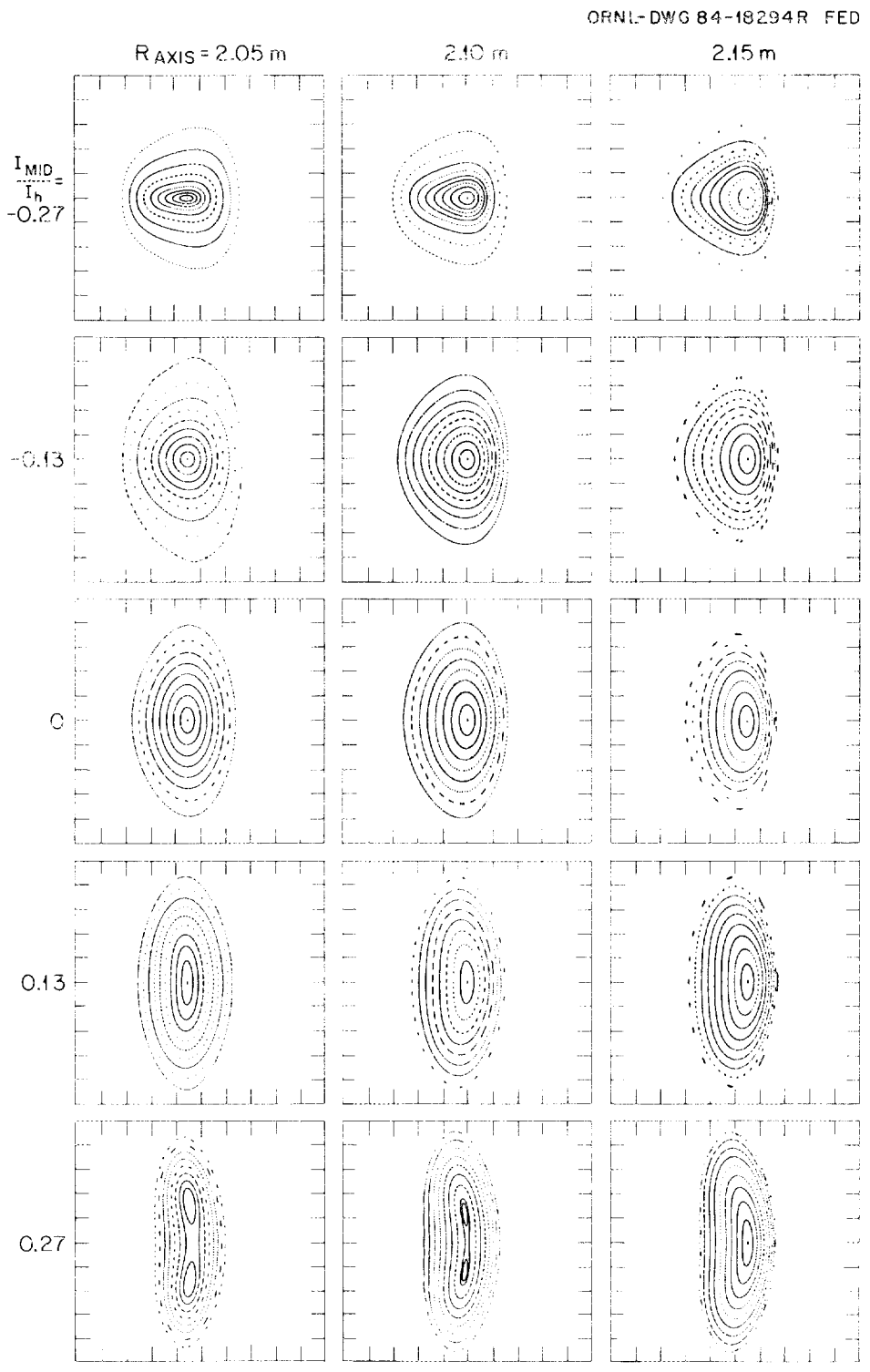

Fig. 16. Vacuum magnetic flux surfaces at $\phi = 0^{o}$ for different magnetic axis radii R_{axis} and mid-VF coil current I_{MID} (normalized to the HF coil current, I_{MID}/I_{h}).

TABLE VII

Coil Currents for Configurations in Fig. 16

I_{MID}/I_h	R_0 (m)	I_{inner}/I_h	I_{outer}/I_h	$\iota(0)$
-0.27	2.05	0.329	-0.432	0.173
	2.1		-0.425	0.311
	2.15		-0.406	0.533
-0.13	2.05	0.236	-0.477	0.274
	2.1		-0.461	0.352
	2.15		-0.434	0.533
0	2.05	0.150	-0.520	0.266
	2.1		-0.494	0.336
	2.15		-0.460	0.504
+0.13	2.05	0.064	-0.561	0.161
	2.1		-0.528	0.260
	2.15		-0.486	0.439
+0.27	2.05	-0.029	-0.591	0
	2.1		-0.566	0
	2.15		-0.514	0.316

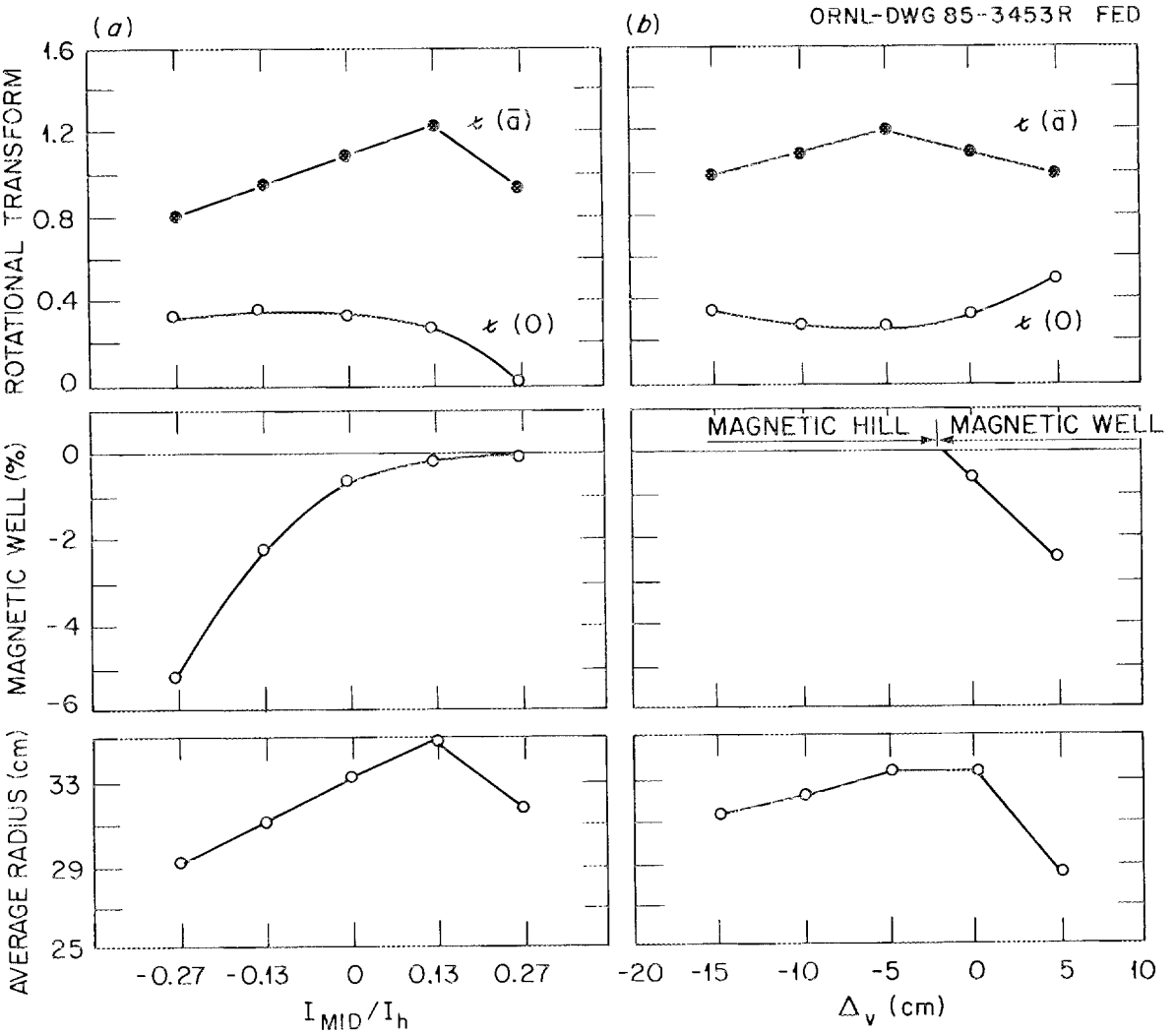

Fig. 17. Variation of vacuum configuration properties vs (a) I_{MID}/I_h for centered configurations and (b) axis shift (Δ_v) for $I_{MID} = 0$.

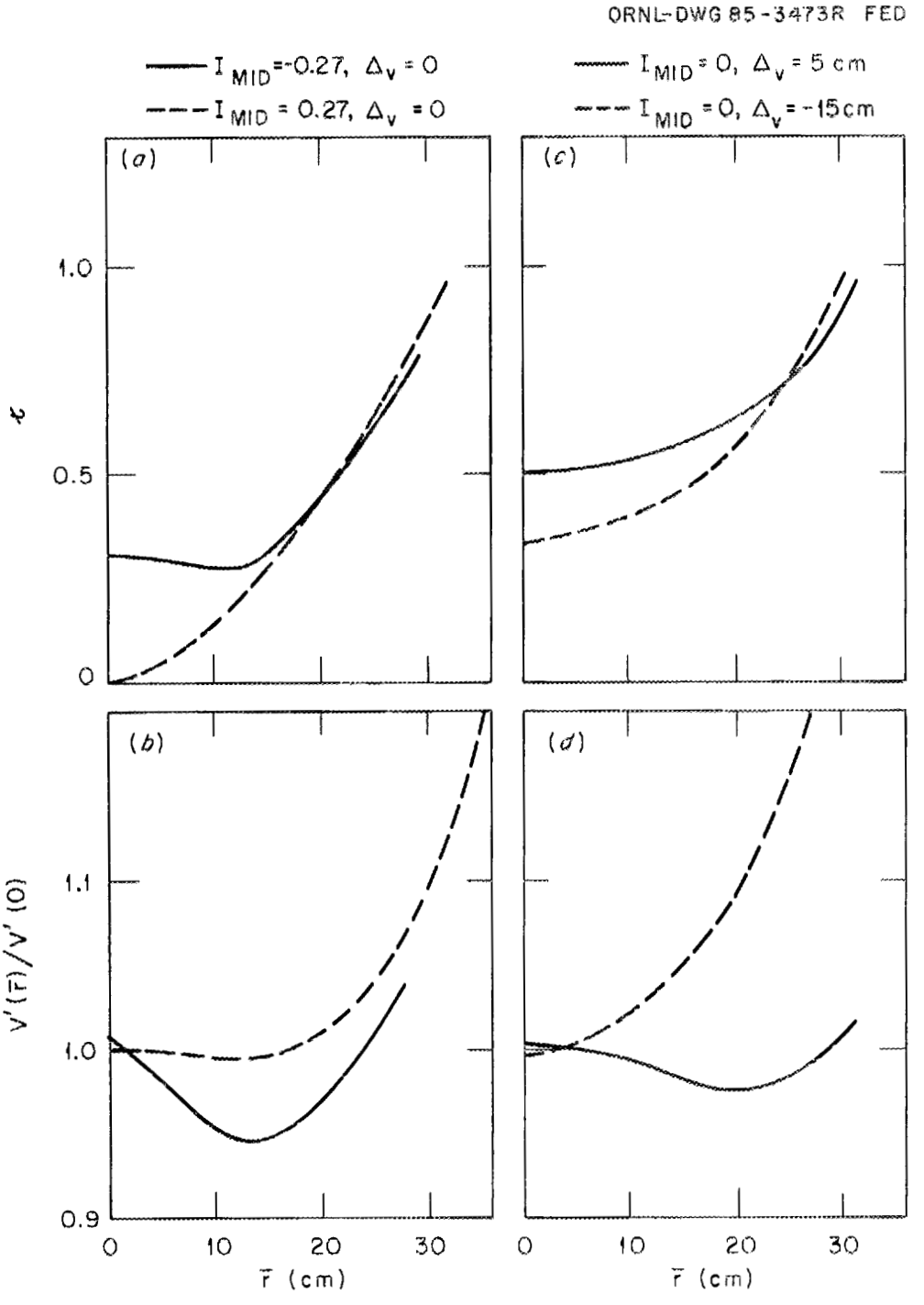

Fig. 18. Radial profiles of ι and $V'(\bar{r})/V'(0)$ for configurations at the extremes of the I_{MID}/I_h and Δ_v variations in Fig. 17.

a helical magnetic axis, can also be obtained with the ATF coil set by using different currents in the two HF windings. Figure 19 shows an example obtained with one HF winding having 0.16 times the current in the other (both in the same direction). The helical nature of the magnetic axis can be seen in Fig. 19(a) and in Fig. 19(c), which shows the poloidal rotation of the plasma cross section around the HF winding axis. Figure 19(d) shows the vacuum flux surfaces in the $\phi = 0^{\circ}$ and $\phi = 30^{\circ}$ planes in more detail. The rotational transform [Fig. 19(b)] varies from $\iota(0) = 0.62$ to $\iota(\bar{a}) = 0.93$.

In addition to having a helical axis, this configuration is interesting because of its lower shear and lack of a primary ($n = 1$) resonance in the plasma. Since the helical-axis plasma follows the HF winding with the higher current, it tends to be closer to the vacuum wall and thus have a smaller average radius ($\bar{a} = 15$–20 cm). Other helical-axis configurations can be obtained by varying the ratios of the two HF winding currents and of the VF coil currents. Although ATF has not been optimized for helical-axis configurations, it will nevertheless provide useful insight into the MHD properties of these configurations [36].

III.B. Finite-Beta Effects

As discussed in Sec. II.B, ATF was optimized for high-beta plasma operation and provided with the necessary flexibility to study the physics of high-beta toroidal plasmas. The optimization was done so that ATF is limited in beta only by equilibrium and not by stability (stable access to the second stability regime). Equilibrium calculations have shown the existence of equilibria at least up to $\langle\beta\rangle = 8\%$ (Fig. 20). Numerous calculations [33–40] have been performed with different 3-D equilibrium codes and for a broad range of pressure profiles, and they show consistent results. Fixed and free boundary ideal MHD stability calculations for low-n modes ($n < 3$) show that all equilibria for the standard ATF configuration (vacuum magnetic axis position at $R = 2.1$ m) are stable [33,38]. These calculations covered a wide range of parameters and assumptions. The volume-average beta $\langle\beta\rangle$ ranged from 0 to 7.5%. The pressure profiles assumed were $p = \psi_p^x$,

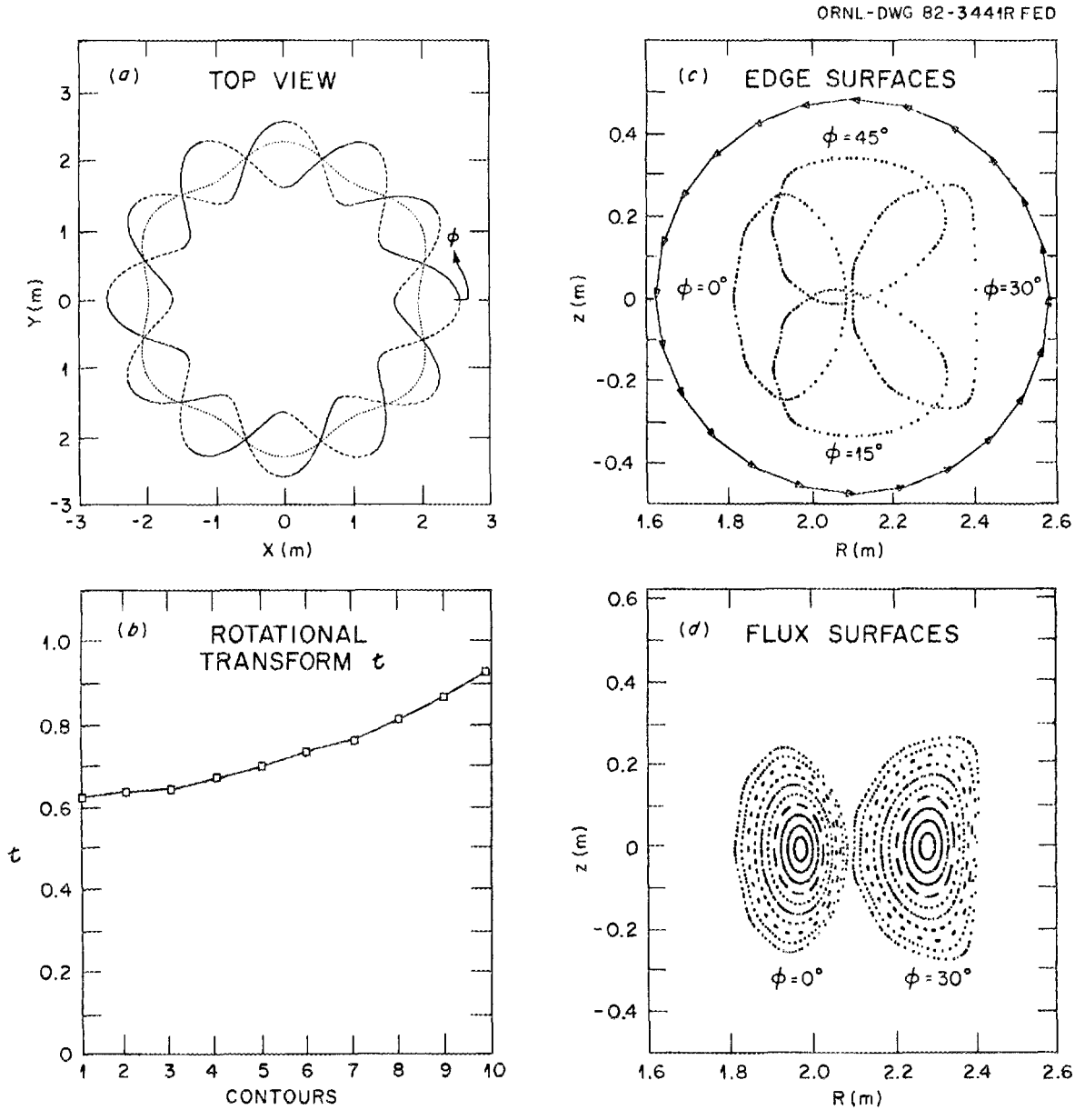

Fig. 19. Helical-axis configuration with six field periods, produced by unequal currents in the HF coil windings ($I_1/I_2 = 0.16$). (a) Top view of ATF showing the helical magnetic axis (dotted curve) and the two helical windings (solid on top, dashed underneath). (b) Rotational transform vs contour number (1 = central, 10 = edge) of vacuum flux surfaces in (d). (c) Side view of the outer flux surfaces at $\phi = 0^{\circ}$, 15°, 30°, and 45° and the circular projection of the helical windings. (d) Internal structure of the vacuum magnetic surfaces at $\phi = 0^{\circ}$ and $\phi = 30^{\circ}$ shown in (c).

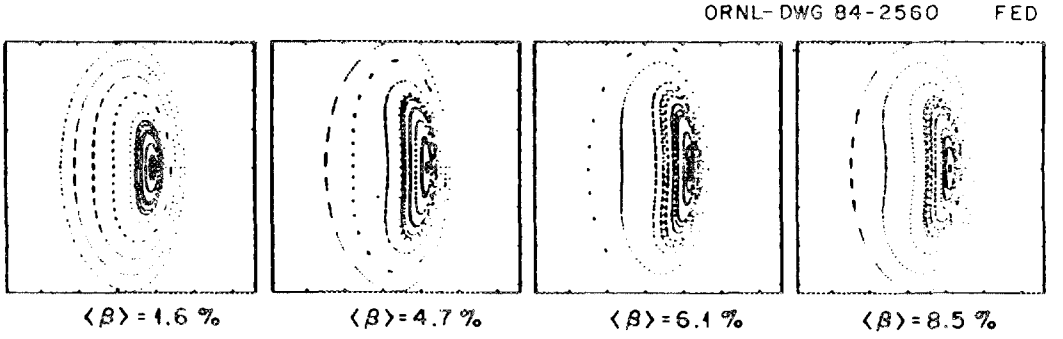

Fig. 20. Sequence of MHD equilibria from the 3-D NEAR code for the standard ATF configuration.

where Ψ_p is the poloidal flux, normalized to 1 at $r = \bar{a}$, and the exponent x ranged from 1.3 to 4. Finally, the equilibria considered assumed either flux conservation or zero net current on each flux surface. When the shaping coils were used to maintain the transform close to its vacuum profile, the plasma also remained stable to Mercier (high-n, radially localized) modes [35].

The stabilization of the low-n modes in ATF is mainly due to the deepening of the magnetic well with increasing beta and to the exclusion of the $\iota = 1$ surface from the plasma. The deepening of the magnetic well is sufficient to stabilize the modes resonant at the $\iota = 1/2$ surface, the most dangerous modes for this configuration. The increase in well depth with beta is produced by the outward shift of the magnetic axis (evident in Fig. 20 and plotted in Fig. 21). The well depth for the standard ATF configuration increases from 0.7% in the vacuum to about 15% at a peak beta value of 10%. The magnetic well also broadens radially with increasing beta and extends to $\iota > 1/2$ (Fig. 22). This increase in well depth with beta is such that the plasma stability properties improve with increasing beta.

The beta limits and their dependence on the magnetic configuration properties can be tested in ATF at relatively low beta values. This can be done by shifting the magnetic surfaces inward, creating a magnetic hill in the plasma. The effect on the plasma stability is illustrated in Fig. 23. For a 5-cm inward shift Δ_v of the vacuum magnetic axis, the plasma is stable for $\beta_0 < 1.5\%$ (first stability region), unstable for $1.5\% < \beta_0 < 8\%$, and stable again due to the beta-self-stabilizing effect for $\beta_0 > 8\%$ (second stability region). This corresponds to a relatively low beta range, $\langle\beta\rangle < 3\%$, and can be tested experimentally. For the standard ATF position ($\Delta_v = 0$) or for an outward shift ($\Delta_v > 0$), the plasma is stable over the entire beta range shown in the figure. For these cases the first and second stability regions have merged, a situation commonly known as having stable access to the second stability region.

Another feature of the flexibility built into ATF may be seen in Fig. 24, which shows the variation of the magnetic axis transform $\iota(0)$ with beta and with the quadrupole moment of the VF coil system for

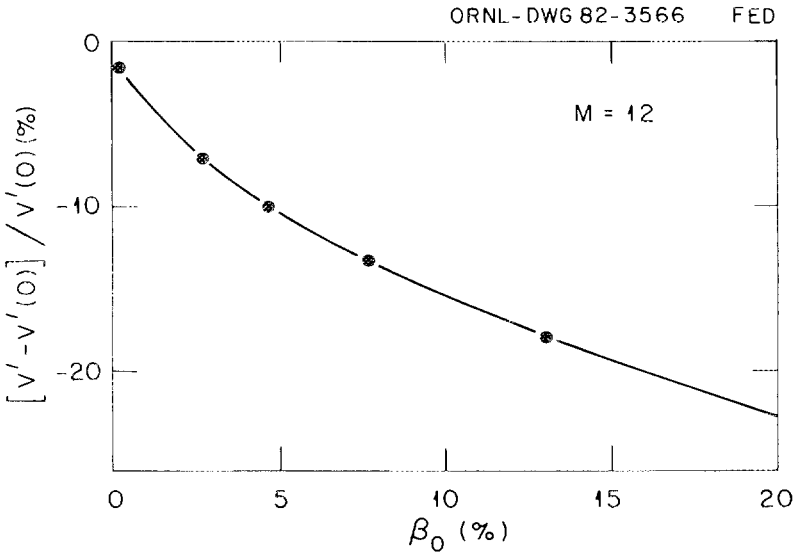

Fig. 21. Deepening of the magnetic well with beta due to the increasing outward (Shafranov) shift of the magnetic axis.

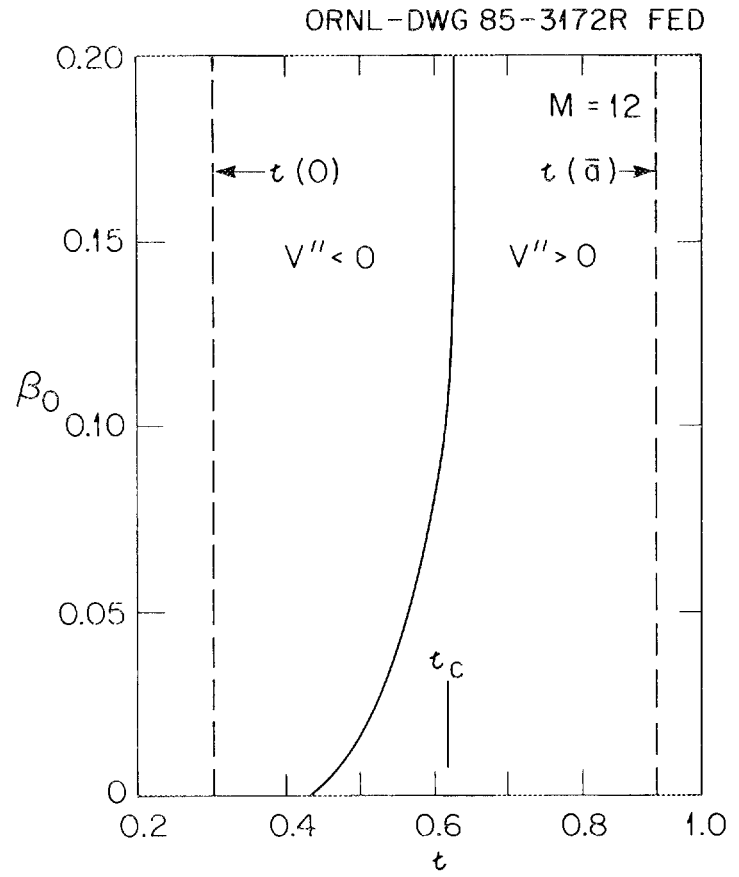

Fig. 22. Dependence of the critical surface (V" = 0) location on beta for a flux-conserving M = 12 torsatron, indicating an increase in well size as beta increases (second stability region).

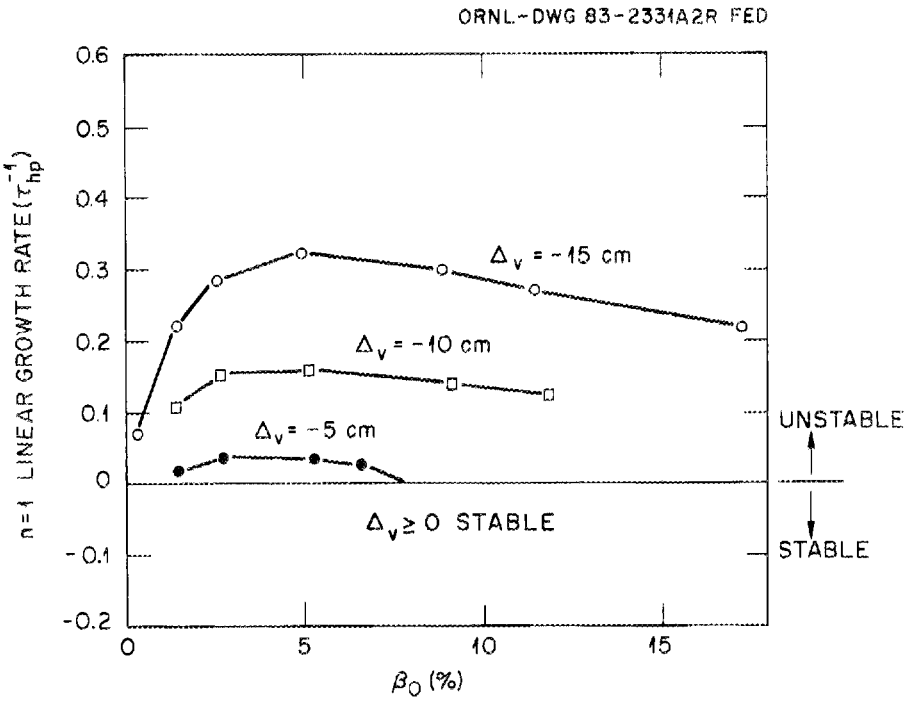

Fig. 23. Linear growth rate of n = 1 instabilities induced by shifting the plasma inward in major radius, thereby creating a magnetic hill.

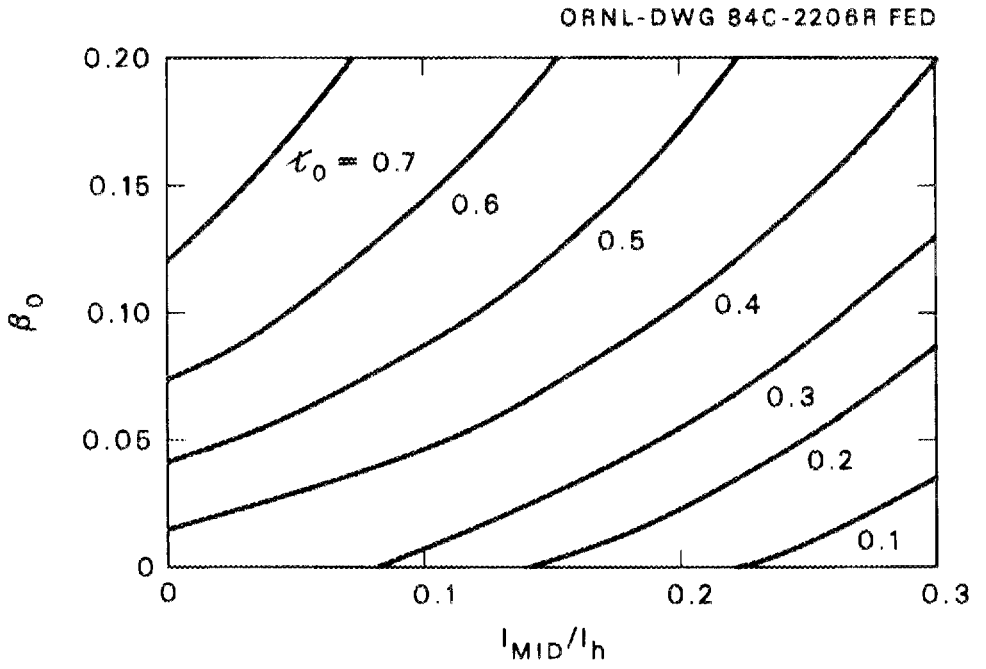

Fig. 24. Variation of $\iota(0)$ with beta and I_{MID}/I_h for zero-net-current equilibria. Paths of constant $\iota(0)$ can be followed to high beta by increasing I_{MID} as beta increases.

zero-current equilibria. Examples of these equilibria are shown in Fig. 25 for different beta values. Increasing the quadrupole moment decreases the transform but increases the beaniness of the plasma. By combining beta and shaping, the plasma can attain high beta while maintaining a transform very close to the optimal vacuum transform [35]. This path corresponds to the diagonal from top left to bottom right in Fig. 25. This way of achieving high beta improves the equilibrium and stability of the plasma. The equilibrium improvement is due to a reduction of the variation of $\int d\ell/B$ in a field period, which causes a reduction of the magnetic axis shift with beta and the concomitant equilibrium improvement. Although the shift is reduced, there is no reduction of the magnetic well because the shaping deepens the well. The overall effect on stability is an improvement for the Mercier modes, which are now stabilized even for very broad pressure profiles.

III.C. Confinement and Transport

Energetic orbit confinement and transport are important factors in selection of an optimum stellarator magnetic configuration. The relatively large helical field ripple in stellarators can lead to large losses of ripple-trapped particles, which are sensitive to the details of the magnetic configuration [41]. Ripple-trapped particles are not well confined because their localization in a helical ripple well emphasizes the outward $\vec{B} \times \nabla B$ drift and reduces the compensating poloidal rotation due to $+$. These particles should drift rapidly outward and be lost to the vacuum wall in ATF.

However, guiding center orbit calculations assuming no electric field and using accurate representations of the ATF magnetic geometry (multifilament coil model) and the ATF vacuum vessel show that although trapped-particle orbits do go outside the last "closed" magnetic surface (taken to be the plasma boundary), these orbits return to the plasma before hitting the wall [42]. This is illustrated in Figs. 2 and 3 for collisionless 1-keV H^+ orbits launched randomly in θ, ϕ, and $v_{\parallel}/v$ at $r/\bar{a} = 0.95$ for $B = 1$ T. The last closed flux surface in these figures is at the outer edge of the ellipse formed by the densest concentration of orbit punctures. Similar

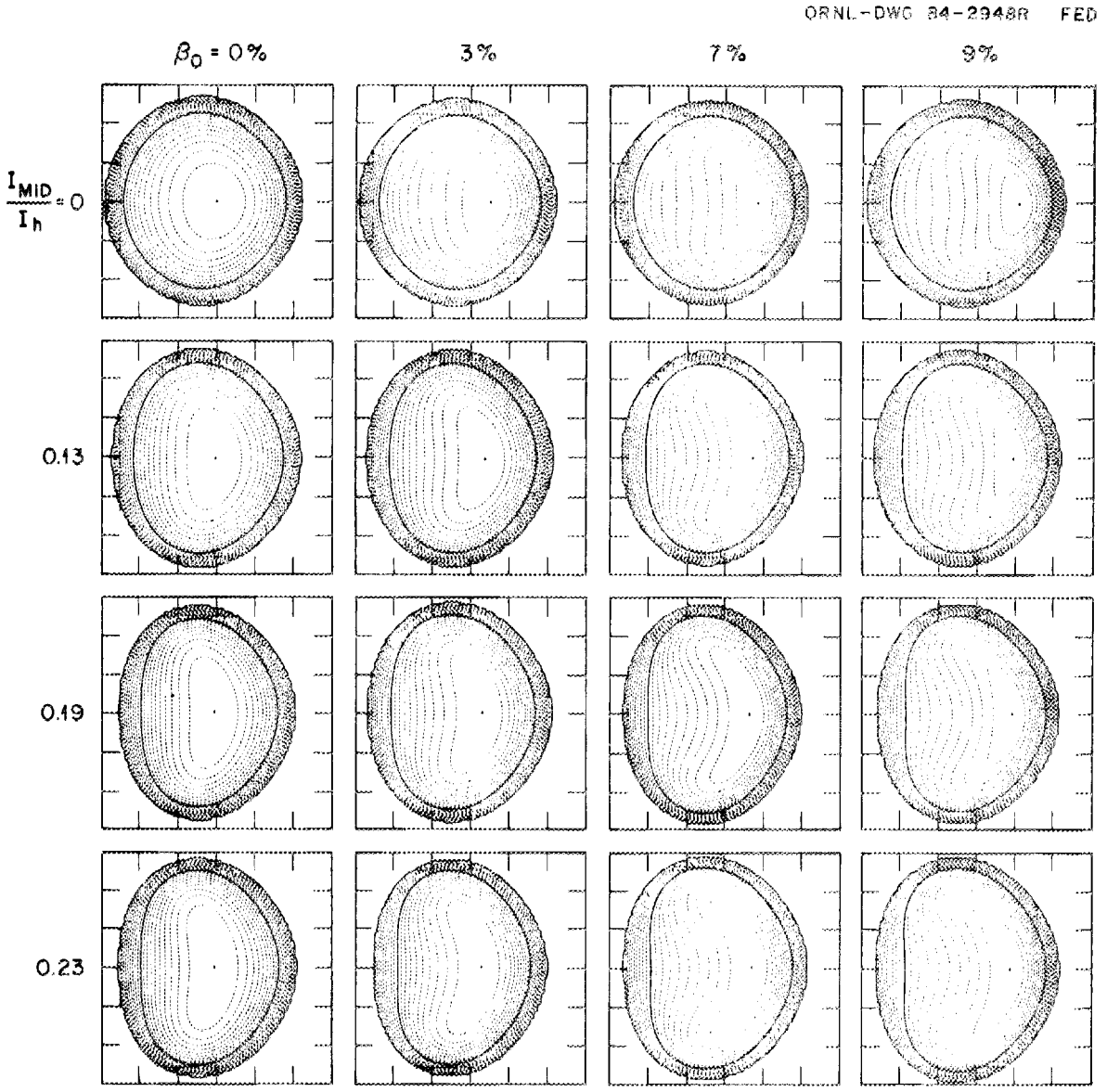

Fig. 25. 2-D averaged, zero-net-current magnetic surfaces calculated from a free boundary MHD equilibrium code for different values of central beta (β_0) and the normalized value of the mid-VF coil current, I_{MID}/I_h. The diagonal from top left to bottom right gives an approximate flux-conserved [$\pi(\psi)$ approximately fixed] sequence with constant $\pi(0)$. Increasing I_{MID} elongates the plasma and produces more bean-shaped interior flux surfaces in combination with the axis shift.

results are obtained for low-energy (10-eV) ions launched at $r/\bar{a} = 0.95$ and for high-energy (20-keV) ions launched at $r/a = 0.25$. Thus, there is effectively no collisionless orbit loss region in ATF, even in the absence of electric fields.

The shapes of the HF coil cross section (specifically, the chamfered corners) and of the vacuum vessel were chosen to take advantage of this situation by maximizing the distance between the last closed flux surface and the vacuum vessel wall, as discussed in Sec. IV.C. Introduction of H^+-H^0 charge-exchange collisions leads to a fairly uniform loss of energetic particles to the wall, with surfaces closer to the plasma (under the HF coils) receiving a somewhat higher share.

In addition, the poloidal $\vec{E} \times \vec{B}$ orbit rotation due to ambipolar radial electric fields of moderate strength (potential $\Phi \sim T$) has a much larger effect on confinement improvement than do differences in magnetic configuration properties. A sufficiently large poloidal $\vec{E} \times \vec{B}$ velocity due to either sign of the radial electric field can overcome the radial drift of helically trapped particles and effectively close the loss region that would otherwise lead to a large $1/\nu$ transport at low collisionality [11,12,43-45]. The large reduction in collisionless orbit losses for $\Phi \gtrsim E$, the particle energy, is illustrated in Fig. 26. The changes in the magnetic configuration that result from finite beta produce effects on the orbit losses that are much smaller by comparison.

The radial electric field also leads to a reduction in diffusive losses, as shown in Fig. 27. For $\Phi \gtrsim T$, the ripple-trapped particle contribution to the ion heat diffusivity χ_i calculated by Shaing and Houlberg [11] is reduced to values comparable to that for the axisymmetric neoclassical χ_i calculated by Hinton and Hazeltine [46]. Monte Carlo calculations for ATF [10] also show large reductions in transport for $\Phi \gtrsim T$. Similar confinement improvement is seen in other Monte Carlo calculations [47,48] and in Fokker-Planck calculations [49] of stellarator transport, and it is inferred from measurements on Wendelstein VII-A and related calculations [50].

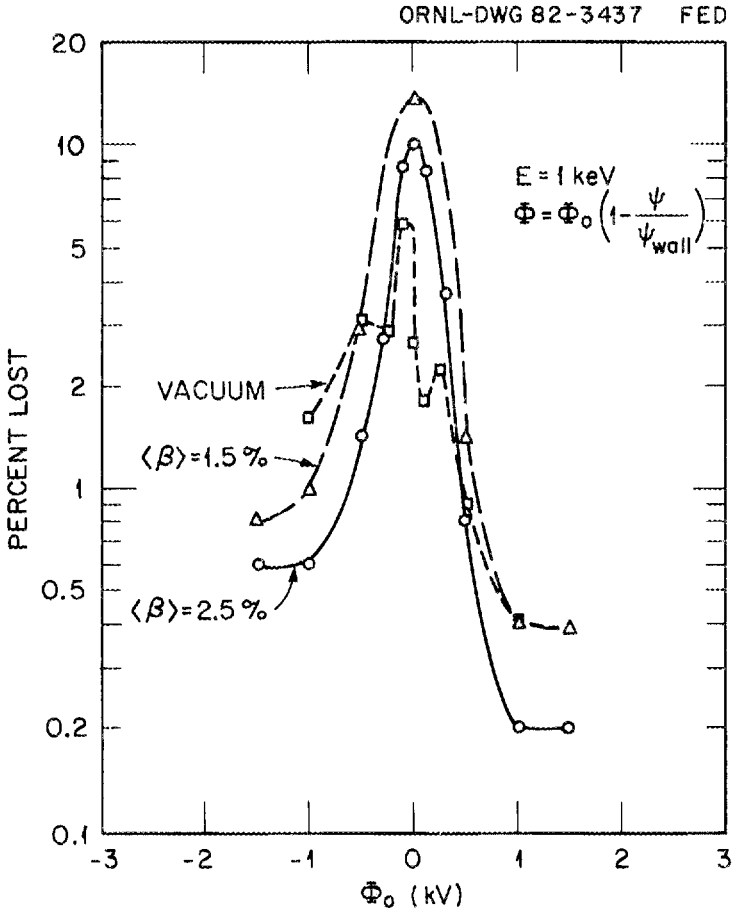

Fig. 26. The density-weighted loss fraction of 1-keV H^+ at B = 1.8 T for the vacuum configuration and $\langle\beta\rangle$ = 1.5% and 2.5% as a function of Φ_0. Here n and Φ have the form $1 - \psi/\psi_{wall}$ (approximately parabolic profiles).

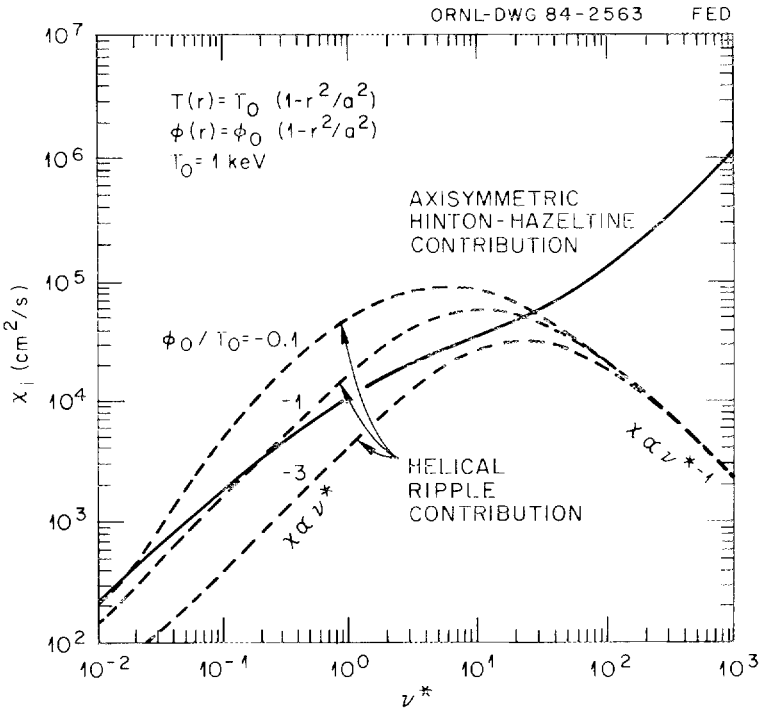

Fig. 27. Ion heat diffusivity χ_i vs collisionality ν_i^*. Moderate radial electric fields reduce the ripple-trapped contribution to χ_i and move the transition to favorable transport scaling ($\chi_i \propto \nu^*$ instead of $\chi_i \propto 1/\nu^*$) to higher collisionality.

III.D. Performance Projections

The ATF mission requires the attainment of high beta and low collisionality and the reduction of driven plasma currents. Rough estimates for these quantities can be obtained from simple expressions, although more extensive, profile-dependent, 1-D transport code calculations are required for more accurate estimates.

Energy confinement time $\tau_E \sim \bar{a}^2/4\chi$ and volume-average beta $\langle\beta\rangle$ are related through the plasma stored energy W by $W = P_{abs}\tau_E = (3B^2\langle\beta\rangle V)/4\mu_0$, where P_{abs} is the absorbed heating power and V is the plasma volume. Scaling from Heliotron-E data [23] ($\bar{a}$ = 0.2 m, B = 0.94 T, P_{abs} = 1.2 MW, $\langle\beta\rangle$ = 2%, τ_E^{net} = 10-20 ms) gives τ_E = 23-45 ms and $\langle\beta\rangle$ = 6% (for P_{abs} = 3.6 MW).

The plasma parameter range expected for ATF was calculated using the WHIST transport code, modified for stellarators [11] and benchmarked against Heliotron-E data. The transport calculations use the full electric-field-dependent, helical ripple transport model of Shaing and Houlberg; the Hinton-Hazeltine axisymmetric (tokamak) neoclassical contribution (times 2 for χ_i and times 20 for χ_e and D); and an empirical anomalous transport term peaked at the edge for χ_e and D based on Poloidal Divertor Experiment (PDX) modeling {D, χ_e = $1000[1 + 4(r/a)^2]$ cm^2/s}. The ambipolarity condition $\Gamma_i = \Gamma_e$ is used to determine the radial electric field self-consistently.

The results of these calculations for 50-kV tangential H^0 injection into an H^+ plasma are shown in Figs. 28 and 29. At a volume-average density $\langle n\rangle = 1.9 \times 10^{13}$ cm^{-3}, a 4-MW H^0 beam would give $\langle\beta\rangle$ = 6% and $T_i(0)$ = 4 keV at B = 1 T (Fig. 28), and a 3-MW H^0 beam would give $\langle\beta\rangle$ = 1.3% and $T_i(0)$ = 5 keV at B = 2 T (Fig. 29). Results for a D^+ plasma case would be somewhat higher. Operation at 1 T is better for high-beta studies because confinement does not scale as rapidly as B^2, and operation at 2 T is better for low-collisionality studies because T_i is higher at the higher field.

The sensitivity of the calculated ATF performance to the self-consistent radial electric field is illustrated in Table VIII. These time-dependent WHIST calculations assume 3-MW tangential H^0 NBI into a

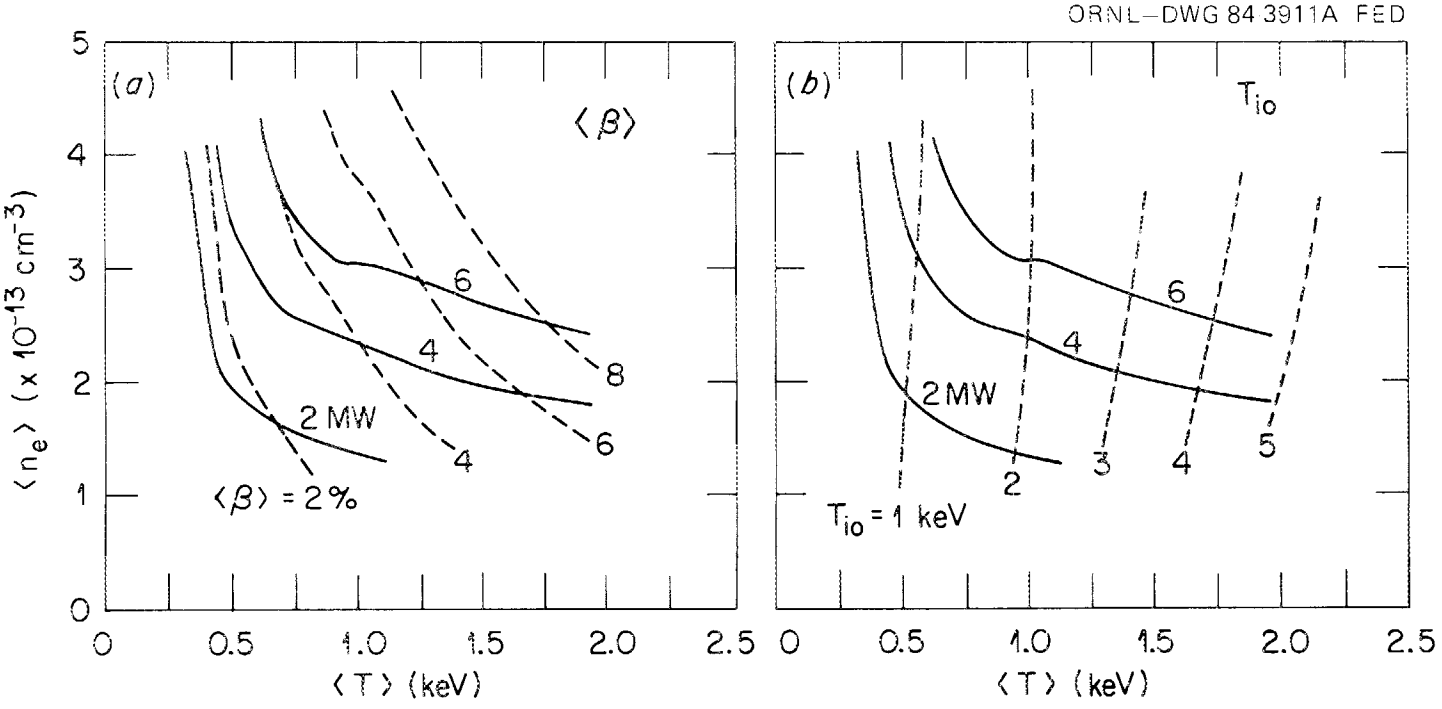

Fig. 28. WHIST transport code calculations for 50-kV H^0 tangential NBI into H^+ plasma at B = 1 T. The axes are the volume-averaged density $\langle n_e \rangle = N/V$, and the combined particle-averaged temperature $\langle T \rangle = W/N$. The solid curves are contours of constant injection power (in megawatts); the dashed curves give contours of (a) constant $\langle \beta \rangle$ in percent and (b) $T_i(0)$ in keV.

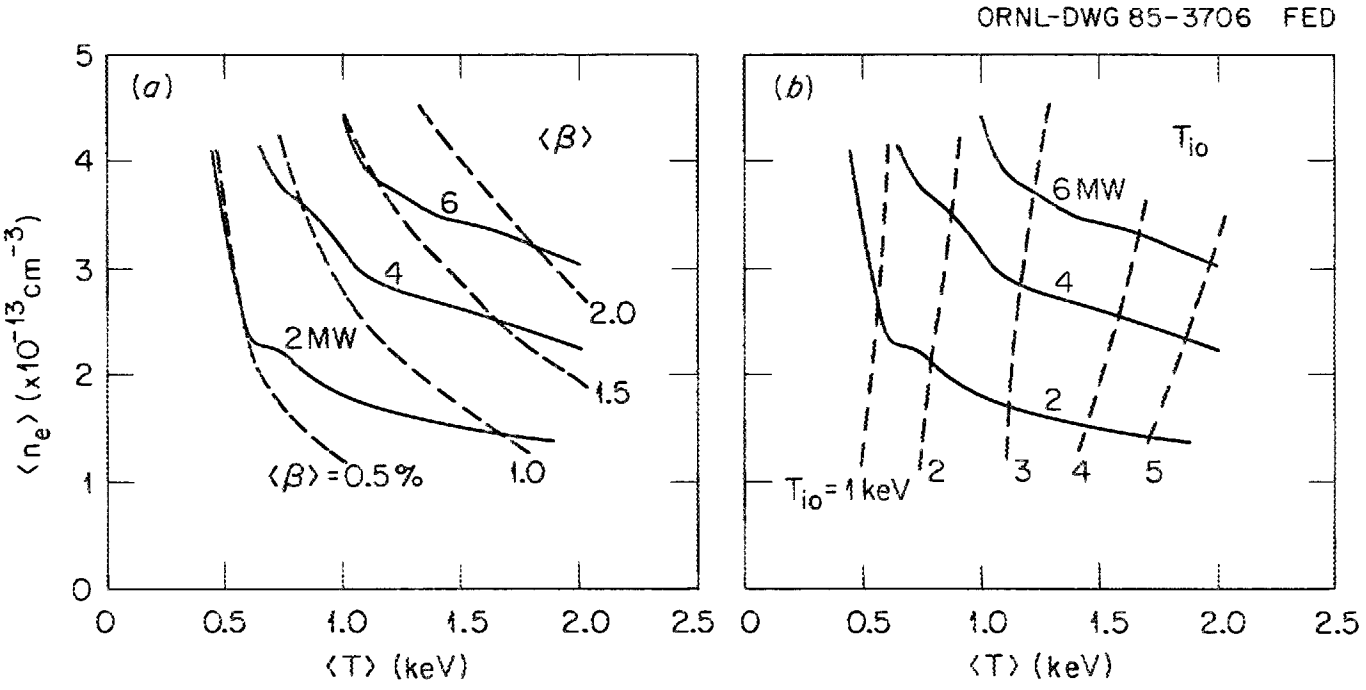

Fig. 29. WHIST transport code calculations for 50-kV H^0 tangential NBI into H^+ plasma at B = 2 T.

TABLE VIII

Time-Dependent WHIST Transport Calculations

Initial $\langle n_e \rangle$, cm^{-3}	1.1×10^{13}	1.1×10^{13}	4.1×10^{13}	4.1×10^{13}
B, T	1	2	1	2
$n_e(0)$, cm^{-3}	5.36×10^{13}	6.00×10^{13}	5.75×10^{13}	5.69×10^{13}
$\langle n_e \rangle$, cm^{-3}	1.82×10^{13}	1.95×10^{13}	4.71×10^{13}	4.74×10^{13}
$\bar{n}_e$, cm^{-3} (a)	2.55×10^{13}	3.02×10^{13}	5.07×10^{13}	5.05×10^{13}
Φ, kV	8.35	12.3	-1.22	-1.69
$T_i(0)$, keV	2.53	9.66	0.53	0.96
$\langle T_i \rangle$, keV	1.63	5.24	0.38	0.58
$T_e(0)$, keV	2.75	4.00	0.60	1.05
$\langle T_e \rangle$, keV	1.86	2.76	0.42	0.59
$\langle \beta \rangle$, %	5.08	2.22	1.89	0.71
$\langle \beta_{thermal} \rangle$, %	1.96	1.26	1.49	0.55

(a) line-average density

D^+ plasma. For low initial density, the density rises due to beam fueling, and a large positive potential (outward radial electric field) develops, reaching a value $\Phi/T \sim 3$. The density profile is peaked [$n_e(0)/\bar{n}_e \sim 2$], and high temperatures and high beta values with a significant fast-ion component are obtained. For higher initial density, the density rises less [$n_e(0)$ approximately the same], and a negative potential (inward radial electric field) develops, reaching a value $\Phi/T \sim -1$. The density profile is broad [$\bar{n}_e$ close to $n_e(0)$], and the plasma temperatures and beta are considerably lower.

The calculated ATF performance is only suggestive, since the radial electric field and its effect on transport are unknown, as are anomalies in confinement, details of the edge transport, and impurity radiation losses. In fact, this determination is part of the ATF base program, and a heavy-ion beam probe will be installed to map the potential over two-thirds of the plasma cross section [51].

The WHIST transport model may be too pessimistic, given the experimental determinations of χ_e and χ_i from Heliotron-E and Wendelstein VII-A. These experiments show that χ_e is near neoclassical values in the plasma core, although it is anomalously high in the edge region ($\chi_e \sim 1/nT^{2/3}$ in Wendelstein VII-A), and that χ_i is near neoclassical values. Recent experiments on Wendelstein VII-A [50] suggest that χ_i may even be much less than the Hinton-Hazeltine axisymmetric neoclassical values due to large radial electric fields (~6-kV potential) produced by fast-ion losses.

Plasma currents driven by different mechanisms related to equilibrium (Shafranov shift, Pfirsch-Schlüter current) and transport (bootstrap current, beam-driven current) may also affect the ATF performance. These currents can range up to ~40 kA, sufficient to increase $\iota(0)$ to ~1, and must be compensated by changes in the VF coil currents or by using balanced (co plus counter) NBI. Large net plasma currents can also lead to increased transport in stellarators [17].

The net equilibrium current varies approximately linearly with central beta (1.86 kA for each percent beta at B = 1 T) up to $\beta(0) \approx 20\%$ and as $\beta(0)^{1/3}$ at higher beta. The compensating current in the

mid-VF coils to maintain $\iota(0)$ constant as beta increases is shown in Fig. 24. The Pfirsch-Schlüter current is zero integrated over a flux surface, with a maximum current density $j_{PS} = -(r/R)(c/B_p)(dp/dr) \sim 5\ kA/m^2$ for typical ATF parameters. The bootstrap current density, $j_b = 4.3(r/R)^{1/2}(c/B_p)(dp/dr)(\ell\iota/m)$, integrates to ~100 A for typical ATF parameters and can also be neglected. However, neutral-beam-driven currents can be large ($\lesssim$40 kA) [52], depending on beam momentum, n_e, T_e, toroidal damping due to ripple, etc., and must be compensated.

III.E. Plasma Heating Physics

Multimegawatt plasma heating is required in currentless plasma operation for the ATF to fulfill its mission. This heating will be provided by ECH, NBI, and ICH. The ATF does not have an OH transformer because a plasma current is not required for good confinement or heating in a stellarator and would lead to increased transport and additional MHD instabilities. A total of 12 V·s is available in the HF and VF coil sets, so a 4.8% change in the HF coil currents is sufficient to drive a plasma current of 40 kA at 1 T, which then decays with a time constant of approximately 0.3 s. However, this level of plasma current would produce relatively little plasma heating (<0.1 MW) and would increase the rotational transform to 1 in the plasma interior, producing an unsatisfactory magnetic configuration. Compensation for the increased interior transform would require VF coil currents similar to those in the bottom rows of Table VII to lower the central transform or addition of TF coils to lower the overall transform level.

Electron Cyclotron Heating. ECH will permit currentless startup of the ATF plasma by providing a moderate-density ($n_e \sim 10^{13}\ cm^{-3}$), moderate-temperature ($T_e \leq 1$ keV), current-free target plasma for NBI or ICH. Steady-state ECH, at sufficient power, would also provide an independent control on electron temperature (and electric field) for confinement studies of steady-state plasmas. Initially 0.2 MW of ECH will be used, with an upgrade to 0.4 MW in 1988.

The best match for the ATF needs is ECH at 53.2 GHz. The cutoff density is high (3.5×10^{13} cm^{-3} for O-mode), and this frequency can be used for pulsed operation in O-mode at fundamental resonance (1.9 T) and for steady-state operation in X-mode at second harmonic resonance (0.95 T) and possibly at third harmonic resonance (0.63 T). The high-field fundamental heating is most useful for the low-collisionality transport studies, and the low-field second and third harmonic heating is most useful for the high-beta studies. Second harmonic ECH is efficient for currentless plasma formation and heating to T_e = 1-2 keV on Heliotron-E [53] and Wendelstein VII-A [54]. Third harmonic ECH is not useful for plasma formation or heating of cold plasma but may be effective for plasma heating if 18-GHz ECH ($\simeq$ 53.2 GHz/3) is used first to preionize and preheat the plasma.

Neutral Beam Injection. The main plasma heating power for ATF will be provided by three neutral beam lines, each delivering up to 1.5 MW at 40 to 50 kV for 0.3-s pulses [55]. The large outside ports provide tangential injection access for a 22-cm-diam beam. Tangential NBI has been chosen because the 2.5-m beam path length in the plasma allows low-density operation and because the small angle to the field ($|v_{\parallel}/v| \geq 0.9$) ensures that the energetic injected ions are far from the orbit loss region at small $v_{\parallel}/v$. Two injectors will be aimed in the coinjection direction (parallel to the toroidal component of the HF coil current, or opposite to the toroidal field for ATF's left-handed helical coils) and one in the opposite (counterinjection) direction. This arrangement allows control of beam-induced toroidal momentum and plasma current. Near-perpendicular injection would limit operation to high plasma density since the beam path length would be $\leq$0.75 m.

Neutral beam heating has several advantages: it is effective over a wide range of density and magnetic field, the energy deposition profile can be calculated, it can provide momentum input for impurity control, and it does not introduce impurities or primarily perpendicularly heated ions in the plasma. Disadvantages are the introduction of a large hydrogen source rate in the plasma (and consequent need to control the plasma density) and a toroidally driven current (which must be compensated to avoid modification of the rotational transform profile).

Ion Cyclotron Heating. ICH power is available in two frequency ranges for use on ATF: (1) 0.4 MW at 5-30 MHz cw and (2) 1.5 MW at 40-80 MHz, nominally up to 30-s pulses. Unless OH startup (and subsequent plasma current rampdown) or some ICH startup is used, the ICH frequencies for ATF are tied to the 53.2-GHz ECH frequency through low multiples of the ion-to-electron mass ratio. However, this still allows a large number of heating frequencies through combinations of H, D, and He^3 operation; fundamental and second harmonic heating; and operation at B = 1.9 T, 0.95 T, and possibly 0.63 T (with additional 18-GHz ECH).

A variety of ICH mechanisms can be used for bulk ion heating. Fast-wave heating (either minority species or second harmonic) can be used with H^+ or D^+ plasmas at B = 0.95 T or B = 1.9 T. Minority-species and second harmonic heating have been demonstrated on Heliotron-E [56], and fundamental proton heating has been demonstrated on L-2 [57]. Another possibility is ion Bernstein wave heating [58] at the third cyclotron harmonic or higher frequency. These options have the advantages of direct ion heating, no driven toroidal currents, no hydrogen feed to the plasma, and available hardware but the disadvantages of mainly perpendicular heating, sensitivity to plasma shape, and the need for high-power antennas that can be close to the plasma, which must be developed for this application.

III.F. Energy and Particle Removal

An important element of the ATF mission is the development of effective methods for energy and particle (especially impurity) removal at high edge power densities, which is essential for steady-state operation. Failure to do this could lead to uncontrolled density increases and the accumulation of impurities in the plasma interior, resulting in large radiation losses and the possible collapse of the plasma stored energy (as observed in Wendelstein VII-A experiments [59]).

Energy Removal. Power will be lost from the ATF plasma in two ways: (1) in a more or less uniform illumination of the vacuum vessel wall from charge exchange and radiation and (2) in localized areas

from energetic and thermal particle losses. Charge exchange and radiation, assuming that ~30% of the input power is lost in this manner, would lead to relatively low wall power densities, ranging from ~1.2 W/cm^2 per megawatt of heating power under the HF coils to half that at the port locations. This power loss (corresponding to 60 MJ for 100 discharges with 4-MW, 0.5-s NBI pulses or 0.4-MW, 5-s ICH pulses) would result in a 60°C rise in the vacuum vessel temperature [60]. This is discussed in more detail in Sec. IV.C.

Vacuum vessel heating and wall sputtering can also result from neutral beam impacts near the entrance port or on the far wall after the beam passes through the plasma. To reduce these effects, the optimum beam injection direction was determined [61] by calculating the beam deposition in the plasma, on apertures, and on the vacuum vessel using an accurate model for the beam line geometry, the ATF vacuum vessel, and the 3-D magnetic field. The beam profile is modeled by Gaussians to fit the power profile measured on a beam test stand, and the plasma is assumed to have parabolic density and temperature profiles. Although the injection port is quite large, the beam diameter must be considerably smaller because of the tangential injection direction and the complex shape of the vacuum vessel wall.

These calculations [61] show that the best results are obtained for a beam centerline tangency radius $R = 1.97$ m, just inside the magnetic axis radius ($R = 2.1$ m). The beam is focused just outside the outer port location, nearly optimum for delivering the maximum power to the plasma. With no aperture in the beam line and $\bar{n}_e = 2 \times 10^{13}$ cm^{-3}, ≈93% of the neutral beam power is deposited in the plasma, ≈6% strikes the vacuum vessel, and a small amount hits outside the vessel port. Figure 30 shows that while attenuated (beam shine-through) neutrals hit the far wall, unattenuated beam neutrals hit the helical coil indentation on the lower right side. The wall power density is highest (>200 W/cm^2) just inside the port, where the cut for the HF coil is made. The beam shine-through loss is smaller, decreases exponentially with $\bar{n}_e$, and is spread over a larger area. Since the calculated local wall heating and sputtering rates exceed the ATF design values, an adjustable (20- to 25-cm-diam) beam-defining

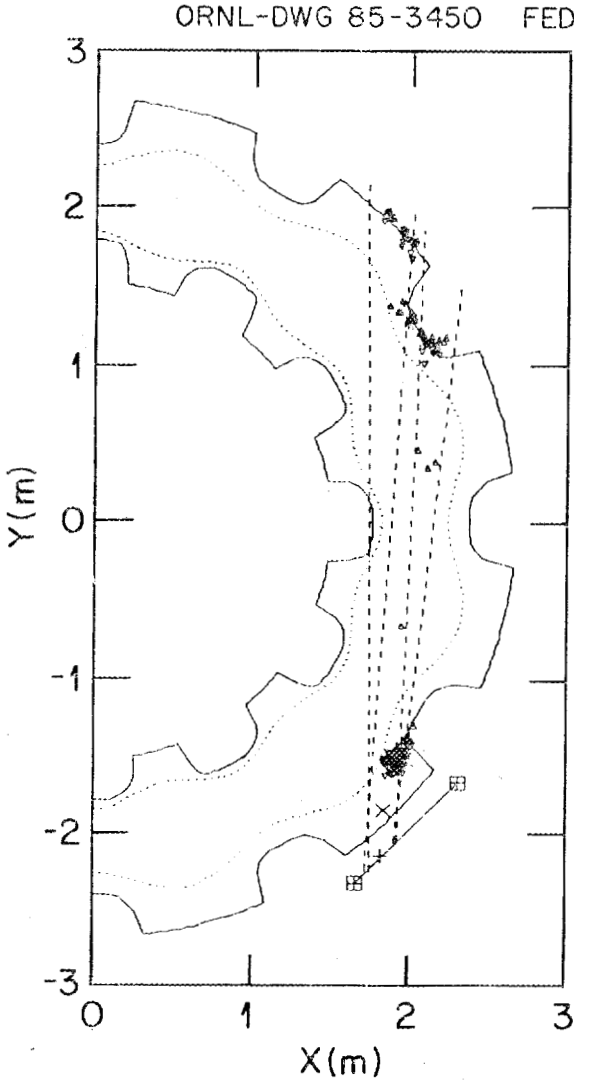

Fig. 30. Locations at which neutral beam particles hit the vacuum vessel: at the HF coil trough near the beam entrance (bottom) and after exiting the plasma (top).

aperture will be placed 0.6 m outside the port (or 3.5 m from the ion source). With the aperture set at a 22-cm diameter, 82% of the beam power is deposited in the plasma and a negligible amount on the vacuum vessel wall.

Energetic ion losses will occur in helical stripe patterns on the small major radius side between $\phi = 6^{o}$ and $\phi = 24^{o}$ unless the vacuum vessel wall is properly shaped (as in Figs. 2 and 3) [42] or unless these orbits, which range outside the last closed flux surface, are intercepted on protective top and bottom limiters. Both measures will be used in ATF to protect the walls from excessive energetic particle flux.

Computer calculations of magnetic field lines and thermal ion orbits, as well as experimental observations, indicate that the heat and particle fluxes will not be distributed uniformly over the plasma surface but will be concentrated in certain areas (like the "divertor traces" [62] in Heliotron-E). This is illustrated for ATF in Fig. 31, which shows field lines and 1-keV protons for launch points 2 cm outside the last closed flux surface. These areas of concentrated flux are natural locations for heat and particle removal. The energy and particle flux patterns will be studied experimentally during the early phase of ATF operation and before that in Heliotron-E. Pump limiters/divertors matched to these patterns will then be designed to optimize energy and particle removal. The divertor-like configuration of the magnetic field in ATF might allow an exhaust efficiency on the order of 10%, similar to that obtained with pump limiters in the Impurity Study Experiment (ISX-B) tokamak [63].

Particle Removal. The plasma will be fueled by gas puffing, by injection of fast (~1-km/s) hydrogen or deuterium pellets, and by accumulation of injected beam particles. For a volume-average plasma density $\langle n_e \rangle = 4 \times 10^{13}$ cm^{-3} and a particle confinement time τ_p = 0.05 s, the total particle outflux is 3×10^{21} s^{-1}. Assuming an exhaust efficiency of 10% (e.g., 90% recycling at the walls in pulsed operation or 10% collection efficiency with pump limiters in steady-state operation), the exhaust rate of 3×10^{20} s^{-1} can be balanced by 5 Torr·L/s of gas fueling, by 1.4 MW of 40-kV NBI, or by 1-mm-diam pellets injected every 100 ms.

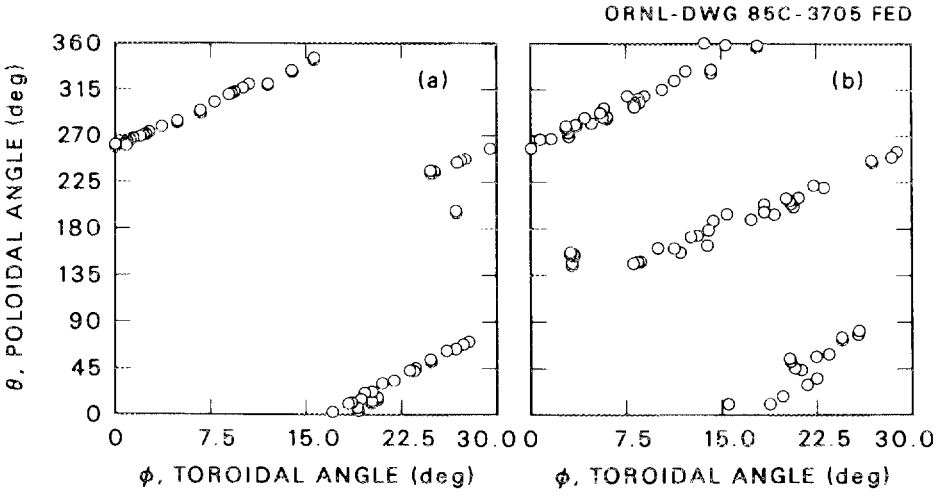

Fig. 31. Helical stripes of (a) field lines and (b) 1-keV H^+ orbits passing through a surface 5 cm outside the last closed flux surface.

With a pump limiter/divertor structure matched to the particle flow pattern, it is assumed that the pressure rise that can be achieved in the pump limiter/divertor is similar to that obtained in tokamaks, that is, on the order of 10^{-3} Torr. For an exhaust rate of 5 Torr•L/s, this would require a pumping speed of 5000 L/s, which appears feasible with various pumping schemes.

An important parameter for the design of a particle removal system is the connection length, the total path length of a field line after it crosses the last closed flux surface until it hits the wall. For ATF, calculations of field lines indicate that within the first few centimeters outside the last closed flux surface (at Z = 0.39 m), connection lengths correspond to several toroidal transits, as illustrated in Fig. 32. The connection length at Z = 0.49 m, 10 cm into the scrapeoff layer, is ~40 m, corresponding to three 13-m toroidal transits. This indicates that a pump limiter/divertor at one toroidal or poloidal location may be sufficient to intercept the total diffusive particle and energy flux crossing the plasma boundary.

Impurity Control. Light and heavy impurities are generated by the impact of energetic and thermal particles on in-vessel components. The impurity level in ATF will be controlled with a pump limiter/divertor for removal of gaseous impurities at the plasma edge in combination with reduction of the impurity source rate and reduction of the impurity confinement time. These impurity control measures have most impact on operating practice and relatively little impact on device design.

The impurity source rate can be reduced in a variety of ways: (1) conditioning the walls to control light impurities (oxygen, carbon), (2) reducing energetic particle bombardment of the wall through tangential NBI and shaping of the vacuum vessel wall, (3) reducing thermal particle and charge-exchange bombardment of the wall by using pellet injection and pump limiters to reduce edge recycling, and (4) choosing low-Z materials and coatings for in-vessel components. Of these techniques, tangential NBI and the shaped vacuum vessel wall have had the most impact on design of the ATF.

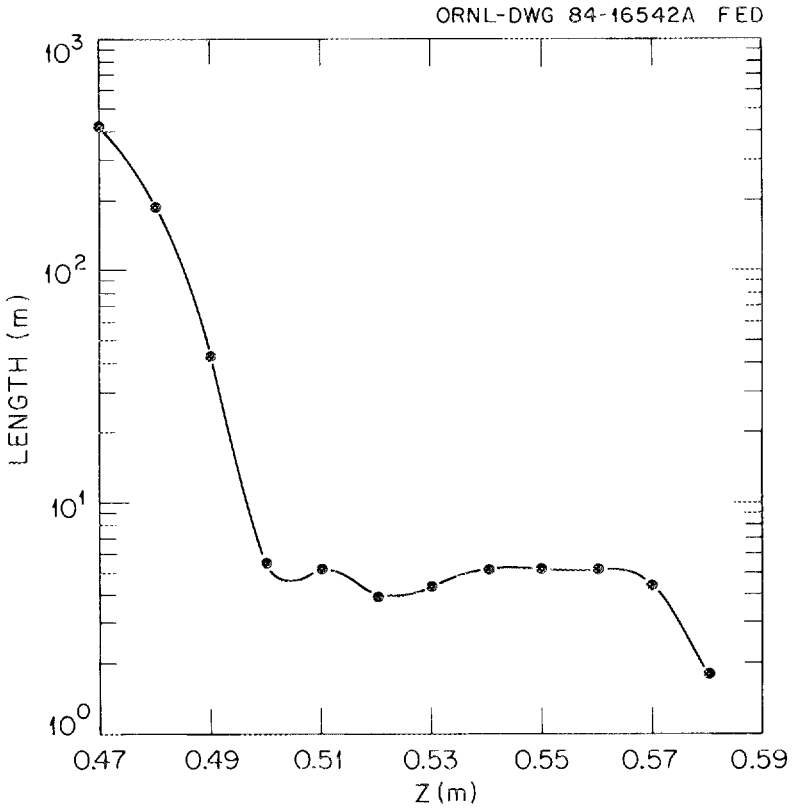

Fig. 32. Connection length vs the launch height Z above the axis in the $\phi = 0^{o}$ plane. The last "closed" flux surface is at Z = 0.39 m, and 13 m corresponds to one toroidal transit.

The impurity confinement time (and hence density) can be reduced through plasma edge control (which affects the global impurity confinement time) and through increase of impurity transport from the plasma core. The plasma edge properties can be modified through (1) gas puffing, (2) edge heating (with ECH or ICH), and (3) positioning of the $\iota = 1$ surface at the plasma edge. Impurity transport from the plasma core can be modified through (1) momentum input from co-injected and counter-injected neutral beams, (2) radial and poloidal electric fields, and (3) cyclic variation of the internal magnetic field structure, illustrated in Fig. 33. In this last technique, the VF coil currents are varied so as to cyclically produce and remove a bifurcated magnetic axis in the plasma interior. These oscillations, similar to sawteeth in tokamaks, might spoil the central confinement time without spoiling the exterior magnetic geometry.

IV. ATF DESIGN

Figures 1-3 show the main ATF components: two segmented, jointed HF coils; three pairs of PF coils, designated the inner, outer, and mid-VF coils; a thin, helically contoured vacuum vessel closely conforming to the HF coils; and an exterior shell structure to support the magnetic loads from the coils. Descriptions of these components follow in Secs. IV.A-IV.D.

A vacuum vessel interior to the HF coils, rather than one enclosing the HF coils, was chosen for ATF to ensure vacuum quality and to eliminate the problems associated with handling the magnetic loads and coil feeds through the vacuum vessel. Since the vacuum vessel is captured within the helical coils, it was decided to fabricate and install the major device components in parallel, as much as possible, in order to shorten the construction period for ATF. Other torsatron and stellarator coils have been successfully constructed by carefully winding hollow copper conductor onto the vacuum vessel [5], but this puts the manufacturing steps in series, requires the completion of a high-precision vacuum vessel before any winding can begin, and requires a thicker vacuum vessel to support the HF coil forces.

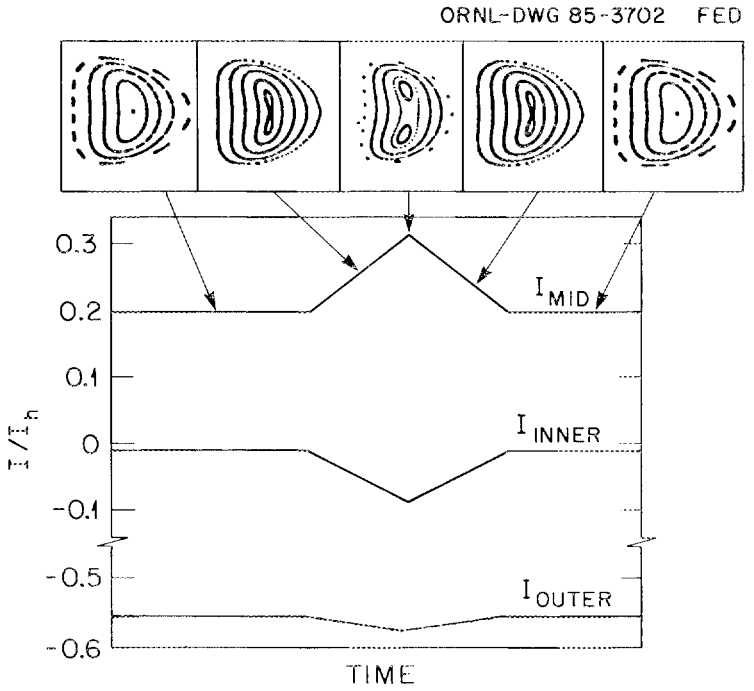

Fig. 33. Effect of cyclic currents in the VF coils. An internal separatrix can be created and removed without major effect on exterior flux surfaces.

Parallel fabrication permits a single-piece vacuum vessel that must support only atmospheric and small eddy current loads, but it necessitates segmented HF coils with joints.

A high degree of accuracy is required in the fabrication and assembly of ATF because low-order resonant field errors of the form $\Delta B/B = \varepsilon \cos(m\theta - n\phi)$ can cause formation of large magnetic islands and destruction of flux surfaces for $\varepsilon \geq 10^{-3}$. Figure 34 shows the effects on the ATF flux surfaces of an $m = 2$, $n = 1$ distortion of the HF coil winding. This type of field error is resonant with the $\iota = 0.5$ ($q = 2$) surface and is thus the most dangerous. Random errors or those with a high-order resonance are much less detrimental (deviations of ~1 cm can be tolerated), and errors that are the same in every field period merely represent an acceptably small change in the coil winding law.

Potential sources of field errors include inaccuracies in construction of the HF coil segments, misalignments in the VF coil sets or in the HF coils, coil current feeds, large nonuniformities in the magnetic permeability of the stainless steel components (the T-shaped structural supports for the HF coil segments or the structural shell), and large pieces of iron near the ATF (reinforcing bars in the floor or support platform, magnetic shielding for diagnostics, neutral beam line bending magnets, iron support platforms, etc.). In the design of the device and the facility, care has been taken to minimize these sources of error, as discussed in Sec. IV.E.

IV.A. Helical Field Coils

The HF coil set [64] consists of a pair of coils that form an $M = 12$, $\ell = 2$ constant-pitch torsatron with the design parameters shown in Table IX. The HF coils are being constructed so that the actual center of the current path is within 1 mm of the theoretical current path. To allow for parallel fabrication, the coils are being manufactured as a set of 24 identical upper and lower segments, 12 per coil, with joints in the horizontal midplane, as shown in Fig. 35. Parts for the HF coil segments are being fabricated by CBI Services, Inc., and assembled at ORNL. The segments are joined at device assembly [65] to form the continuous helical coils.

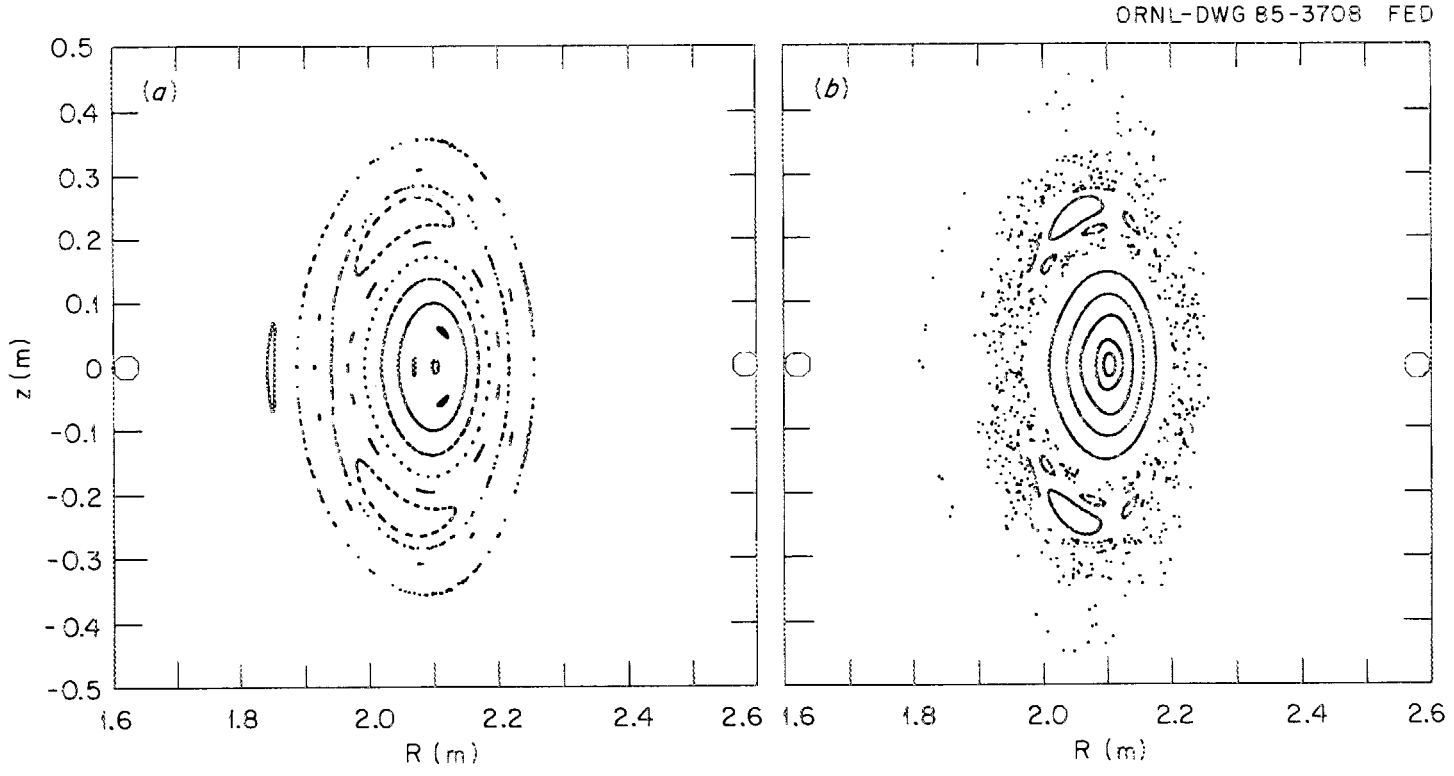

Fig. 34. Distortion of the ATF vacuum flux surfaces produced by a field perturbation of the form $\Delta B/B = \varepsilon \cos(m\theta - n\phi)$ for (a) an $\varepsilon = 1 \times 10^{-3}$, $m = 2$, $n = 1$ perturbation and (b) an $\varepsilon = 2 \times 10^{-3}$, $m = 2$, $n = 1$ perturbation. The small circles show the HF coil centers.

TABLE IX

ATF Coil Characteristics

	HF coil	Inner VF coil	Mid-VF coil	Outer VF coil	
				Main	Trim
Radius, m	2.1	1.33	1.69	2.94	2.94
z, m	---	±0.20	±0.85	±(0.47, 0.76)	±0.64
Weight,[a] tonnes	16.37	0.795	2.12	2.29 × 2	2.29
Number of turns	14	16	24	3 × 2	15
Conductor height, cm	2.86	3.63	4.45	6.35	4.45
Conductor width, cm	14.0	2.22	2.54	4.45	2.54
Hole diameter, cm	0.92 × 2	1.35	1.59	2.54	1.59
Conductor area, cm^2	37.3	6.63	9.32	23.2	9.32
Resistance[a] R, mΩ	2.45	3.86	4.95	(included	5.35
Inductance[a] L, mH	2.36	1.95	4.35	in HF)	4.05
L/R, s	1.04	0.51	0.88		0.76
Maximum current per coil, MA turns	1.75	0.263	0.306[b]	0.375	0.159
Maximum current per turn, kA	125	16.4	12.8	125/2	10.6
Maximum current density j, kA/cm^2	3.35	2.47	1.37	2.69	1.14
Water flow rate per coil set, L/min	17,800	490	950	2010	380
Number of cooling paths per coil set	480	8	12	8	6

[a] Values per coil.
[b] Due to force constraints, the mid-VF coil current is restricted to 0.306 MA for $B \leq 1.6$ T and to 0.17 MA at $B = 2$ T.

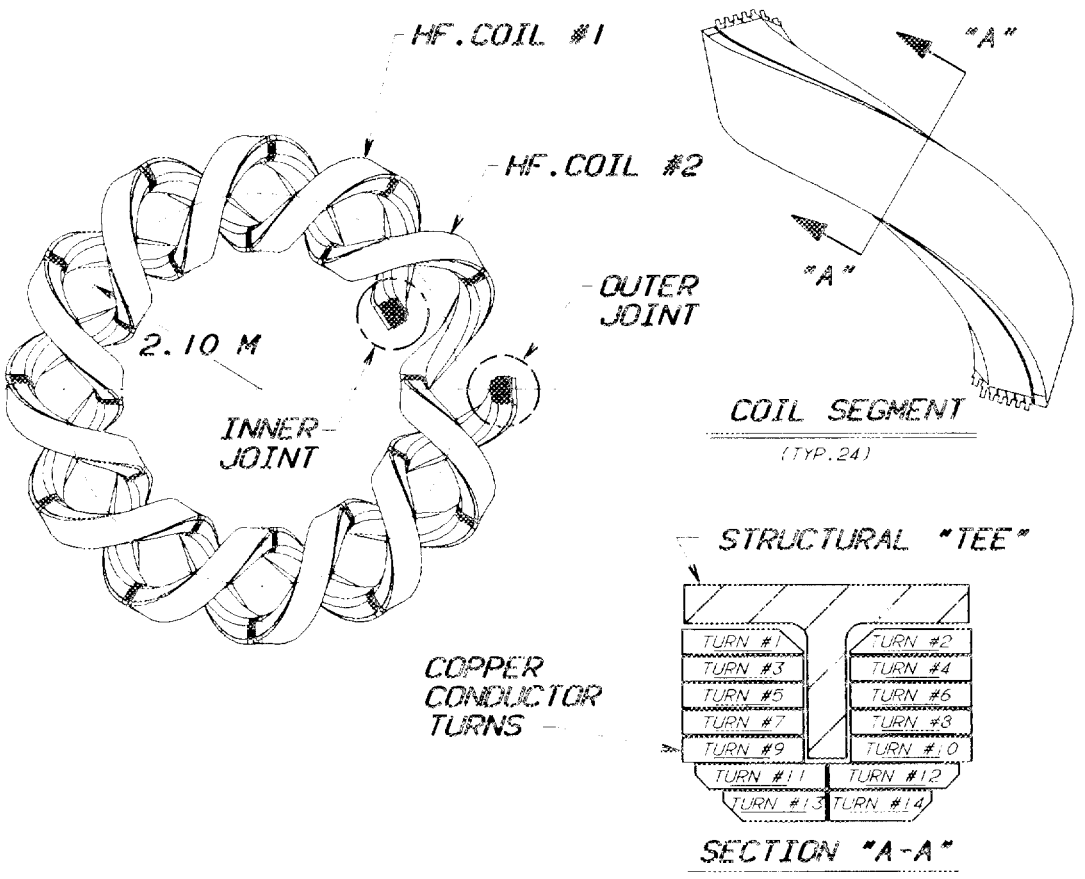

Fig. 35. HF coil concept.

A cross section of an HF coil segment is shown in Fig. 36. Each segment consists of 14 copper conductors wrapped with Kapton tape and separated by fiberglass and G-10 insulation, bolted to a T-shaped stainless steel structural support member, and vacuum-impregnated with epoxy. The large cross section (and the current density $j < 3$ kA/cm^2) results from the need to match existing power supplies, to have steady-state joints in the HF coils, and to have steady-state cooling for the HF coil segments. The "corners" of the HF coil cross section are chamfered to allow adequate distance between the plasma edge and the vacuum vessel wall. This constraint requires the inner turns to be slightly thicker, narrower, and clamped by three rather than by four bolts.

The assembly [66] of the HF coil segment is illustrated in Fig. 37. The conductors are made by machining flat developments from CDA 102 copper plate, brazing a cooling water tube into a milled groove, and bending the plate with rollers to the approximate shape. Then a complete set of conductors is clamped into a precision fixture and annealed to achieve the final form tolerance. The stainless steel T-piece is cast to shape to fit in its tolerance window and is then machined to provide accurate location points for mounting the conductors and assembling the coil. Following assembly, the segment is potted in epoxy resin. Figure 38 is a cutaway view of a completed HF coil segment.

A potted HF coil segment has been disassembled and repotted twice in the prototype development program by taking advantage of a differential de-encapsulation process [67] that separates the epoxy from the copper bars without softening the epoxy. This process allows examination of the effectiveness of the potting procedure and repair of a coil segment if necessary.

The demountable joint, which must meet the requirements for both pulsed and steady-state operation [68,69], is a critical design feature. These requirements are operation for 1,000 8-h "pulses" at 1 T, with the joint temperature rise limited to 100^{o}C, and a distribution of 60,000 5-s pulses (10,000 at 2 T; 15,000 at 1.5 T;

ORNL-DWG 84-3195 FED

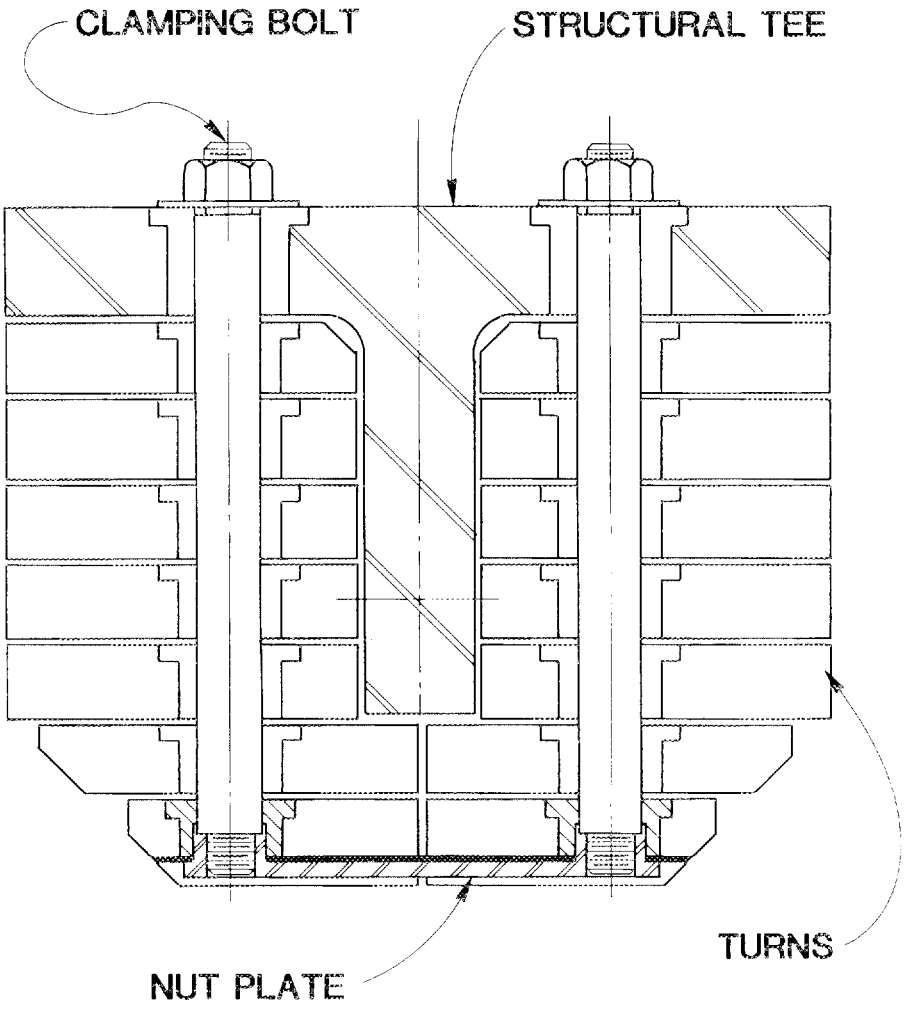

Fig. 36. Cross section of an HF coil segment.

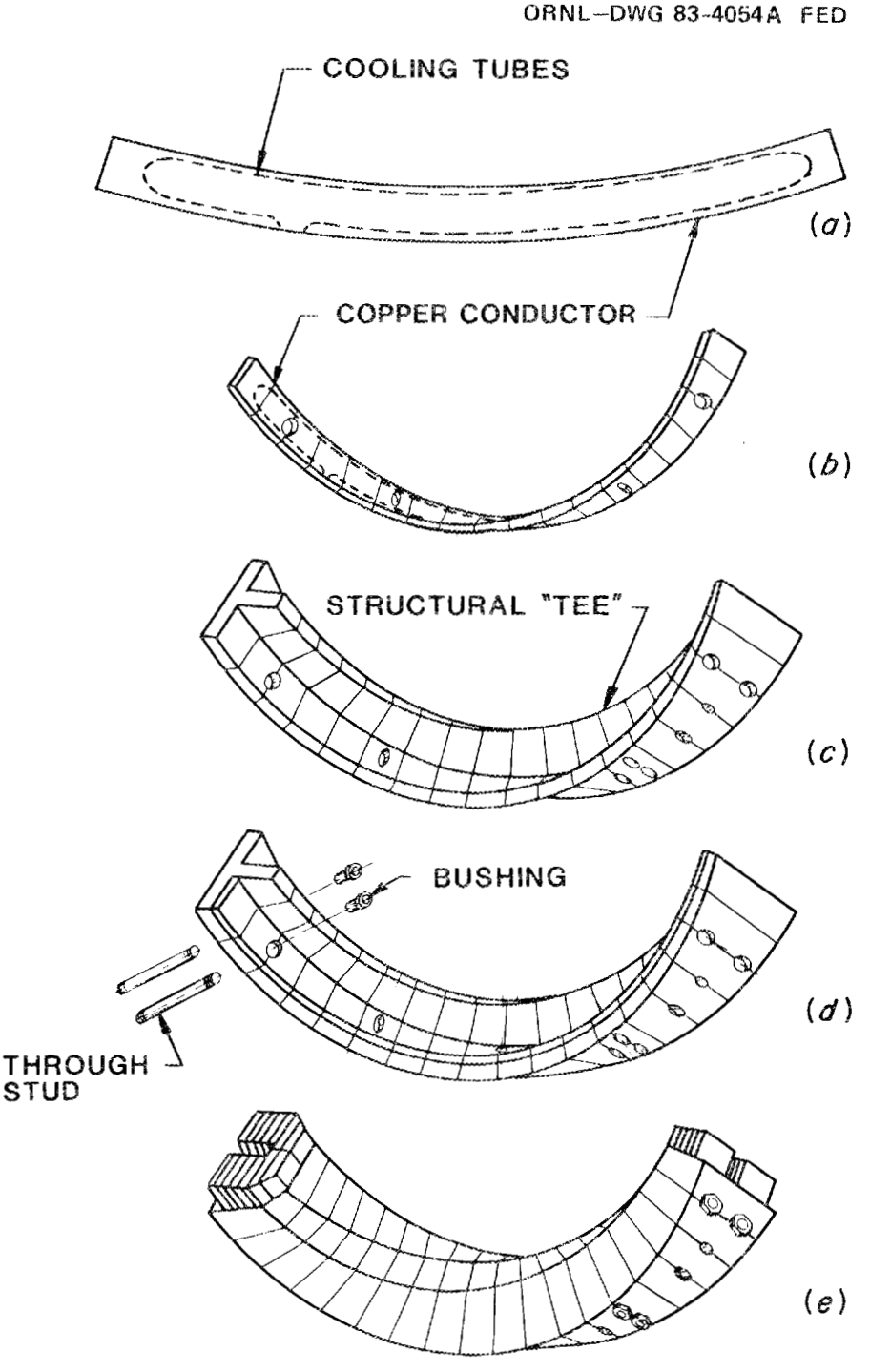

Fig. 37. The HF coil segment assembly procedure, showing (a) the flat development of a copper turn, (b) the formed and drilled turn, (c) the cast stainless steel structural T-piece, (d) a conductor positioned on the T-piece, and (e) a completed segment impregnated with epoxy.

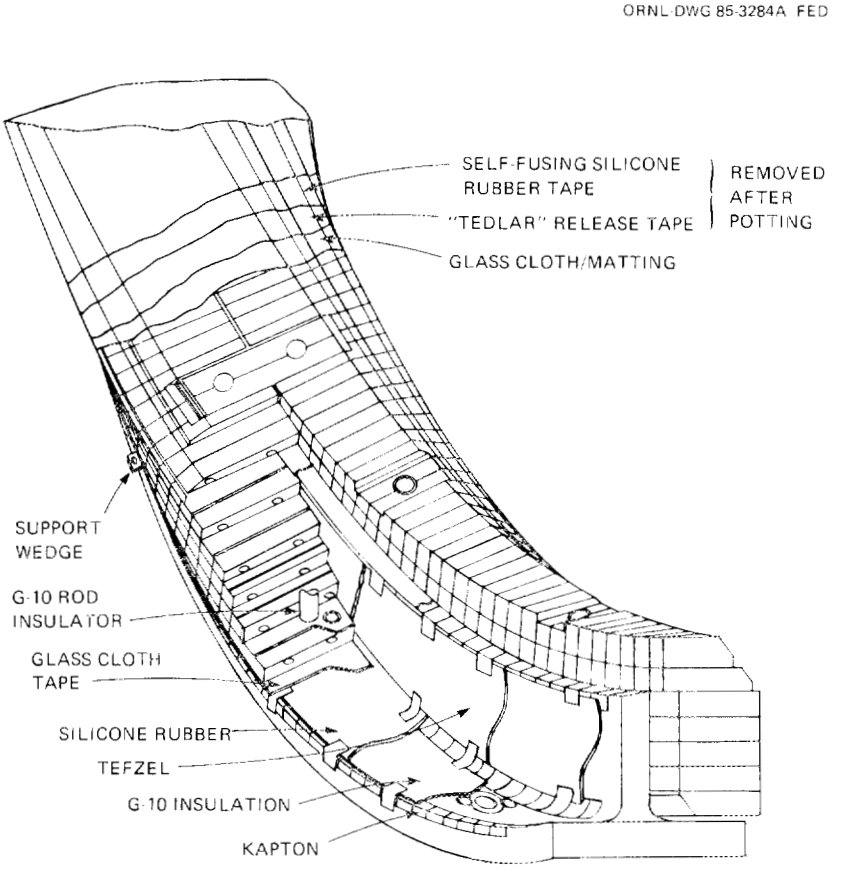

Fig. 38. Cutaway view of a completed HF coil segment.

25,000 at 1 T; and 10,000 in helical-axis mode at 1 T) that defines the minimum joint fatigue lifetime.

The selected joint concept (Fig. 39) is a simple lap geometry for each turn with bolts through the entire segment stack. Critical features of this joint include (1) flat contact surfaces, (2) adjustable wedge insulators to provide assembly clearance and prevent tolerance buildup due to thickness variations in the copper tabs, (3) match-reamed bushing and wedge insulators for good load transfer to the through-bolts to prevent slipping of contact surfaces, and (4) high-strength Inconel 718 studs with a centerless ground coating of fiberglass epoxy for extra insulation and tight fit. The current density for the inner turns is 6.9 kA/cm^2 in the joint tab and 2.7 kA/cm^2 in the contact area at B = 2 T.

The lap joint is composed of a half-lap machined tab at the end of each turn of a coil segment that mates with corresponding half-laps when upper and lower segments are joined during the HF coil assembly process. The tabs on each turn are machined while the copper conductor is still in a flat development stage. Each tab's position in the segment stack, including the holes for the joint through-bolts, is precisely controlled using tooling fixtures at the initial forming stage and again during segment assembly. This approach reduces the penalty for machining errors and provides the maximum amount of copper in the joint tabs or contact regions.

The through-bolts are a sliding fit to match honed G-11CR bushings in each joint tab hole. The composite material G-11CR, rather than the G-10 used elsewhere in the HF coil segment, is used in the joint region because of its higher compressive strength and its better properties at the higher temperatures occurring at this location. The bolts are actually studs that engage a floating nut plate located at the innermost turn joint. The studs are tensioned and the load is secured by a nut applied to the outer end of the stack to provide joint contact pressure.

The joint is made up during HF coil assembly, as shown in Figs. 35 and 39 (see also Fig. 44). Field assembly of the HF coil joints is based on optical alignment to a particular joint feature on each

ORNL-DWG 85-3728 FED

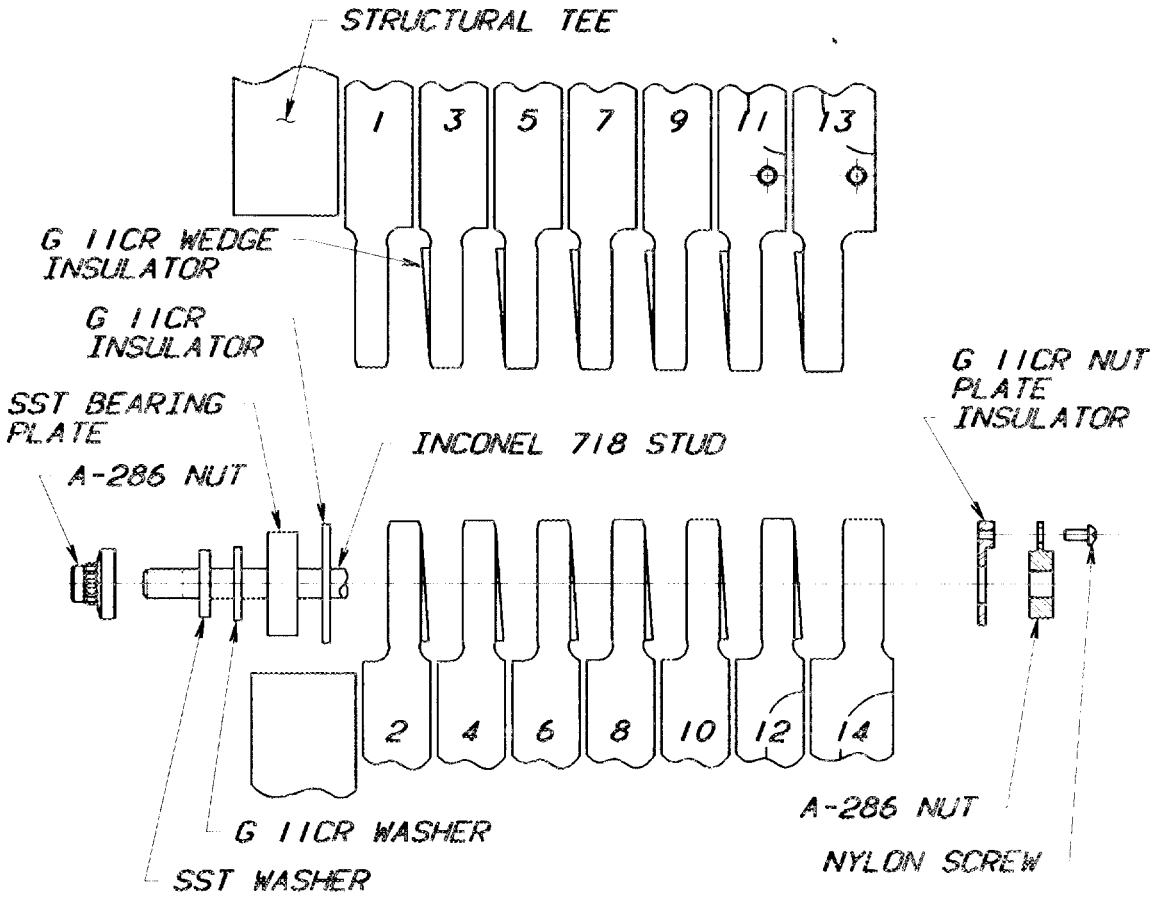

Fig. 39. Cross section of HF coil in joint region. The insulating wedges are arranged for a current crossover connection.

segment end. Joint tab misalignments (nonparallel surfaces) are corrected by assembly forces as the upper and lower segments are engaged. Tests of actual joint ends have been conducted [68] and verify this behavior. As the coil segments are engaged, tapered G-11CR insulating wedges installed between turns are actuated to fill the gap and provide a solid block for through-bolt load transfer to each turn.

The joint connections on the inside of the torus (small major radius side) simply transfer the current across the joint to the same layer of conductor, while the joint connections on the outside of the torus (large major radius side) are current crossovers that transfer the current from layer to layer, thereby putting all turns in a helical winding in series. The type of joint depends on the side of the conductor tab on which the insulating G-11CR wedge is located. The current feeds to the two HF coils occur at two outer adjacent joints on each coil that are located 60° apart toroidally. The magnetic field perturbations associated with the current feeds are minimized since these feeds carry only one-fourteenth of the total HF coil current and the 60° toroidal connections occur 4 m below the joint. Shunts are used at the eight remaining outer joints to preserve symmetry.

Tests on joint specimens [69] and related calculations have been made to verify joint capability and operating margin for steady-state operation at 1 T and 5-s pulsed operation at 2 T. Tests of joint resistances through the stack showed that all joints had a measured resistance of 1 $\mu\Omega$ or less. Thermal-electric tests show adequate cooling for all joint configurations and hot-spot temperatures below the 1-T steady-state limit of 100°C.

Calculations of the expected number of cycles to failure [68] show more than a factor of 10 margin over the ATF operating requirements at 2 T. The predicted number of life cycles (including a factor of 10 safety margin) from stress analysis is 14,000 at B = 2 T (vs the required 10,000 pulses). The actual fatigue lifetime should be considerably higher, since stress redistribution within each turn is not included in the analysis and the fatigue testing measurements gave

230,000 cycles, half with a full-width crack produced inadvertently under a doubled load. The number of predicted life cycles is 10^5 at B = 1.5 T and 10^6 at B = 1 T.

IV.B. Poloidal Field Coils

Three sets of PF coils (or VF coils) are required: an inner pair, a mid-VF pair, and an outer pair, as discussed in Sec. II.B. The locations of these coil sets [70] are shown in Figs. 2 and 3. The coil parameters are given in Table IX. The coils, built by Princeton Plasma Physics Laboratory, are all wound from hollow CDA 104 silver-bearing copper conductor and insulated with half-lapped layers of a polyester Mylar tape and a semicured polyester-treated glass tape. The windings must be circular to within $\pm$5 mm. The most serious misalignment would be a relative displacement (shift) of the centers of the HF and VF coil sets by $\geq$1 cm. Precisely located brackets permit the required accuracy in the installation of the VF coils.

Each set of VF coils is independently powered for configuration flexibility. The inner VF coils are operated in series from a single power supply, as are the mid-VF coils. Each outer VF coil has three independently connected windings, including two main sections and a trim section. The main sections are connected in series with the HF coils and provide the field that offsets the vertical field from the helix. Two main sections are required in each outer VF coil to maintain symmetry during helical-axis operation, when one of the HF coils is operated at reduced current. The trim section is powered from a separate power supply and can be energized to its maximum current in either direction.

Fabrication of the inner and mid-VF coils presents no significant problems. However, the large copper conductor cross section of the outer VF coils (4.45- by 6.35-cm conductor with a 2.54-cm-diam cooling passage in the main sections) required solutions [70] to problems of variable hardness within a single conductor length and difficulty in making a high-strength, induction-brazed joint.

IV.C. Vacuum Vessel

The vacuum vessel [60,71], shown in Fig. 40, is a thin-walled (6-mm), 304L stainless steel torus with a circular cross section (R = 2.1 m, a = 0.58 m) and with a helical indentation, the cross section of which closely matches the inner bore and sidewall of the HF coils to maximize the plasma-wall separation. The plasma-wall separation varies over the vacuum vessel interior, with the minimum distance (~10 cm) occurring under the HF coil corners, particularly on the small major radius side. In addition, there are straight sides in the region above and below the HF coil joints to allow clearance for vertical installation of the HF coil segments. There is a nominal 1-cm gap between the outside of the vacuum vessel and the HF coils to allow access to the HF coil joint region and room for a 6-mm radial expansion of the vacuum vessel when it is heated to 150°C (by 2-kW, 2.45-GHz cw ECH discharge cleaning or by inductive heating).

Cross sections of the vacuum vessel at $\phi = 0^{\circ}$ and $\phi = 15^{\circ}$ are shown in Figs. 2 and 3. The interior dimensions (minimum) are roughly 1.16 by 0.65 m. The vacuum vessel volume is 10.5 m^3, and the interior surface area is 62.6 m^2. The 12 large parallelogram-shaped outer ports (0.9 by 0.6 m) allow tangential NBI access for a 22-cm-diam beam. Square ports (0.35 by 0.35 m) were chosen for the 12 top and 12 bottom ports instead of the alternative 0.4-m-diam round ports because the square ports permit 0.5-m diagnostic access radially and toroidally along the port diagonals. Vertical access to the 12 0.2-m-diam inner ports is limited to 15 cm by the inner VF coil support structure.

The vacuum vessel [71] is being fabricated by Pittsburgh-Des Moines Corp. from about 1200 small sections of stainless steel plate, which are shaped to the required fit on a precision forming fixture that forms an internal mold of the vessel contour. The forming fixture consists of 360 steel plates, one each degree toroidally, having the shape of the vacuum vessel cross section at that location. These plates are mounted on a high-precision base plate to ensure dimensional integrity during fabrication and removed through the

ORNL–DWG 85-3623 FED

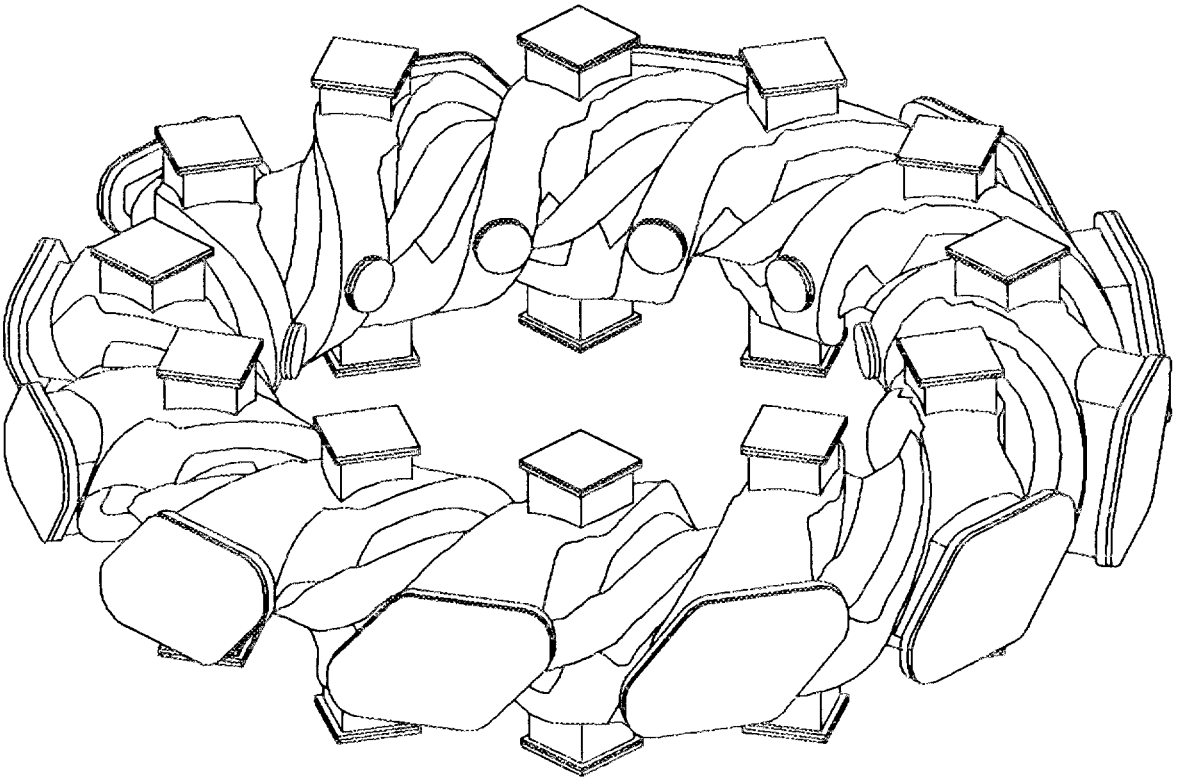

Fig. 40. View of ATF vacuum vessel showing the helical groove for the HF coil segments, the large (0.6- by 0.9-m) outside ports, the square (0.35- by 0.35-m) top and bottom ports, and the small (0.2-m-diam) inside ports.

outside ports after the vacuum vessel is completed. Each small plate section of the vacuum vessel is formed on a hydraulic press to its complex curved shape, individually fitted, and tack welded to its neighbors. Full-penetration welding of the completed vacuum vessel from both outside and inside using Inconel filler rod will minimize magnetic permeability.

Because the vessel carries only atmospheric pressure and a slight (0.3-atm) induced electromagnetic load, the wall is only 6.4 mm thick. This provides sufficient toroidal resistance (0.5 mΩ) to avoid the need for bellows or insulating breaks and gives a 10-ms time constant for penetration of the poloidal fields that may be needed to shift the magnetic axis, control the plasma shape, or induce a plasma current.

The temperature response of the uncooled vacuum vessel has been studied [60] using a 3-D heat diffusion model with natural and forced-air convection outside the vessel for two extreme cases: (1) concentrated heat deposition in a 3.8-cm-wide helical strip at r = 0.59 m (between helical troughs), which might occur in divertor-like behavior, and (2) uniform heat deposition over the vacuum wall, which might result from radiative or charge-exchange losses from the plasma. For the concentrated heat deposition case, local heating to 150°C occurs for 1.5-MJ total deposition (140 W/cm^2 for 0.5 s), but the vessel cools down sufficiently through heat redistribution to allow a 10-min repetition rate. Retractable top and bottom limiters will be used to prevent deposition of high plasma heat flux on the vessel wall. For the uniform heat deposition case, the vacuum vessel heats to 150°C for 150-MJ total deposition, after which it must cool down for a long time (~8 hours for forced-air convection or ~24 hours for natural convection over the vacuum vessel). Although initially there will be no active cooling, space is provided inside the vacuum vessel for water-cooled panels that would permit high-duty-cycle or continuous operation.

Clean vacuum conditions will be produced through conditioning of the walls, metallic seals, and adequate pumping speed. Conditioning to control light impurities, such as oxygen and carbon, will be done with 2-kW, 2.45-GHz cw ECH discharge cleaning, glow discharge cleaning,

and vacuum vessel bakeout with induction heating at 60 Hz using a 100-kVA transformer connected to the HF windings. Metallic seals on the port flanges permit temperatures of up to 150°C for discharge cleaning and initial operation. The top, bottom, and inside ports use knife-edge flanges on flat copper gaskets, and the outer ports use a special aluminum-jacketed Helicoflex metal seal. Three 2000-L/s turbomolecular pumps will be mounted at the end of a duct 0.6 m in diameter by 2.5 m long, so that the stray field at the pumps will be acceptably low (<15 G).

Finite element structural analysis studies [71] for the ATF vacuum vessel were done for static load conditions (gravity, vacuum, and temperature loads) to check the adequacy of a 6-mm-thick wall. A 30° sector of the vacuum vessel was modeled, as shown in Fig. 41, using PATRAN [72] as a pre- and post-processor with MSC/NASTRAN [73]. The ports and flanges tend to support the vacuum vessel wall. The maximum principal stresses are 91.7 MPa (13,300 psi) in a localized area at the base of the square ports, and the maximum deflection is about 1 mm near the base of the outer port. The stress in the trough region is 55.2 MPa (8000 psi), close to that found with a simpler model (without ports) that used cyclic symmetry to establish consistent boundary conditions with MSC/NASTRAN. This analysis gave a maximum principal stress of 55.8 MPa (8100 psi). A buckling analysis with vacuum loads predicted buckling at 11.5 times the actual vacuum load.

IV.D. Support Structure

The machine support structure is designed to position the HF and VF coil sets accurately and support them against the magnetic, thermal, and gravity forces. The principal loads on the HF coils are due to thermal and magnetic forces that lead to radially outward hoop loads and overturning or side loads. These loads have been calculated using the BARC [74] and MAGFOR [75] computer programs. Both radial and axial components of the force on the HF coils vary approximately sinusoidally along an HF coil period, as shown in Fig. 42. The net radial force component is always radially outward (hoop force) and varies from 0.63 MN/m at the outside to 1.39 MN/m at the inside in

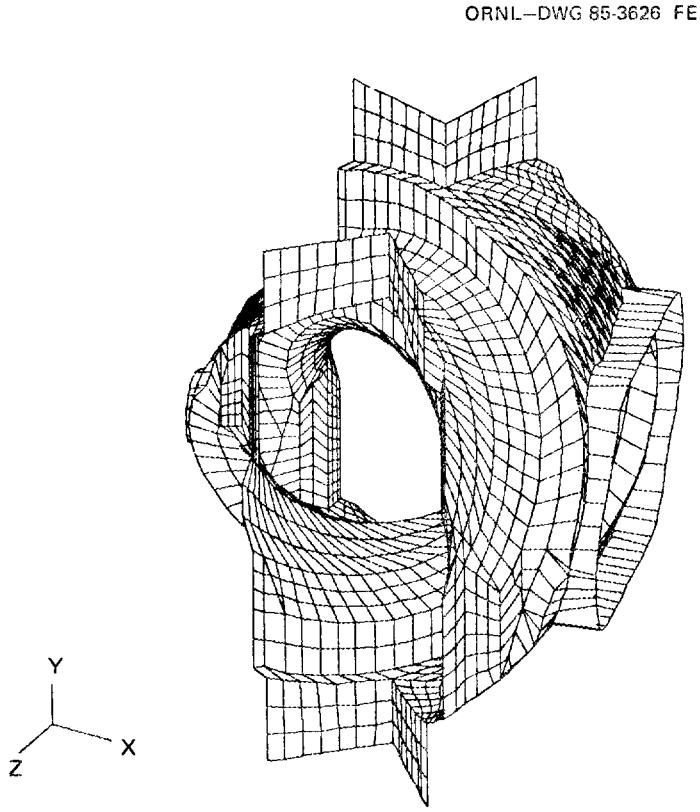

Fig. 41. An outside view of 30^{o} segment of the ATF vacuum vessel generated with a finite element model used in the stress analysis calculations.

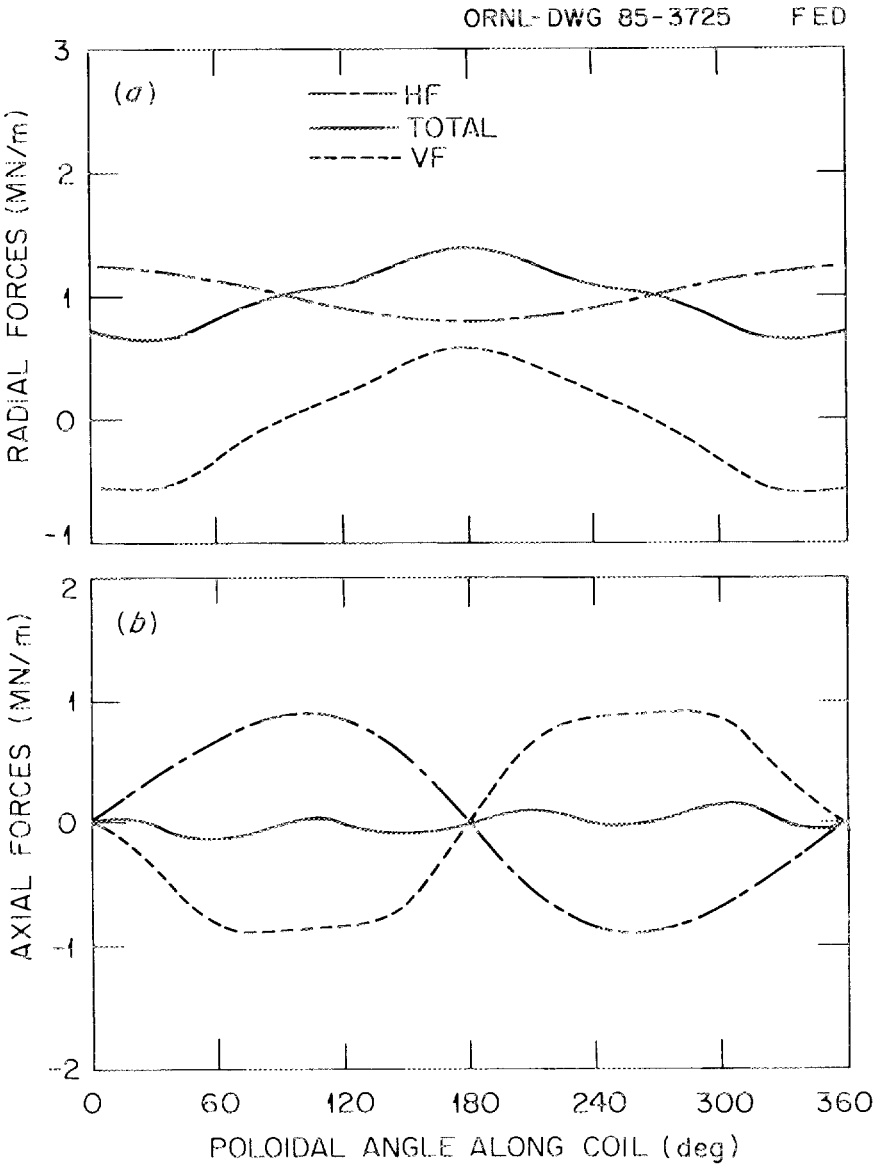

Fig. 42. Distribution along the coil length of (a) radial and (b) axial force components on the HF coils at B = 2 T. The curves show the contributions due to the HF coils, the VF coils, and their sum.

major radius, reflecting a net centering force. The side (axial) component of the force, which changes sign along the coil, is reduced considerably (by a factor of 6) by connecting the HF coil and the main sections of the outer VF coils in series to ensure a minimum net vertical field. Within the HF coil itself, the attractive force between the conductors and a torque about the coil center are both taken in the structural T-piece. The epoxy and fiberglass of the HF coil segment form a compressive load path to transfer the nonradial component of the magnetic forces on the conductors into the structural T-piece. The copper conductors are allowed to expand in the minor radius direction through the use of rubber "crush planes." This radial expansion manifests itself primarily as hoop tension in the copper conductors.

The HF coil support structure is an external toroidal shell, fabricated by Westinghouse Nuclear Components Division, composed of identical upper and lower toroidal shell segments, cast from stainless steel, and intermediate connecting panels. The shell components are bolted together, and the structural T-pieces are connected to the shell by studs and adjustable structural ties. The top and bottom shell segments are 4 cm thick and have an inside radius of 0.66 m. The flat, 5-cm-thick stainless steel vertical connecting panels allow access to the inside and outside horizontal ports. The shell forms a compact structure that allows maximum access for diagnostics and neutral beams. The lower half also serves as an assembly fixture for the HF coils through the use of adjustable tooling balls that precisely locate the HF coil segments, as indicated in Fig. 3. As shown in Fig. 43, the shell segments are joined at insulated, bolted flanges to prevent circulating eddy currents.

When the HF coil set is energized, the primary radial force is carried by the copper conductors. In an earlier design [15], the radial force was to be transmitted from the coil structural T-piece through epoxy-filled bladders into the structural shell, where it would be carried in hoop and axial tension. This determined the thickness of the structural shell. The actual design retains the epoxy-filled bladders but allows for radial and longitudinal motion, so the HF

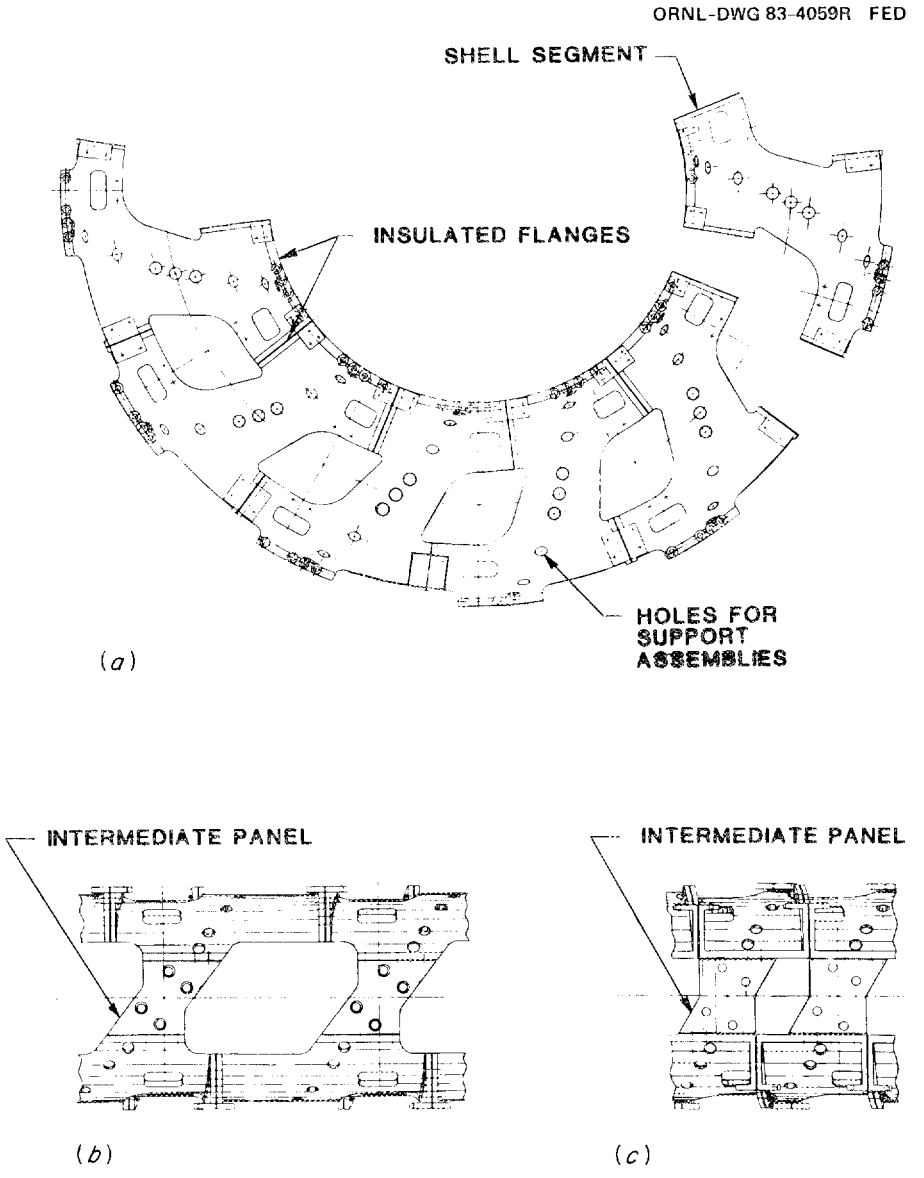

Fig. 43. The 4-cm-thick, segmented shell support structure for ATF. (a) Top view. (b) Outside view. (c) Inside view.

coils are only constrained axially (toroidally) in the shell. The side or overturning moments are transmitted through special shear attachments into the shell and are carried as a torsional load between the upper and lower shell assemblies.

The principal VF coil loads are a radial hoop force and a vertical force of interaction between the HF and VF coils and between the VF coils in a pair. A finite element stress analysis of the outer VF coil showed that the shear stresses in the epoxy glass layers between coils greatly exceeded the ultimate stress of this material, so intercoil slip planes were incorporated into the outer VF coil bundle. If the coils were bonded together, they would delaminate at the nominal operating conditions, not only at the coil-to-coil interfaces but possibly also between layers due to shear transfer or crack propagation within the coils.

The vacuum vessel weight is supported from the upper half of the shell on a set of pinned supports that allow thermal expansion in the radial direction. The entire device rests on 18 columns located under the shell segment flanges.

IV.E. Accuracy in ATF Construction

The need for high accuracy in fabrication and assembly of the ATF components, as discussed previously, and the desire for a rapid fabrication and assembly schedule have led to the development of some innovative techniques for ATF construction. Accuracy in fabrication is obtained through use of a Sheffield Measurement Division five-axis computerized coordinate measuring machine [76] that can measure parts to an accuracy of ± 0.01 mm in a volume of 2 m x 1 m x 1 m. It has been programmed to automatically measure a part and display out-of-tolerance points. Accuracy in assembly will be obtained using a computerized optical triangulation system (twin electronic theodolites) manufactured by Wild-Heerbrugg Instruments [77] with an accuracy of ± 0.025 mm at a distance of 6 m. A computer program will determine the translations and rotation required to bring a part (e.g., an HF segment) into alignment with an accuracy of ± 0.25 mm. Accuracy in the relative positioning of the current centers of the ATF

coil systems will be ensured using a field-null method developed for ATF [78] and tested in experiments on URAGAN-3 [79]. This method can determine coil current alignment errors (shifts, tilts) to an accuracy of ±2 mm.

The structural member or backbone for the HF coil segments is the stainless steel T-shaped piece shown in Fig. 37(c). This helical piece is 2 m long, 4.4 cm thick, 32.2 cm wide, and 20 cm in radial depth; weighs 400 kg; must be accurate to ±6 mm; and must have reasonable cost and fabrication time, since 24 are required for the full HF coil set. Precision stainless steel castings are inexpensive (~3 $/kg vs ~15 $/kg for machined pieces), but a large number (typically 10-20) of trial-and-error attempts had previously been required to get the desired accuracy. As part of the ATF project, a method was developed at ORNL that obtains, in two or three tries, a precision mold that gives repeatable castings [80]. Using this method, the casting of each structural T-piece was reduced from 900 kg and ±19-mm accuracy to 400 kg and ±1.5-mm accuracy. The method uses the coordinate measuring machine and an energy minimization technique to find the part orientation with the smallest integrated rms deviation from the optimum piece. The casting molds can then be optimized quickly, and the castings are quite repeatable.

The copper bar conductors for the HF coil segment are formed to an accuracy of ±0.25 mm using an accurate forming fixture similar to the stainless steel T-pieces but with high-precision (±0.025-mm accuracy) end fixtures to position the joint tabs on the ends of the HF segment. Numerically controlled machining techniques [80] were developed to eliminate setup errors in fabricating this fixture. The normal approach would have been to use a three-axis mill with standard numerical control techniques, requiring >2200 hours and precise alignment of the part when it must be moved to allow access to different regions of the part during machining. This typically introduces setup errors of ±2.5 mm. In our technique, the part is moved to its approximate location, the machine tool measures the part location, and the computer transforms the machine tool coordinates into the part coordinates, eliminating any setup errors. This approach, using

a five-axis mill with computer control, takes ~500 hours, and the final forming fixture is accurate everywhere to $\pm$0.25 mm.

The major ATF components are shown in the assembly sequence illustrated in Fig. 44. After the concrete base and support columns are installed, the lower VF coils are installed and the lower half of the structural shell is assembled and optically aligned. Adjustable tooling balls are accurately located in the lower shell to form a reference datum for positioning each lower HF coil segment. Next, the 12 lower HF coil segments are installed and accurately aligned using the optical alignment system. The vacuum vessel is lowered into position as a unit. Next, the 12 upper HF coil segments are installed and attached to the lower HF coil segments by making up the coil joints. Alignment fixtures are used to pull the coil joints together by slightly deforming the copper end tabs where interferences exist. The upper half of the structural shell is then installed and attached to the lower half by the intermediate connecting panels. As the last step, the upper VF coil sets are attached to the shell and aligned. Brackets attached to the shell flanges locate the inner and outer VF coil pairs, and adjustable columns between VF coil pairs carry the principal VF coil loads. Adjustable ($\pm$1-cm) interfaces between the shell and the coils relax the positional tolerance requirements on the shell.

A final check on the accuracy of the installed HF coils and the (adjustable) VF coils will be obtained by measuring the locations of the nulls in the radial magnetic field component when oppositely directed currents are fed to the two HF coils or to the two circular coils in each VF set. This method [78] is fast, can be done with the vacuum vessel open, and can detect both distortion and relative misalignments (shifts, tilts) in the VF coil sets with an accuracy of $\pm$2 mm. It has been tested on the URAGAN-3 torsatron at Kharkov [79], where it detected a 1-cm relative shift between the $\ell = 3$ helical coil system and the circular VF coil set.

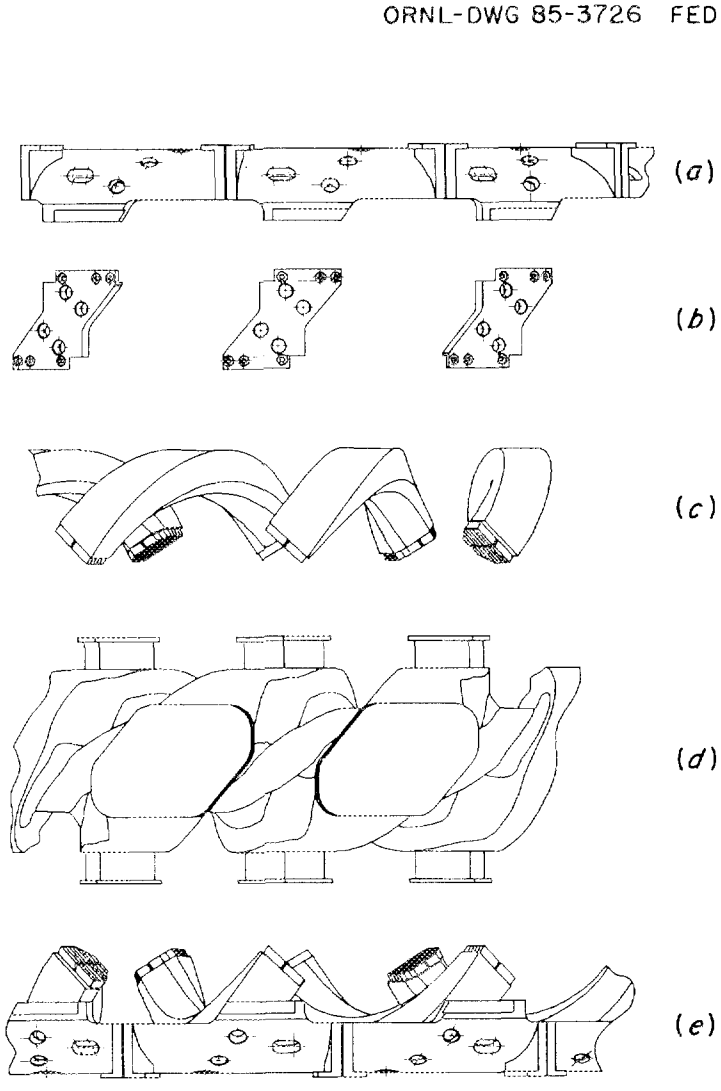

Fig. 44. The major ATF components in the assembly sequence, showing (a) the upper half of the structural shell, (b) the intermediate connecting panels, (c) the upper HF coil segments, (d) the one-piece vacuum vessel, and (e) the lower HF coil segments positioned in the lower half of the structural shell.

V. ATF SUPPORT SYSTEMS

In addition to the device itself (coil systems, vacuum vessel, and support structure), systems required for operation of the ATF include power supplies, plasma heating and fueling systems, energy and particle removal systems, and plasma diagnostics [81]. This section discusses the two largest systems: the power supplies and plasma heating systems. Energy and particle removal issues are discussed in Sec. III.F. The ISX-B plasma diagnostics [82] are being modified for ATF to better analyze the more complex 3-D plasma configuration and to adapt to the 15^{o} toroidal difference in the horizontal and vertical port locations.

V.A. Power Supplies and Cooling

Four power supplies are required for the four independent ATF coil systems: the HF coils and the inner VF, mid-VF, and outer VF coils. All coil power supplies consist of transformer/SCR assemblies. These power supplies must operate for up to 5-s pulses at full field (2 T on axis) and steady state at 1 T. The coil and power supply characteristics are given in Table X. The current and voltage capabilities of the power supplies exceed the maximum design values in order to provide extra flexibility. Each VF power supply covers the range needed to create the configurations shown in Fig. 16 at B = 1 T, where the high-beta studies will be conducted and the most configuration flexibility is required. The inner VF and mid-VF power supplies are restricted to about half this range at B = 2 T due to force constraints.

The HF power supply is based on eight transformer-rectifier modules (each 625 V no-load and 7.8 kA steady-state or 31.3 kA pulsed) configured in parallel for steady-state operation (62.5 kA, 625 V) and in four parallel strings of series pairs for pulsed operation (125 kA, 1250 V). This power supply also feeds the main (upper and lower) sections of the outer VF coil that are in series with the HF coils. For helical-axis operation, the current in one helical coil and its associated outer VF coil sections will be reduced using an auxiliary resistive shunt.

TABLE X

Coil and Power Supply Characteristics

	HF + Outer Main VF Coils	Inner VF Coils	Mid-VF Coils	Outer Trim VF Coils
Maximum design current I, kA	125	16.4	12.8	10.6
P.S. current, kA	125	18	30	18
Maximum IR, V	719	120	127	112
P.S. no-load voltage, V	1250	650	144	650
Power at maximum design current, MW	89.9	1.97	1.63	1.19
Fraction of I_h at B = 1 T	1	$\pm$0.30	$\pm$0.35	-0.61 to -0.25
Fraction of I_h at B = 2 T	1	$\pm$0.15	$\pm$0.10	-0.52 to -0.34
Desired fraction of I_h (Table VII)	1	-0.03 to +0.33	+0.27	-0.41 to -0.59

Power supplies for the outer trim VF coils and the inner VF coils consist of two transformer/SCR assemblies connected in parallel by an interphase transformer. These supplies provide a maximum current of 16 kA and 650 V of no-load voltage in pulsed operation and will work, with some reconfiguration, in steady-state operation. The mid-VF coils will use an existing power supply consisting of a battery bank and a transistor-diode switching bridge with a 2- to 3-MW rating for pulsed operation and a new 14.2-kA, 250-V supply, similar to the other VF power supplies, for steady-state operation.

The HF power supply is fed from a substation with three 13.8-kV, 40-MVA transformers, and the VF power supplies are fed from another 50-MVA substation. Control is accomplished using the SCRs in 6-phase or 12-phase configurations. The 360-Hz ripple associated with the 6-phase arrangement is acceptable because of the long L/R times of the coils. A computer system with VAX-based software and a CAMAC hardware interface is used to monitor performance and provide protection. For both pulsed and steady-state operation, the supply outputs will be controlled by an analog drive signal, rather than by direct digital control of SCR firing pulses. This offers more flexibility, including the possibility of implementing feedback regulation of either the power supply currents or appropriate plasma parameters.

Demineralized cooling water for the ATF coils and associated electrical bus work is provided by a 40-MW, 104,000-L/min cooling water facility. The 32.5-MW continuous cooling required for steady-state operation at 1 T is a more severe constraint on the cooling system than the cooling needed for 5-s, 2-T pulses every 10 min. The steady-state power dissipation is 22.5 MW in the HF coil system, 2.4 MW in the VF coils, 3.9 MW in the electrical buswork, and 3.7 MW in the power supply rectifiers. The cooling system is designed to limit the copper temperature to 100^{o}C in the uncooled HF coil joint regions and 65^{o}C in the VF coils.

V.B. Plasma Heating Systems

Electron Cyclotron Heating. The ECH transmission system [83] (waveguide, mode absorbers, bends, a dummy load, launchers, and other

components) features a mode-controlled, quasi-optical, 6.35-cm-ID vacuum waveguide with 90^{o} miter bends. The waveguide components will have high average (steady-state) power-handling capability, since the gyrotrons and power supply are also rated for cw operation, and sufficient bandwidth to allow operation at 28 GHz or 60 GHz with appropriate gyrotrons.

An evacuated (10^{-5}-Torr) waveguide system is favored because its power handling surpasses that of pressurized waveguide systems. Elimination of the barrier window at ATF improves the system efficiency and reliability. An all-metal, rf-compatible gate valve is used to isolate the ECH waveguide vacuum from the ATF vacuum. The natural output mode of the gyrotrons is the TE_{02} circular electric mode, which is ideal for long-distance transmission because of its very low attenuation in oversized waveguides. This allows moderately long (20-m) waveguide runs from the ECH system site to the ATF device. In any overmoded waveguide system, bends are a critical element because of their mode conversion, power handling, and cost. Miter bends were chosen over corrugated waveguide bends because they are simple and relatively inexpensive to fabricate, their cooling and power handling are straightforward, and they can be made very efficient for the TE_{02} mode if the waveguide diameter is much greater than a free-space wavelength. Attenuation of unwanted (noncircular electric) modes is accomplished with TiO_2 coatings in absorber sections [84]. Finally, a "Vlasov-type" launcher [85] can convert the TE_{02} mode into a linearly polarized O-mode beam launch for fundamental ECH and into an X-mode beam launch for second harmonic ECH.

Neutral Beam Injection. The neutral beam injector is a modified version [55] of the system used on ISX-B [86]. The 30-cm-diam ORNL ion sources [87] deliver 100 A of hydrogenic ions at 40 kV with a beam divergence angle (HWHM) of $1.1^{o} \pm 0.1^{o}$. With a neutralization efficiency of 60%, the neutral power is 1.5 MW on a target subtending an angle of $\pm 2^{o}$ (28-cm-diam aperture at the beam focal length of 4 m). The beam species yield (power fraction) at the plasma is 75% 40-keV H^0 (from H^+), 15% 20-keV H^0 (from H_2^+), and 10% 13.3-keV H^0 (from H_3^+).

The modifications of the ISX-B neutral beam injector required for ATF are a new front end to adapt to the ATF outer port; an adjustable beam-defining aperture to minimize beam interception on the vacuum vessel wall, as discussed in Sec. III.F; and magnetic shielding of the neutralizer and the ion source, necessary due to the large stray field from the ATF. The $\int B\, d\ell$ along the 1.5-m-long neutralizing gas cell is 15 G•m for B = 2 T. If not corrected with magnetic shielding, the resulting deflection of 0.2^{o}/G•m for 40-keV H^{+} would be unacceptable. A 0.5-cm-thick iron sleeve will be placed around the neutralizer to attenuate the field by a factor of ~50. At the ion source plasma location (4.1 m from the ATF port), the 7-G field must be reduced to <1 G to maintain source plasma uniformity. A magnetic shield will also be used here. Calculations show that these magnetic shields, and other magnetic components (for example, beam bending magnets) in the beam line, have negligible effect on the ATF flux surfaces.

Ion Cyclotron Heating. Three HF-band transmitters (U.S. Navy type AN/FRT 86) will be used for steady-state ICH in the 5- to 30-MHz frequency range. Two of the units will operate as class AB amplifiers at 100 kW each, and the third has been converted for class C operation at 200 kW. The outputs of the two class AB transmitters will be combined to feed one antenna, and the class C amplifier will feed a second antenna. All three units will be driven by a single exciter with phase adjustment between the two antennas. Higher-power (1.5- to 2-MW), higher-frequency (40- to 80-MHz), pulsed (<30-s) ICH will be provided by a modified FMIT transmitter. The transmission line used is 15.6-cm-diam coaxial cable.

To meet design requirements, the ATF fast-wave antenna must (1) be close to the plasma surface (<5 cm away) and contoured to the last closed flux surface; (2) be movable radially over several centimeters to optimize coupling to the plasma while minimizing impurity generation; (3) have $\vec{B}_{RF}$ parallel to $\vec{B}$; (4) avoid regions of energetic or thermal ion drift orbits outside the plasma; and (5) be on |B| contours that do not penetrate deep into the plasma to avoid edge impurity heating. For fast-wave heating in large dense plasmas, control of the parallel wave number ($k_{\parallel}$) spectrum launched by the

antennas is useful for tailoring the ion heating profile. This will require two antennas spaced several tens of centimeters apart toroidally (in adjacent ports).

The ICH launchers themselves have some novel features [88]. The launchers have a resonant double loop configuration to improve the tuning, impedance matching, and power handling capabilities of the antennas. The Faraday shield is actively cooled and consists of two layers of graphite-coated tubes. A single 50-Ω rf vacuum feedthrough will be used for each antenna. The antennas are designed for 30 kV, typical for standard vacuum variable capacitors, and for 0.6 μH at 14.2 MHz (0.95-T H^+ resonance). The loading resistance required for 200-kW operation is 0.5 Ω.

The ATF fast-wave antenna is shaped to conform to the last closed flux surface at $\phi = 15^{\circ}$ and follows the plasma shape toroidally. The antennas will be installed in two adjacent outside ports and are radially movable to adjust the plasma-antenna separation and the resulting coupling. Antennas are oriented along the short diagonal of the outside ports to minimize the angle between the directions of the antenna $\vec{B}_{RF}$ and the device $\vec{B}$ for fast-wave launching.

VI. SUMMARY

The ATF has been developed to carry out a specific mission: to demonstrate the principles of high-beta, steady-state operation in a toroidal confinement device and to study the basic building blocks of toroidal confinement in a flexible experiment. The coil systems have been optimized to allow direct access to the second stability regime and to enable study of a wide range of magnetic configurations. The mechanical design provides for the necessary construction accuracy, heating access, and steady-state capability at 1 T.

The first phase of the ATF program will start in early 1987 with sufficient heating power to attain high parameters in pulsed (5-s) operation. If this phase is successful, the next phase will entail installation of steady-state heating, cooling, and pumping to demonstrate the maintenance of a clean, high-beta, high-temperature plasma in true steady-state operation.

ACKNOWLEDGMENTS

Contributors to the development of ATF include E. E. Bartlett, D. B. Batchelor, L. R. Baylor, R. D. Benson, D. E. Brashears, C. Bridgman, A. Y. Broverman, R. L. Brown, W. E. Bryan, W. D. Cain, J. L. Cantrell, B. A. Carreras, L. A. Charlton, K. K. Chipley, M. J. Cole, W. K. Cooper, D. L. Coppenger, R. A. Dory, P. H. Edmonds, O. C. Eldridge, A. C. England, J. W. Forseman, R. H. Fowler, W. A. Gabbard, L. Garcia, J. C. Glowienka, E. L. Halstead, J. H. Harris, T. C. Hender, G. H. Henkel, H. R. Hicks, S. P. Hirshman, D. J. Hoffman, J. A. Holmes, W. A. Houlberg, T. C. Jernigan, R. L. Johnson, L. M. Jordan, V. E. Lynch, J. F. Lyon, B. F. Masden, J. A. Mayhall, J. F. Monday, R. N. Morris, G. H. Neilson, B. E. Nelson, J. A. Rome, M. J. Saltmarsh, K-C. Shaing, J. Sheffield, W. D. Shipley, D. J. Taylor, C. K. Thomas, P. B. Thompson, L. M. Vinyard, J. E. Warwick, J. A. White, J. C. Whitson, D. E. Williamson, W. L. Wright, and R. B. Wysor.

The advice and encouragement of stellarator researchers from the Max-Planck Institut für Plasmaphysik (Garching, Federal Republic of Germany), Kyoto University Plasma Physics Laboratory (Japan), the Kharkov Physico-Technical Institute and the Moscow Institute of General Physics (U.S.S.R.), GA Technologies, Inc., Los Alamos National Laboratory, Massachusetts Institute of Technology, New York University, Princeton Plasma Physics Laboratory, and the University of Wisconsin are appreciated.

The support of the Office of Fusion Energy and the Oak Ridge Operations Office of the U.S. Department of Energy has been important to the success of this project.

It is a pleasure to acknowledge the help and encouragement of O. B. Morgan and M. W. Rosenthal of Oak Ridge National Laboratory.

REFERENCES

1. J. SHEFFIELD, "The Advanced Toroidal Facility," J. Vac. Sci. Technol. A 3, 1134 (1985).

2. C. GOURDON et al., "Configurations of the Stellarator Type with Mean Well and Shear," Proc. 3rd Int. Conf. on Plasma Physics and Cont. Nucl. Fusion Res., Novosibirsk, 1968, Vol. 1, p. 845, IAEA, Vienna (1969).

3. U. BROSSMAN, W. DOMMASCHK, F. HERRNEGGER, G. GRIEGER, et al., "Concept of an Advanced Stellarator," Proc. 9th Int. Conf. on Plasma Physics and Cont. Nucl. Fusion Res., Baltimore, 1982, Vol. 3, p. 141, IAEA, Vienna (1983).

4. J. SAPPER et al., "The Advanced Stellarator Wendelstein VII-AS," Proc. 12th Symp. on Fusion Technology, Jülich, Vol. 1, p. 161 (1982).

5. K. UO et al., "Engineering Aspects of Heliotron-E Facility," Hitachi Rev. 30, 153 (1981).

6. E. D. ANDRYUKHINA, G. M. BATANOV, M. S. BEREZHETSKIJ, M. A. BLOKH, et al., "First Results on Currentless Plasma Production and Heating by ECR Waves in the L-2 Stellarator," Proc. 10th Int. Conf. on Plasma Physics and Cont. Nucl. Fusion Res., London, 1984, Vol. 2, p. 409, IAEA, Vienna (1985).

7. W VII-A TEAM et al., "Recent Results on Plasma Behaviour in the W VII-A Stellarator," Plasma Phys. Controlled Fusion 26, 183 (1984).

8. V. V. BAKAEV, S. P. BONDARENKO, V. V. BRONNIKOV, V. S. VOITSENYA, et al., "Currentless Plasma Production and Heating in the Torsatron Uragan-3 by RF Waves," Proc. 10th Int. Conf. on Plasma Physics and Cont. Nucl. Fusion Res., London, 1984, Vol. 2, p. 397, IAEA, Vienna (1985).

9. "Application for Preferential Support PHASE I for TJ-II EXPERIMENT: Proposal for a Flexible Heliac Device," Junta de Energia Nuclear, Madrid, Spain, 1985.

10. R. H. FOWLER, J. A. ROME, and J. F. LYON, "Monte-Carlo Studies of Transport in Stellarators," Phys. Fluids 28, 338 (1985).

11. D. E. HASTINGS, W. A. HOULBERG, and K. C. SHAING, "The Ambipolar Electric Field in Stellarators," Nucl. Fusion 25, 445 (1985).

12. K. C. SHAING, "Stability of the Radial Electric Field in a Non-axisymmetric Torus," Phys. Fluids 27, 7 (1984).

13. P. B. THOMPSON, "The Advanced Toroidal Facility (ATF)," Fusion Technol. 8 (1), part 2A, 450-455 (1985).

14. R. L. JOHNSON, "The Advanced Toroidal Facility," Proc. 11th Symp. on Fusion Eng., Austin, 1985, IEEE, New York, in press (1986).

15. R. L. JOHNSON, O. B. ADAMS, T. C. JERNIGAN, B. E. NELSON, J. F. LYON, and P. B. THOMPSON, "Design of the Advanced Toroidal Facility (ATF-1)," Nucl. Technol./Fusion 4, 1296 (1983).

16. B. E. NELSON, W. D. CAIN, K. K. CHIPLEY, M. J. COLE, et al., "Design Description of the Advanced Toroidal Facility," Proc. 10th Symp. on Fusion Eng., Philadelphia, 1983, Vol. 2, p. 2097, IEEE, New York (1983).

17. J. L. JOHNSON, G. GRIEGER, D. J. LEES, M. S. RABINOVICH, J. L. SHOHET, and K. UO, "The Stellarator Program," IEEE Trans. Plasma Sci. 9, 142 (1981).

18. J. L. JOHNSON, "Recent Developments in Stellarator Physics," Nucl. Technol./Fusion 4, 1275 (1983).

19. J. D. CALLEN, "Plasma Confinement and Heating in Stellarators," Nucl. Fusion 25, 485 (1985).

20. G. GRIEGER, "Fourth International Stellarator Conference," Nucl. Fusion 23, 683 (1983).

21. E. D. ANDRYUKHINA and I. S. DANILKIN, "Fifth International Stellarator Workshop," Sov. J. Plasma Phys. 11, 444 (1985).

22. K. UO, A. IIYOSHI, T. OBIKI, O. MOTOJIMA, et al., "Neutral-Beam Injection Heating Experiment on Currentless Plasma in the Heliotron-E Device," Nucl. Fusion 24, 1551 (1984).

23. F. SANO, T. OBIKI, O. MOTOJIMA, A. SASAKI, et al., "Ion and Electron Energy Balance Calculations for Neutral-Beam-Heated Heliotron-E Plasmas," Nucl. Fusion 24, 1103 (1984).

24. O. MOTOJIMA, F. SANO, M. SATO, et al., "Studies of Currentless, High-Beta Plasma in the Heliotron-E Device," Nucl. Fusion 25, 1783 (1985).

25. S. SUDO, O. MOTOJIMA, M. SATO, H. ZUSHI, et al., "Pellet Injection Experiment on NBI Current-Free Plasmas in Heliotron-E," Nucl. Fusion 25, 94 (1985).

26. J. H. HARRIS, O. MOTOJIMA, H. KANEKO, S. BESSHOU, et al., "Magnetohydrodynamic Activity in High-Beta, Currentless Discharges in Heliotron-E," Phys. Rev. Lett. 53, 2242 (1985).

27. W VII-A TEAM and NI GROUP, "Plasma Confinement and the Effect of Rotational Transform in the Wendelstein VII-A Stellarator," Proc. 10th Int. Conf. on Plasma Physics and Cont. Nucl. Fusion Res., London, 1984, Vol. 2, p. 371, IAEA, Vienna (1985).

28. G. CATTANEI, D. DORST, A. ELSNER, G. GRIEGER, et al., "Neutral Injection Heating in the Wendelstein VII-A Stellarator," Proc. 9th Int. Conf. on Plasma Physics and Cont. Nucl. Fusion Res., Baltimore, 1982, Vol. 2, p. 241, IAEA, Vienna (1983).

29. J. F. LYON, B. A. CARRERAS, J. H. HARRIS, J. A. ROME, et al., "Stellarator Physics Evaluation Studies," Proc. 9th Int. Conf. on Plasma Phys. Controlled Nucl. Fusion Res., Baltimore, 1982, Vol. 3, p. 115, IAEA, Vienna (1983).

30. L. M. KOVRIZHNYKH and S. V. SHCHEPETOV, "MHD Equilibrium and Stability of Stellarator Plasma," Nucl. Fusion 23, 859 (1983).

31. G. REWOLDT and J. L. JOHNSON, "MHD Kink-Driven Instabilities in Net-Current-Free Stellarators," Nucl. Fusion 24, 733 (1984).

32. O. B. ADAMS et al., "Proposal to Build ATF-1, an Advanced Toroidal Facility," Oak Ridge National Laboratory (unpublished).

33. B. A. CARRERAS, H. R. HICKS, J. A. HOLMES, V. E. LYNCH, et al., "Equilibrium and Stability Properties of High-Beta Torsatrons," Phys. Fluids 26, 3569 (1983).

34. L. GARCIA, B. A. CARRERAS, J. H. HARRIS, H. R. HICKS, and V. E. LYNCH, "Equilibrium Studies for Low-Aspect-Ratio Torsatrons," Nucl. Fusion 24, 115 (1984).

35. B. A. CARRERAS, H. R. HICKS, J. A. HOLMES, V. E. LYNCH, and G. H. NEILSON, "Zero-Current High-Beta Stellarator Equilibria with Rotational Transform Profile Control," Nucl. Fusion 24, 1347 (1984).

36. T. C. HENDER and B. A. CARRERAS, "Equilibrium Calculations for Helical Axis Stellarators," Phys. Fluids 27, 2101 (1984).

37. B. A. CARRERAS, J. L. CANTRELL, L. A. CHARLTON, et al., "MHD Equilibrium and Stability for Stellarator/Torsatron Configurations," Proc. 10th Int. Conf. on Plasma Physics and Cont. Nucl. Fusion Res., London, 1984, Vol. 2, p. 31, IAEA, Vienna (1985).

38. T. C. HENDER, B. A. CARRERAS, L. A. CHARLTON, L. GARCIA, et al., "Torsatron Equilibrium and Stability Studies," Oak Ridge National Laboratory Report No. ORNL/TM-9587 (1985).

39. V. E. LYNCH et al., "Stellarator Expansion Methods for MHD Equilibrium and Stability Calculations," submitted to J. Comput. Phys.; also, Oak Ridge National Laboratory Report No. ORNL/TM-9861 (1985).

40. T. C. HENDER et al., "The Calculation of Stellarator Equilibria in Vacuum Flux Surface Coordinates," J. Comput. Phys. 60, 76 (1985).

41. K. MIYAMOTO, "Recent Stellarator Research," Nucl. Fusion 18, 243 (1978).

42. J. F. LYON, J. A. ROME, and V. E. LYNCH, "Particles and Field Lines Outside the ATF Plasma," J. Nucl. Mater. 121, 415 (1984).

43. L. M. KOVRIZHNYKH, "Neoclassical Theory of Transport Processes in Toroidal Magnetic Confinement Systems, with Emphasis on Non-Axisymmetric Configurations," Nucl. Fusion 24, 851 (1984).

44. L. M. KOVRIZHNYKH, "The Energy Confinement Time in Stellarators," Nucl. Fusion 24, 435 (1984).

45. H. E. MYNICK and W. N. G. HITCHON, "Effect of the Ambipolar Potential on Stellarator Confinement," Nucl. Fusion 23, 1053 (1983).

46. F. L. HINTON and R. D. HAZELTINE, "Theory of Plasma Transport in Toroidal Confinement Systems," Rev. Mod. Phys. 48, 239 (1976).

47. W. N. G. HITCHON, C. D. BEIDLER, H. E. MYNICK, and J. L. SHOHET, "Bounce-Average Monte-Carlo Calculation of Ripple Transport in Stellarators," Nucl. Fusion 25, 105 (1985).

48. H. WOBIG, "Numerical Evaluation of Neoclassical Transport in Stellarators at Arbitrary Collisionality," Z. Naturforsch. 37a, 906 (1982).

49. H. E. MYNICK and W. N. G. HITCHON, "A Bounce Average Fokker-Planck Code for Stellarator Transport," Princeton Plasma Physics Laboratory Report No. PPPL-2235 (1985).

50. H. MAASSBERG, W VII-A TEAM, NI TEAM, and ECRH GROUP, "Ambipolar Electric Fields and Transport," Proc. 12th Eur. Conf. on Cont. Fusion and Plasma Phys., Budapest, 1985, Vol. 9F, part 1, p. 389, European Phys. Soc. (1985).

51. A. CARNEVALI, J. MISIUM, et al., "Heavy Ion Beam Probe Diagnostic System for ATF-1," Bull. Am. Phys. Soc. 30, 1419 (1985).

52. H. C. HOWE, Oak Ridge National Laboratory, private communication, 1985.

53. A. IIYOSHI, O. MOTOJIMA, M. SATO, T. MUTOH, et al., "RF Heating of Currentless Plasmas in Heliotron-E," Proc. 10th Int. Conf. on Plasma Physics and Cont. Nucl. Fusion Res., London, 1984, Vol. 1, p. 453, IAEA, Vienna (1985).

54. V. ERCKMANN, G. JANZEN, W. KASPAREK, G. A. MULLER, et al., "70 GHz Experiments on the W-VIIA Stellarator," Proc. 12th Eur. Conf. on Cont. Fusion and Plasma Phys., Budapest, 1985, Vol. 9F, part 1, p. 385, European Phys. Soc. (1985).

55. M. M. MENON et al., "ATF Neutral Beam Injection System," Proc. 11th Symp. on Fusion Eng., Austin, 1985, IEEE, New York, in press (1986).

56. T. MUTOH, H. OKADA, O. MOTOJIMA, S. MORIMOTO, et al., "ICRF Heating of Currentless Plasma in Heliotron-E," Nucl. Fusion 24, 1003 (1984).

57. V. A. BATYUK, M. A. BLOKH, S. E. GREBENSHCHIKOV, I. A. KOVAN, et al., "Heating of Hydrogen Plasma on the First Harmonic of the Ion Cyclotron Frequency," Proc. 11th Eur. Conf. on Cont. Fusion and Plasma Phys., Aachen, 1983, Vol. 7D, part 1, p. 373, European Phys. Soc. (1983).

58. M. ONO et al., "Ion Bernstein Wave Excitation via Finite-Larmor-Radius Mode-Transformation Process," Princeton Plasma Physics Laboratory Report No. PPPL-1819 (1981).

59. W VII-A TEAM and NI GROUP, "Impurity Transport in the Wendelstein VII-A Stellarator," Nucl. Fusion 25, 1593 (1985).

60. K. K. CHIPLEY, B. E. NELSON, L. M. VINYARD, and D. F. WILLIAMSON, "Design Description of the Vacuum Vessel for the Advanced Toroidal Facility," Proc. 10th Symp. on Fusion Eng., Philadelphia, 1983, Vol. 2, p. 993, IEEE, New York (1983).

61. R. N. MORRIS, R. H. FOWLER, J. A. ROME, and T. J. SCHLAGEL, "ATF Neutral Beam Injection: Optimization of Beam Alignment and Aperturing," Oak Ridge National Laboratory Report No. ORNL/TM-9689 (1985).

62. O. MOTOJIMA, T. MIZUUCHI, S. BESSHOU, et al., "Analysis of the Plasma-Wall Interaction in the Heliotron-E Device," J. Nucl. Mater. 128, 524 (1984).

63. P. MIODUSZEWSKI et al., "Particle Removal with Pump Limiters in ISX-B," J. Nucl. Mater. 121, 285 (1984).

64. M. J. COLE, B. E. NELSON, R. L. JOHNSON, and P. B. THOMPSON, "Design Description of the Helical Field Coils for the Advanced Toroidal Facility," Proc. 10th Symp. on Fusion Eng., Philadelphia, 1983, Vol. 1, p. 876, IEEE, New York (1983).

65. D. J. TAYLOR et al., "Helical Coil Alignment in the Advanced Toroidal Facility," Proc. 11th Symp. on Fusion Eng., Austin, 1985, IEEE, New York, in press (1986).

66. R. D. BENSON, "Highlights from the Assembly of the Helical Field Coils for the Advanced Toroidal Facility," Proc. 11th Symp. on Fusion Eng., Austin, 1985, IEEE, New York, in press (1986).

67. Advance Engineering Plastics Company, Freehold, New Jersey.

68. B. E. NELSON et al., "Mechanical Testing and Development of the Helical Field Coil Joint for the Advanced Toroidal Facility," Proc. 11th Symp. on Fusion Eng., Austin, 1985, IEEE, New York, in press (1986).

69. R. L. BROWN and R. L. JOHNSON, "Thermal and Electrical Joint Test for the Helical Field Coils in the Advanced Toroidal Facility," Proc. 11th Symp. on Fusion Eng., Austin, 1985, IEEE, New York, in press (1986).

70. J. H. CHRZANOWSKI et al., "Coil Design and Manufacturing of the ATF Vertical Field Coils," Proc. 11th Symp. on Fusion Eng., Austin, 1985, IEEE, New York, in press (1986).

71. K. K. CHIPLEY and G. N. FREY, "Design and Fabrication of the Vacuum Vessel for the Advanced Toroidal Facility," Proc. 11th Symp. on Fusion Eng., Austin, 1985, IEEE, New York, in press (1986).

72. PATRAN, computer code from PDA Engineering, Santa Ana, Calif.

73. MSC/NASTRAN, computer code from MacNeal-Schwendler Corp., Los Angeles, Calif.

74. J. A. MOORE, BARC computer code, Oak Ridge National Laboratory, Oak Ridge, Tennessee.

75. W. D. CAIN, "MAGFOR: A Magnetics Code to Calculate Fields and Forces in Twisted Helical Coils of Constant Cross Section," Proc. 10th Symp. on Fusion Eng., Philadelphia, 1983, Vol. 2, p. 1223, IEEE, New York (1983).

76. Instruction Manual for the Cordax Coordinate Measuring System, Sheffield Instruments, Inc., Dayton, Ohio (1982).

77. Operator's Manual for Informatic Theodolite Theomat Wild T2000, Wild-Heerbrug, Ltd., Heerbrug, Switzerland (1984).

78. J. A. ROME, J. H. HARRIS, G. H. NEILSON, and T. C. JERNIGAN, "A Novel Method of Aligning ATF-1 Coils," Oak Ridge National Laboratory Report No. ORNL/TM-8496 (1983).

79. R. J. COLCHIN et al., "Magnetic Field Alignment Studies for the URAGAN-3 Torsatron," Oak Ridge National Laboratory Report No. ORNL/TM-9685 (1986).

80. J. C. WHITSON, Oak Ridge National Laboratory, private communication.

81. R. D. FOSKETT, P. H. EDMONDS, and G. H. NEILSON, "Facility Design and Preparation for ATF," Proc. 11th Symp. on Fusion Eng., Austin, 1985, IEEE, New York, in press (1986).

82. "Fusion Energy Division Annual Progress Report for Period Ending December 31, 1982," Oak Ridge National Laboratory Report No. ORNL-5919 (1982), Chap. 2; "Fusion Energy Division Annual Progress Report for Period Ending December 31, 1983," Oak Ridge National Laboratory Report No. ORNL-6015 (1984), Chap. 2.

83. H. D. KIMREY, T. L. WHITE, and T. S. BIGELOW, "ATF ECH System Status," paper presented at the U.S.-Japan Heliotron-Stellarator Workshop, Oak Ridge, Tenn., 1985.

84. T. L. WHITE, H. D. KIMREY, and T. S. BIGELOW, "Mixed-Mode Distribution Systems for High Average Power Electron Cyclotron Heating," Heating in Toroidal Plasmas: Proceedings of the Fourth International Symposium, Rome, March 1984, Vol. II, p. 1444, International School of Plasma Physics and ENEA, Varenna, Italy (1984).

85. S. N. VLASOV and I. M. ORLOVA, "Quasioptical Transformer Which Transforms the Waves in a Waveguide Having a Circular Cross Section into a Highly Directional Wave Beam," Izv. Vyssh. Uchebn. Zaved. Radiofiz. 17, 148 (1974) [Radiophys. Quantum Electron. 17, 115 (1975)].

86. S. C. BATES, P. H. EDMONDS, et al., "ISX-B Neutral Beams and the Beam Target Experiment," Oak Ridge National Laboratory Report No. ORNL/TM-7452 (1980).

87. W. L. GARDNER et al., "Properties of an Intense 50-kV Neutral Beam Injection System," Rev. Sci. Instrum. 53, 424 (1982).

88. F. W. BAITY, D. J. HOFFMAN, and T. L. OWENS, "ICRF Heating on ATF," in Radiofrequency Plasma Heating, AIP Conf. Proc. 129, 32 (1985).

Appendix

OPTIMIZATION PROCEDURE AND RESULTS

Selection of a specific magnetic configuration for ATF proceeded in two stages: first, evaluation of a number of possible stellarator geometries covering a wide range of configuration parameters, and second, optimization of the most promising type of configuration, once the parameter range had been restricted. The large number of attractive stellarator configurations did not permit an exhaustive optimization procedure, and other (facility-dependent) factors were allowed to enter into the final selection.

A broad set of computational tools was used in the assessment and optimization process: (1) 3-D vacuum magnetic field calculations; (2) 2-D and 3-D MHD equilibrium and stability codes; (3) 3-D guiding center particle orbit codes and 1-D transport codes; and (4) engineering design codes. All magnetic fields used in these calculations were derived from realistic coil models rather than from simplified analytic model field expressions. Since developing an optimal configuration required balancing different magnetic field properties that have nonorthogonal effects on physics performance and engineering practicality, an iterative approach was used to assess configurations, as illustrated in Fig. A.1. The linked assessment loops indicate the connections between the information generated in the different evaluation procedures. The criteria used for the overall assessment are discussed in Sec. II.B.

Loop (a) in Fig. A.1, the calculation of the vacuum magnetic field properties, was the most frequent iteration step because of its speed and because it made it possible to recognize the potential of a candidate configuration from the size and shape of the magnetic surfaces, from the $\iota(r)$ profile (particularly the rational ι locations and the value of the shear), from $V'(r)$ and hence the magnetic well or hill value, and from the variation ΔQ of $\oint d\ell/B$ on a flux surface.

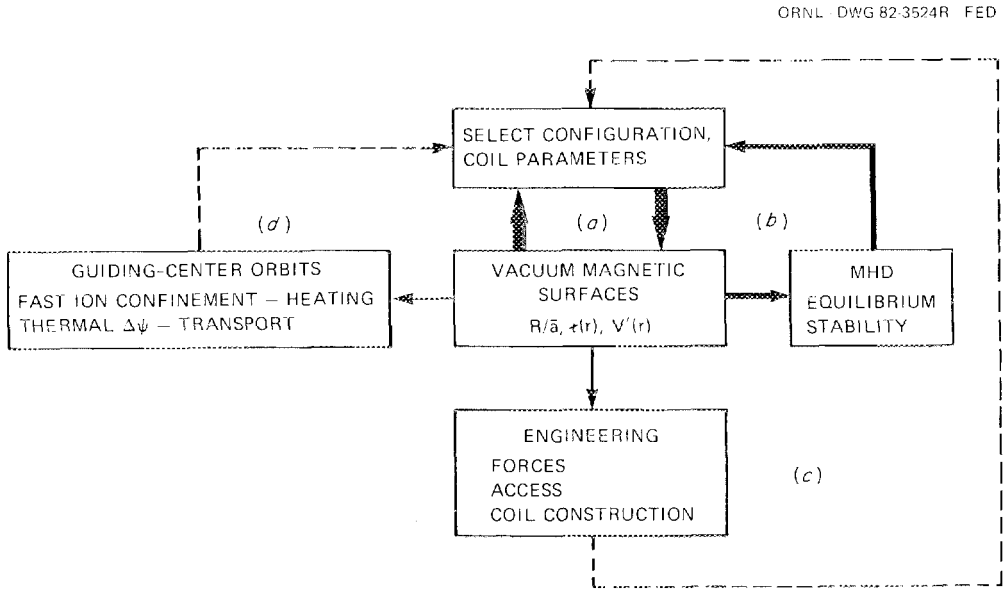

Fig. A.1. Configuration assessment process. The thickness of the arrows indicates the importance of the loop.

Magnetic field lines were calculated from the Biot-Savart law and were followed toroidally for ~20 transits on each of typically 10 flux surfaces to characterize the magnetic configuration in both space and flux coordinates [1]. Coils were usually represented by single filaments (288 elements for the $\ell = 2$, $M = 12$ torsatron). Multiple filaments (up to 56, but usually ~6) were used only where it was necessary to have a more accurate magnetic field calculation, for instance near the HF coils.

The MHD assessment process, loop (b) in Fig. A.1, played a dominant role in finding an optimum configuration within a given class, since the MHD studies were the most sensitive to variations in the vacuum field structure. The objective of these studies was to determine the MHD equilibrium and stability limits to the plasma beta for a given plasma pressure profile. The MHD equilibrium and stability codes [2-13] listed in Table A.I are fully 3-D or equivalent 2-D (averaged method [14] or stellarator expansion [15]), are free boundary or fixed boundary, and are flux-conserving or have zero net current on a flux surface. The calculated quantities used in the assessments include the major axis shift, the magnetic well depth, the degree of magnetic surface breakup, the linear growth rate (if unstable), the free energy, and the Mercier criterion. Figure A.2 indicates the relationships of the various MHD equilibrium and stability calculations and their use for study of low-n modes, high-n modes, ballooning modes, etc.

The guiding center orbit calculations (collisionless and Monte Carlo), loop (d) in Fig. A.1, were used primarily to filter out magnetic configurations with unacceptably large vacuum orbit losses. The calculated quantities used in these assessments included the deviations from an average flux surface for contained particles, the mean loss time for lost particles, the weighted loss fraction, and the particle diffusion coefficient D. These calculations show that the ambipolar electric field has a much larger effect on confinement improvement than small differences in the magnetic configuration [16], as illustrated in Fig. 26. The WHIST 1-D transport code was used to evaluate the ATF performance for various transport models, heating

TABLE A.I

MHD Equilibrium and Stability Codes Used for ATF Analysis

	DIMENSIONS	NAME	METHOD	NUMERICAL APPROACH	BOUNDARY CONDITION
EQUILIBRIUM CODES	3-D	CHODURA-SCHLÜTER [2]	Energy Minimization Eulerian	Conjugate Gradient	Fixed Boundary Away From Plasma
		BETA [3]	Energy Minimization Lagrangian	Accelerated Iteration	Fixed and Free Boundary
		NEAR [4]	Energy Minimization Eulerian	Conjugate Gradient	Fixed Boundary
		MOMCOM [5]	Energy Minimization Lagrangian	Steepest Descendent	Fixed Boundary
	2-D (Stellarator Expansion)	RSTEQ [6,7]	Grad-Shafranov Equation	S.O.R.	Fixed Boundary
		PPLEQ [8,9]	Grad-Shafranov Equation	Fast Fourier	Free Boundary
		NAV [6,10]	Generalized Grad-Shafranov Equation	Conjugate Gradient	Fixed Boundary
STABILITY CODES	2-D (Stellarator Expansion)	RST [11]	Reduced MHD Equations	Initial Value Semi-Implicit Spectral	Fixed Boundary
		FAR [6,12]	Full MHD Equations	Fully Implicit Spectral	Fixed Boundary
		PEST [13]	Energy Principle		Free Boundary
	3-D	BETA [3]	δW Minimization	Acceleration Iteration	Fixed Boundary

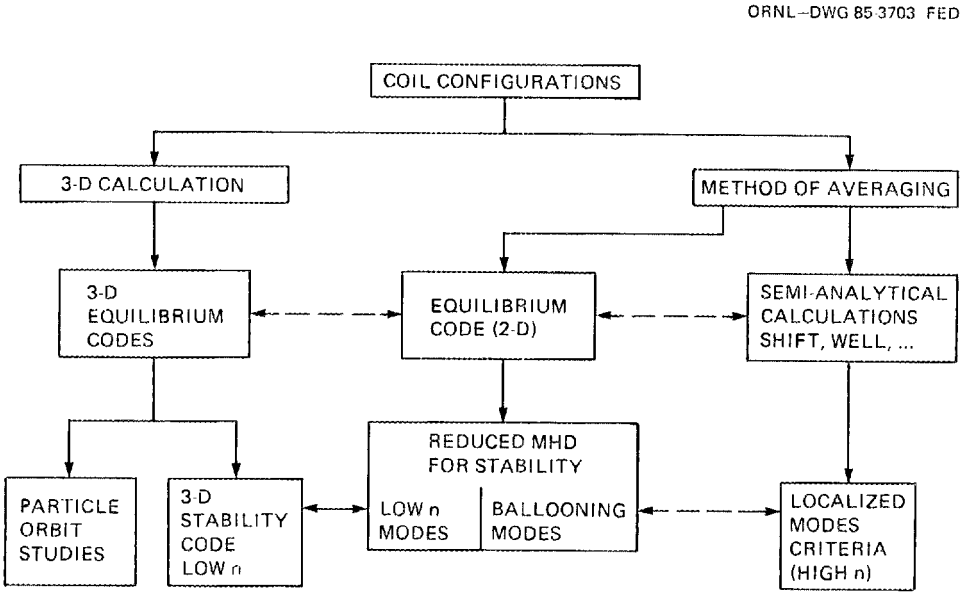

Fig. A.2. Relationship of MHD codes used in the equilibrium and stability assessments.

profiles, and assumptions about the electric field. The relationships of the different calculations are shown in Fig. A.3. Other codes were used to study neutral beam deposition and wall losses [17, 18].

These MHD and transport calculations were performed using both spatial and flux coordinates. Flux, or field line, coordinates [1] were very useful because they allowed study of the various components (spatial harmonics) of the magnetic field, an increase of an order of magnitude in computational speed, a more physical separation of motion about a flux surface from the complex 3-D spatial field line geometry, and inclusion of radial electric fields (assuming constant potential on a flux surface).

The engineering assessment, loop (c) in Fig. A.1, was used primarily to indicate when candidate coil configurations had overlapping conductors, extreme forces, coil bend radii that were too small, or inadequate access for tangential NBI. This was particularly important for the more complicated modular stellarator and Symmotron coil configurations. A full complement of engineering design codes [19-29], listed in Table A.II, was used in the final design of the ATF.

The types of stellarator geometries examined for ATF are shown in Fig. A.4, and the ranges of parameters explored are listed in Table A.III. Continuous-coil torsatrons, shown in Fig. A.4(a), use helical windings to create the main toroidal and poloidal fields and circular (VF) coils for plasma positioning and shaping. Torsatrons with $\ell = 2$ gave the best combination of plasma size, shear, and central transform. The helical coil winding law for the $\ell = 2$ torsatrons had the form $\phi = (\ell/M)(\theta - \alpha \sin \theta)$, where ϕ is the toroidal angle, θ is the poloidal angle, α is the winding modulation ($-1 < \alpha < 1$), and M is the number of toroidal field periods. Although windings on tori with noncircular cross sections and $\alpha \neq 0$ cases were examined, these cases were no better than those obtained with a circular cross section and $\alpha = 0$.

Modular torsatron configurations of the Symmotron type [30,31], developed at ORNL during the ATF configuration search, were also studied. This configuration, shown in Fig. A.4(b), uses identical,

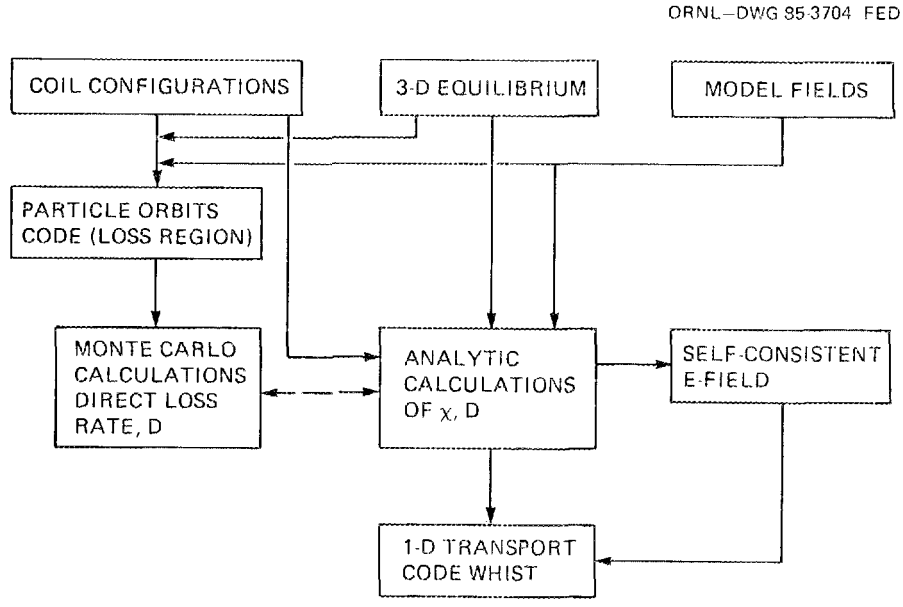

Fig. A.3. Relationship of codes used in the orbit and transport assessments.

TABLE A.II

Engineering Design Codes

Computer code	Purpose
	Mechanical Design
MOVIE.BYU [19]	3-D plots of coil and vacuum vessel geometry.
CADAM [20]	Computer-aided drafting of ATF components.
	Fields and Forces
BARC [21]	Calculate magnetic fields and forces from filaments and/or finite cross section segments.
MAGFOR [22]	Calculate magnetic fields and forces for coils of arbitrary geometry, including twisted, nonplanar coils from 20-node isoparametric brick elements.
EFFI [23]	Calculate magnetic fields, forces, and coil inductances from filaments and/or finite cross section segments.
	Vacuumm Vessel
ANSYS [24]	Finite element analysis code, used by PDM to generate flat developments of vacuum vessel skin from 3-D geometry data.
	Thermal Analysis
KCOL3 [25]	PPPL code to calculate thermal behavior of VF coils.
HEATING6 [26]	Finite-difference thermal analysis of vacuum vessel.
	Stress Analysis
PAFEC [27]	Finite element stress analysis of vacuum vessel and thermal analysis of HF coil.
MSC/NASTRAN [28]	Multipurpose finite element analysis, including stress, thermal, and buckling solutions. Used for vacuum vessel, coils, and structure.
PATRAN [29]	Solid modeling of coils and vacuum vessel. Used as a pre- and post-processor for MSC/NASTRAN.

(a) TORSATRON

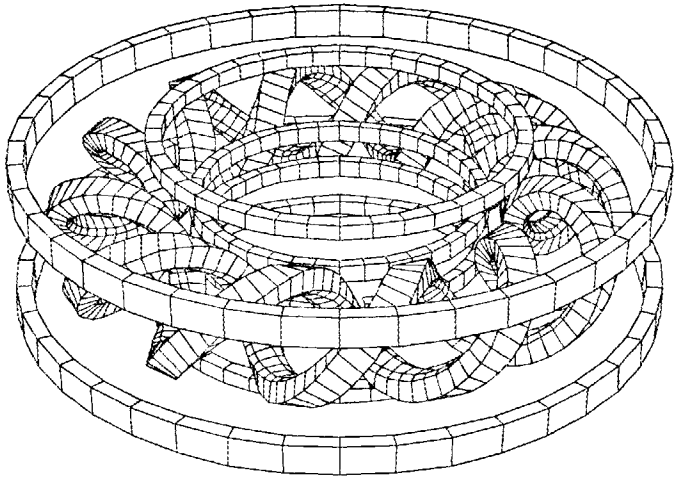

(b) SYMMOTRON

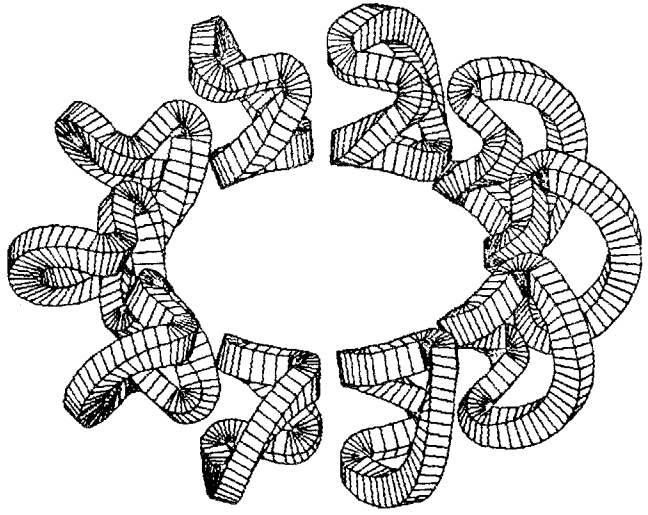

(c) MODULAR STELLARATOR

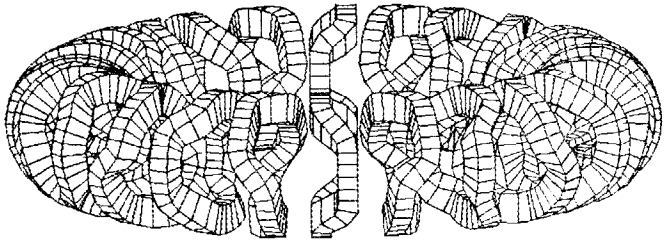

(d) HELIAC

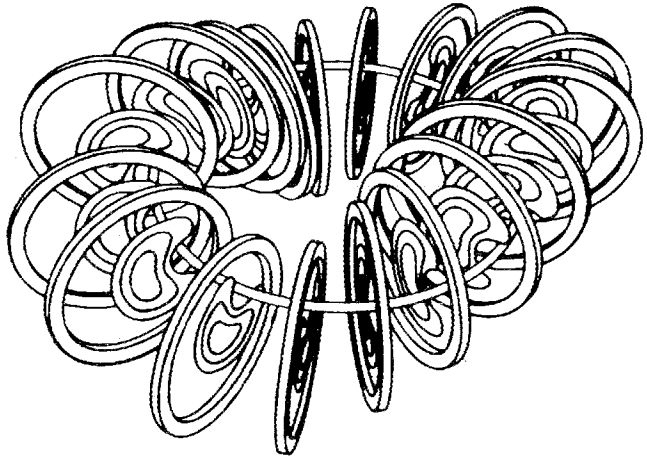

Fig. A.4. Examples of configurations examined in the ATF studies: (a) torsatron, (b) Symmotron, (c) modular stellarator, and (d) heliac.

TABLE A.III

Configurations Evaluated in ATF Studies

	ℓ	M	R/a_c	$\iota(\bar{a})$	Shear
$\ell = 3$ Torsatron	3	8–10	3–5	0.8	~0.8
$\ell = 2$ Torsatron	2	6–24	2.5–10	0.5–2	~1.0
$\ell = 2$ Symmotron	2	10–21	4–9	0.8–1.5	~0.5
$\ell = 1$ Symmotron	1	13	5	0.7	$\leq$0.3
Modular Stellarator	2	3–6	3–6	0.3–0.6	$\leq$0.3
Heliac	1	2–8	2–8	0.8–4.0	$\leq$0.2

nonrotated, helically deformed coils, one per field period. The helical segments are connected by toroidally directed windbacks (the stray field of which must be compensated by adjacent toroidal ring coils), which also provide part of the vertical field needed for positioning the plasma. These configurations retained the good physics properties of the continuous-coil torsatrons but had slightly smaller average plasma radii and less configuration flexibility.

Modular stellarator configurations, similar to that illustrated in Fig. A.4(c), were also assessed as candidate ATF configurations. These configurations [32,33] employ a set of toroidally distorted TF coils to create an $\ell = 2$ stellarator configuration. The TF coil set studied consisted of identical, sinusoidally distorted TF coils that were rotated poloidally with respect to each other in a field period. Modular stellarator configurations examined for ATF all had low shear and low beta limits, and none was an improvement over that proposed for Wendelstein VII-AS.

The heliac (a helical-axis stellarator) coil configuration [34,35], shown in Fig. A.4(d), was also examined as an ATF candidate. This magnetic configuration has high ι (>1) and the potential for high-beta operation [36,37], at least for large aspect ratio, but may have problems with flux surface breakup at low beta (<1%) and finite aspect ratio due to its low shear and high transform per field period ($\iota/M \gtrsim 0.3$ vs $\iota/M \lesssim 0.1$ for planar-axis stellarators). This makes it very sensitive to resonant effects at rational transform values [38,39]. This magnetic geometry was thought to have too little configuration flexibility and to be too high a risk for the only large U.S. stellarator experiment. This deficiency has since been remedied by the development of the flexible heliac concept [40], which will be tested in the TJ-II experiment to be built in Spain [41,42].

REFERENCES

1. G. KUO-PETRAVIC, A. H. BOOZER, J. A. ROME, and R. H. FOWLER, "Numerical Evaluation of Magnetic Co-ordinates for Particle Transport Studies in Asymmetric Plasmas," J. Comput. Phys. 51, 261 (1983).

2. R. CHODURA and A. SCHLÜTER, "A 3D Code for MHD Equilibrium and Stability," J. Comput. Phys. 41, 68 (1981).

3. F. BAUER, O. BETANCOURT, and P. GARABEDIAN, Magnetohydrodynamic Equilibrium and Stability of Stellarators, Springer-Verlag, New York (1984).

4. T. C. HENDER et al., "The Calculation of Stellarator Equilibria in Vacuum Flux Surface Coordinates," J. Comput. Phys. 60, 76 (1985).

5. S. P. HIRSHMAN and J. C. WHITSON, "A Steepest-Descent Moment Method for Three-Dimensional Magnetohydrodynamic Equilibria," Phys. Fluids 26, 3553 (1983).

6. V. E. LYNCH et al., "Stellarator Expansion Methods for MHD Equilibrium and Stability Calculations," submitted to J. Comput. Phys.; also, Oak Ridge National Laboratory Report No. ORNL/TM-9861 (1985).

7. J. A. HOLMES, Y-K. M. PENG, and S. J. LYNCH, "Evolution of Flux-Conserving Tokamak Equilibria with Preprogrammed Cross Sections," J. Comput. Phys. 36, 35 (1980).

8. J. L. JOHNSON et al., "Numerical Determination of Axisymmetric Toroidal Magnetohydrodynamic Equilibria," J. Comput. Phys. 32, 212 (1979).

9. G. ANANIA and J. L. JOHNSON, "Application of the Stellarator Expansion for Plasma Stability Studies in Stellarators," Phys. Fluids 26, 3070 (1983).

10. T. C. HENDER and B. A. CARRERAS, "Equilibrium Calculations for Helical Axis Stellarators," Phys. Fluids 27, 2101 (1984).

11. V. E. LYNCH et al., "Resistive MHD Studies of High β Tokamak Plasmas," Comput. Phys. Commun. 24, 465 (1981).

12. L. A. CHARLTON et al., "Numerical Calculations Using the Full MHD Equations in Toroidal Geometry," J. Comput. Phys., accepted for publication (1986).

13. R. C. GRIMM, J. M. GREENE, and J. L. JOHNSON, "Computation of the Magnetohydrodynamic Spectrum in Axisymmetric Toroidal Confinement Systems," in Methods in Computational Physics, Vol. 16, p. 253, Academic Press, New York (1976).

14. L. M. KOVRIZHNYKH and S. V. SHCHEPETOV, "Description of a Stellarator Plasma with Averaged MHD Equations," Sov. J. Plasma Phys. 6, 533 (1981).

15. J. M. GREENE and J. L. JOHNSON "Determination of Hydromagnetic Equilibria," Phys. Fluids 4, 875 (1961).

16. R. H. FOWLER, J. A. ROME, and J. F. LYON, "Monte-Carlo Studies of Transport in Stellarators," Phys. Fluids 28, 338 (1985).

17. R. N. MORRIS, R. H. FOWLER, J. A. ROME, and T. J. SCHLAGEL, "ATF Neutral Beam Injection: Optimization of Beam Alignment and Aperturing," Oak Ridge National Laboratory Report No. ORNL/TM-9689 (1985).

18. S. A. HOKIN, J. A. ROME, T. C. HENDER, and R. H. FOWLER, "Neutral Beam Heating in Stellarators: A Numerical Approach," Oak Ridge National Laboratory Report No. ORNL/TM-8530 (1983).

19. BRIGHAM YOUNG UNIVERSITY, MOVIE.BYU (A General Purpose Computer Graphics System), Version 3.3, January 1980.

20. CADAM INC., Lockheed Corp., Burbank, Calif.

21. J. A. MOORE, BARC computer code, Oak Ridge National Laboratory, Oak Ridge, Tennessee.

22. W. D. CAIN, "MAGFOR: A Magnetic Code to Calculate Fields and Forces in Twisted Helical Coils of Constant Cross Section," Proc. 10th Symp. Fusion Eng., Philadelphia, 1983, Vol. 2, p. 1223, IEEE, New York (1983).

23. S. J. SACKETT, "EFFI - A Code for Calculating the Electromagnetic Field, Force and Inductance in Coil Systems of Arbitrary Geometry," Lawrence Livermore Laboratory Report No. UCID-17621 (1977).

24. G. J. DESALVO and J. A. SWANSON, "ANSYS, Engineering Analysis System User's Manual, Vol. II," Swanson Analysis Systems, Inc., Houston, Penn.

25. KCOL3, computer code from Coil Design Section, Princeton Plasma Physics Laboratory, Princeton, New Jersey.

26. D. C. ELROD, G. E. GILES, and W. D. TURNER, "HEATING6: A Multi-dimensional Heat Conduction Analysis with the Finite-Difference Formulation," Vol. 2, Sec. F10, Oak Ridge National Laboratory Report No. ORNL/NUREG/CSD-2/V2.

27. PAFEC Ltd., Strellev Hall, Strellev, Nottingham NG86PE, England.

28. MSC/NASTRAN, computer code from MacNeal-Schwendler Corp., Los Angeles, Calif.

29. PATRAN, computer code from PDA Engineering, Santa Ana, Calif.

30. L. GARCIA, B. A. CARRERAS, J. H. HARRIS, H. R. HICKS, and V. E. LYNCH, "Equilibrium Studies for Low-Aspect-Ratio Torsatrons," Nucl. Fusion 24, 115 (1984).

31. J. A. ROME and J. H. HARRIS, "Symmetric Modular Torsatron," patent applied for by U.S. Department of Energy.

32. T. K. CHU, H. P. FURTH, J. L. JOHNSON, C. LUDESCHER, and K. E. WEIMER, "Optimization Techniques for Modular Stellarator Coils," Nucl. Fusion 22, 871 (1982).

33. T. K. CHU, H. P. FURTH, J. L. JOHNSON, C. LUDESCHER, and K. E. WEIMER, "Modular Coils: A Promising Toroidal Coil System," IEEE Trans. Plasma Sci. 9, 234 (1981).

34. A. H. BOOZER, T. K. CHU, R. L. DEWAR, H. P. FURTH, et al., "Two High-Beta Toroidal Configurations: a Stellarator and a Tokamak-Torsatron Hybrid," Proc. 9th Int. Conf. on Plasma Physics and Cont. Nucl. Fusion Res., Baltimore, 1982, Vol. 3, p. 129, IAEA, Vienna (1983).

35. S. YOSHIKAWA, "Design of a Helical-Axis Stellarator," Nucl. Fusion 23, 667 (1983).

36. P. MERKEL, J. NÜHRENBERG, R. GRUBER, and F. TROYON, "Linear MHD Stability Studies of Helically Symmetric Equilibria with HERA," Nucl. Fusion 23, 1061 (1983).

37. D. A. MONTICELLO, R. L. DEWAR, H. P. FURTH, and A. REIMAN, "Heliac Parameter Study," Phys. Fluids 27, 1248 (1984).

38. B. A. CARRERAS, J. L. CANTRELL, L. A. CHARLTON, et al., "MHD Equilibrium and Stability for Stellarator/Torsatron Configurations," Proc. 10th Int. Conf. on Plasma Physics and Cont. Nucl. Fusion Res., London, 1984, Vol. 2, p. 31, IAEA, Vienna (1985).

39. A. REIMAN and A. H. BOOZER, "Island Formation and Destruction of Flux Surfaces in Three-Dimensional MHD Equilibria," Phys. Fluids 27, 2446 (1984).

40. J. H. HARRIS, J. L. CANTRELL, T. C. HENDER, B. A. CARRERAS, and R. N. MORRIS, "A Flexible Heliac Configuration," Nucl. Fusion 25, 623 (1985).

41. A. PEREA, J. L. ALVAREZ-RIVAS, J. BOTIJA, J. R. CEPERO, et al., "Physics Issues in the Design of TJ-II," Proc. 12th Eur. Conf. on Cont. Fusion and Plasma Phys., Budapest, 1985, Vol. 9F, part 1, p. 433, European Phys. Soc. (1985).

42. J. GUASP, J. L. ALVAREZ-RIVAS, J. A. FABREGAS, J. A. LOPEZ-FRAGUAS, et al., "Physics Studies for the TJ-II Device," Proc. 12th Eur. Conf. on Cont. Fusion and Plasma Phys., Budapest, 1985, Vol. 9F, part 1, p. 441, European Phys. Soc. (1985).

ORNL/TM-9831
Dist. Category UC-20

INTERNAL DISTRIBUTION

1. R. D. Benson
2. L. A. Berry
3. R. L. Brown
4–8. B. A. Carreras
9. K. K. Chipley
10. R. J. Colchin
11. M. J. Cole
12. R. A. Dory
13. J. L. Dunlap
14. P. H. Edmonds
15. J. H. Harris
16. H. H. Haselton
17. T. C. Jernigan
18. O. V. Jett
19. R. L. Johnson
20. M. S. Lubell
21. V. E. Lynch
22–26. J. F. Lyon
27. P. K. Mioduszewski
28. M. Murakami
29. G. H. Neilson
30. B. E. Nelson
31. J. A. Rome
32. M. J. Saltmarsh
33. J. Sheffield
34. P. B. Thompson
35. J. C. Whitson
36–37. Laboratory Records Department
38. Laboratory Records, ORNL-RC
39. Document Reference Section
40. Central Research Library
41. Fusion Energy Division Library
42–43. Fusion Energy Division Publications Office
44. ORNL Patent Office

EXTERNAL DISTRIBUTION

45. Office of the Assistant Manager for Energy Research and Development, Department of Energy, Oak Ridge Operations Office, P. O. Box E, Oak Ridge, TN 37831
46. J. D. Callen, Department of Nuclear Engineering, University of Wisconsin, Madison, WI 53706
47. R. W. Conn, Department of Chemical, Nuclear, and Thermal Engineering, University of California, Los Angeles, CA 90024

48. S. O. Dean, Fusion Power Associates, 2 Professional Drive, Gaithersburg, MD 20760
49. H. K. Forsen, Bechtel Group, Inc., Research Engineering, P. O. Box 3965, San Francisco, CA 94105
50. J. R. Gilleland, GA Technologies, Inc., Fusion and Advanced Technology, P.O. Box 81608, San Diego, CA 92138
51. R. W. Gould, Department of Applied Physics, California Institute of Technology, Pasadena, CA 91125
52. R. A. Gross, Plasma Research Library, Columbia University, New York, NY 10027
53. D. M. Meade, Princeton Plasma Physics Laboratory, P.O. Box 451, Princeton, NJ 08544
54. W. M. Stacey, School of Nuclear Engineering and Health Physics, Georgia Institute of Technology, Atlanta, GA 30332
55. D. Steiner, Nuclear Engineering Department, NES Building, Tibbetts Avenue, Rensselaer Polytechnic Institute, Troy, NY 12181
56. R. Varma, Physical Research Laboratory, Navrangpura, Ahmedabad 380009, India
57. Bibliothek, Max-Planck Institut fur Plasmaphysik, D-8046 Garching, Federal Republic of Germany
58. Bibliothek, Institut fur Plasmaphysik, KFA, Postfach 1913, D-5170 Julich, Federal Republic of Germany
59. Bibliotheque, Centre des Recherches en Physique des Plasmas, 21 Avenue des Bains, 1007 Lausanne, Switzerland
60. Bibliotheque, Service du Confinement des Plasmas, CEN/Cadarache, Departement de Recherches sur la Fusion Controlee, 13108 Saint-Paul-lez-Durance, France
61. Documentation S.I.G.N., Departement de la Physique du Plasma et de la Fusion Controlee, Centre d'Etudes Nucleaires, B.P. 85, Centre du Tri, 38041 Grenoble, France
62. Library, Culham Laboratory, UKAEA, Abingdon, Oxfordshire, OX14 3DB, England
63. Library, FOM-Instituut voor Plasma-Fysica, Rijnhuizen, Edisonbaan 14, 3439 MN Nieuwegein, The Netherlands

64. Library, Institute of Plasma Physics, Nagoya University, Nagoya 464, Japan
65. Library, International Centre for Theoretical Physics, Trieste, Italy
66. Library, Laboratorio Gas Ionizatti, CP 56, I-00044 Frascati, Rome, Italy
67. Library, Plasma Physics Laboratory, Kyoto University, Gokasho, Uji, Kyoto, Japan
68. Plasma Research Laboratory, Australian National University, P.O. Box 4, Canberra, A.C.T. 2000, Australia
69. Thermonuclear Library, Japan Atomic Energy Research Institute, Tokai-mura, Ibaraki Prefecture, Japan
70. G. A. Eliseev, I. V. Kurchatov Institute of Atomic Energy, P. O. Box 3402, 123182 Moscow, U.S.S.R.
71. V. A. Glukhikh, Scientific-Research Institute of Electro-Physical Apparatus, 188631 Leningrad, U.S.S.R.
72. I. Shpigel, Institute of General Physics, U.S.S.R. Academy of Sciences, Ulitsa Vavilova 38, Moscow, U.S.S.R.
73. D. D. Ryutov, Institute of Nuclear Physics, Siberian Branch of the Academy of Sciences of the U.S.S.R., Sovetskaya St. 5, 630090 Novosibirsk, U.S.S.R.
74. V. T. Tolok, Kharkov Physical-Technical Institute, Academical St. 1, 310108 Kharkov, U.S.S.R.
75. Library, Academia Sinica, P.O. Box 3908, Beijing, China (PRC)
76. K. Bol, Princeton Plasma Physics Laboratory, P.O. Box 451, Princeton, NJ 08544
77. R. A. E. Bolton, IREQ Hydro-Quebec Research Institute, 1873 Montee Ste.-Julie, Varennes, P.Q. JOL 2P0, Canada
78. R. L. Freeman, GA Technologies, Inc., P.O. Box 81608, San Diego, CA 92138
79. K. W. Gentle, RLM 11.222, Institute for Fusion Studies, University of Texas, Austin, TX 78712
80. R. J. Goldston, Princeton Plasma Physics Laboratory, P.O. Box 451, Princeton, NJ 08544

81. J. C. Hosea, Princeton Plasma Physics Laboratory, P.O. Box 451, Princeton, NJ 08544
82. Laboratory for Plasma and Fusion Studies, Department of Nuclear Engineering, Seoul National University, Shinrim-dong, Gwanak-ku, Seoul 151, Korea
83. D. Overskei, GA Technologies, Inc., P.O. Box 81608, San Diego, CA 92138
84. R. R. Parker, Plasma Fusion Center, 167 Albany Street, Cambridge, MA 02139
85. J. L. Johnson, Plasma Physics Laboratory, Princeton University, P.O. Box 451, Princeton, NJ 08544
86. L. M. Kovrizhnykh, Institute of General Physics, U.S.S.R. Academy of Sciences, Ulitsa Vavilova 38, 117924 Moscow, U.S.S.R.
87. V. D. Shafranov, I. V. Kurchatov Institute of Atomic Energy, P.O. Box 3402, 123182 Moscow, U.S.S.R.
88. J. L. Shohet, Torsatron/Stellarator Laboratory, University of Wisconsin, Madison, WI 53706
89. J. L. Alvarez-Rivas, Junta de Energia Nuclear, Avenida Complutense 22, Madrid (3), Spain
90. A. H. Boozer, C Site, A16, Princeton Plasma Physics Laboratory, P.O. Box 451, Princeton, NJ 08544
91. G. Grieger, Max-Planck Institut fur Plasmaphysik, D-8046 Garching, Federal Republic of Germany
92. S. M. Hamberger, Plasma Research Laboratory, Research School of Physical Sciences, The Australian National University, P.O. Box 4, Canberra, ACT 2600, Australia
93. R. W. Moses, MS-F642, Controlled Thermonuclear Research Division, Los Alamos National Laboratory, P.O. Box 1663, Los Alamos, NM 87545
94. O. S. Pavlichenko, Kharkov Physical-Technical Institute, Ukrainian Academy of Sciences, Kharkov 310108, U.S.S.R.
95. F. L. Ribe, 319 Benson Hall, BF10, University of Washington, 1400 Northwest Campus Parkway, Seattle, WA 98195
96. J. A. Rubio, Division de Fusion, Junta de Energía Nuclear, Avenida Complutense 22, Madrid (3), Spain

97. D. G. Swanson, Department of Physics, Auburn University, College Street, Auburn, AL 36849

98. K. Uo, Plasma Physics Laboratory, Kyoto University, Gokasho, Uji, Kyoto, Japan

99–108. Office of Fusion Energy, Office of Energy Research GTN, U.S. Department of Energy, Washington, DC 20545

R. A. Blanken, ER-542
J. F. Clarke, ER-50
D. H. Crandall, ER-542
N. A. Davies, ER-51
W. F. Dove, ER-543
S. W. Luke, ER-55
E. Oktay, ER-55
M. Roberts, ER-52
W. Sadowski, ER-541
J. W. Willis, ER-55

109–216. Given distribution according to TIC-4500 (Dist. Category UC-20)